

---

# The $^{14}\text{N}(p,\gamma)^{15}\text{O}$ reaction studied at low and high beam energy

---

DISSERTATION

zur Erlangung des Akademischen Grades

Doctor rerum naturalium (Dr. rer. nat.)

vorgelegt

der Fakultät Mathematik und Naturwissenschaften  
der Technischen Universität Dresden

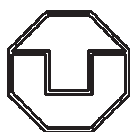
von

**Michele Marta**

geboren am 24. Mai 1979 in Romano di Lombardia (BG), Italien

1. Gutachter: Prof. Dr. E. Grosse, TU Dresden
2. Gutachter: Dr. Zs. Fülöp, D.Sc., ATOMKI Debrecen

DRESDEN 2011



Promotionskommission:

- Prof. Dr. W. Strunz (Vorsitz)
- Prof. Dr. E. Grosse
- Dr. Zs. Fülöp, D.Sc.
- Prof. Dr. K. Zuber
- Prof. Dr. T. Cowan
- Dr. W. Mader (Protokoll)

Tag der mündlichen Prüfung und Disputation: 1.11.2011

*A chi è lontano,  
ma mi è sempre vicino.*

8. And Los round the dark globe of Urizen  
Kept watch for the Eternals, to confine  
The obscure separation alone,  
For Eternity stood wide apart,  
As the stars ar apart from the earth.

from “The Book of Urizen”, William Blake



# Contents

<b>Abstract</b>	<b>6</b>
<b>1 Astrophysics: Carbon-Nitrogen-Oxygen cycle</b>	<b>9</b>
1.1 Evolution of stars . . . . .	9
1.2 Bethe-Weizsäcker (CNO) cycle . . . . .	12
1.3 Our Sun: chemical composition problem . . . . .	15
1.4 The bottleneck reaction $^{14}\text{N}(\text{p},\gamma)^{15}\text{O}$ : literature overview . . . . .	21
<b>2 <math>^{14}\text{N}(\text{p},\gamma)^{15}\text{O}</math> experiment at LUNA, <math>E = 0.3 - 0.4</math> MeV</b>	<b>29</b>
2.1 Experimental Setup . . . . .	29
2.1.1 Underground laboratory . . . . .	29
2.1.2 Accelerator and beam line . . . . .	30
2.1.3 Targets . . . . .	32
2.1.4 The Clover composite detector . . . . .	33
2.2 $\gamma$ -ray spectra and data acquisition . . . . .	35
2.2.1 Gain-matching and summing of individual spectra . . . . .	36
2.2.2 Addback mode: Study of the BGO veto . . . . .	37
2.2.3 Singles mode: Study of the ADC multiplexer . . . . .	39
2.2.4 Uncertainty due to geometry reproducibility issues . . . . .	42
2.2.5 Summary of corrections and uncertainties due to DAQ issues . . . . .	43
2.3 Net peak area calculation . . . . .	43
2.4 $\gamma$ -ray detection efficiency . . . . .	49
2.5 Effective energy . . . . .	52
2.6 True coincidence summing . . . . .	53
2.6.1 Summing-out effect calculation . . . . .	53
2.6.2 Summing-in effect for the ground state capture line . . . . .	54
2.7 Relative cross section data for capture to the ground state . . . . .	59
2.7.1 S-factors for capture to the ground state . . . . .	60
2.8 Branching ratios for the decay of the 259 keV resonance . . . . .	61
2.9 Absolute analysis of GS, 5.18, 6.17, 6.79 cross sections . . . . .	62
2.9.1 The absolute cross section . . . . .	62

2.9.2	Results and discussion . . . . .	64
<b>3</b>	<b>High-energy resonances in <math>^{14}\text{N}(p,\gamma)^{15}\text{O}</math> and <math>^{15}\text{N}(p,\alpha\gamma)^{12}\text{C}</math> studied in Dresden.</b>	<b>71</b>
3.1	Setup . . . . .	71
3.1.1	Accelerator and target chamber . . . . .	72
3.1.2	Targets . . . . .	73
3.1.3	Detection of emitted photons and efficiency . . . . .	76
3.2	$^{14}\text{N}(p,\gamma)^{15}\text{O}$ resonances . . . . .	83
3.2.1	Angular distribution of emitted $\gamma$ -rays . . . . .	84
3.2.2	Branching ratios . . . . .	85
3.3	$^{15}\text{N}(p,\alpha\gamma)^{12}\text{C}$ resonances . . . . .	86
3.3.1	Angular distribution of emitted $\gamma$ -rays . . . . .	88
3.4	Resonance strengths of $^{14}\text{N}(p,\gamma)^{15}\text{O}$ and $^{15}\text{N}(p,\alpha\gamma)^{12}\text{C}$ . . . . .	89
3.5	Preliminary off-resonance cross sections . . . . .	93
3.5.1	$\gamma$ -ray spectra . . . . .	93
3.5.2	Analysis and results . . . . .	95
<b>4</b>	<b>R-matrix analysis</b>	<b>97</b>
4.1	What is R-matrix? . . . . .	97
4.2	Influence of present data . . . . .	98
4.3	New R-matrix fit for capture to the ground state . . . . .	100
<b>A</b>	<b>Angular correlation</b>	<b>105</b>
	<b>References</b>	<b>107</b>
	<b>Acknowledgements</b>	<b>116</b>

# Abstract

The Bethe-Weizsäcker cycle consists of a set of nuclear reactions that convert hydrogen into helium and release energy in the stars. It determines the luminosity of low-metal stars at their turn-off from the main-sequence in the Hertzsprung-Russel diagram, so its rate enters the calculation of the globular clusters' age, an independent lower limit on the age of the universe. The cycle contributes less than 1% to our Sun's luminosity, but it produces neutrinos that can in principle be measured on Earth in underground experiments and bring direct information of the physical conditions in the solar core, provided that the nuclear reaction rate is known with sufficient precision.

The  $^{14}\text{N}(p,\gamma)^{15}\text{O}$  reaction is the slowest reaction of the Bethe-Weizsäcker cycle and establishes its rate. Its cross section is the sum of the contributions by capture to different excited levels and to the ground state in  $^{15}\text{O}$ . Recent experiments studied the region of the resonance at  $E_p = 278$  keV. Only one modern data set from an experiment performed in 1987 is available for the high-energy domain. Both energy ranges are needed to constrain the fit of the excitation function in the R-matrix framework and to obtain a reliable extrapolated S-factor at the very low astrophysical energies.

The present research work studied the  $^{14}\text{N}(p,\gamma)^{15}\text{O}$  reaction in the LUNA (Laboratory for Underground Nuclear Astrophysics) underground facility at three proton energies 0.36, 0.38, 0.40 MeV, and in Dresden in the energy range  $E_p = 0.6 - 2$  MeV. In both cases, an intense proton beam was sent on solid titanium nitride sputtered targets, and the prompt photons emitted from the reaction were detected with germanium detectors.

At LUNA, a composite germanium detector was used. This enabled a measurement with dramatically reduced summing corrections with respect to previous studies. The cross sections for capture to the ground state and to the excited states at 5181, 6172, and 6792 keV in  $^{15}\text{O}$  have been determined. An R-matrix fit was performed for capture to the ground state, that resolved the literature discrepancy of a factor two on the extrapolated S-factor. New precise branching ratios for the decay of the  $E_p = 278$  keV resonance were measured.

In Dresden, the strength of the  $E_p = 1058$  keV resonance was measured relative to the well-known resonance at  $E_p = 278$  keV, after checking the angular distribution. Its uncertainty is now half of the error quoted in literature. The branching ratios were also measured, showing that their recommended values should be updated. Preliminary data

for the two most intense transitions off resonance are provided.

The presence in the targets of the other stable nitrogen isotope  $^{15}\text{N}$  with its well-known isotopic abundance, allowed to measure the strength of two resonances at  $E_p = 430$  and  $897$  keV of the  $^{15}\text{N}(p,\alpha\gamma)^{12}\text{C}$  reaction, improving the precision for hydrogen depth profiling.

Part of the present data have already been published in a peer-reviewed journal:

- Relative data from LUNA (chapter 2, sec. 2.7)  
**M. Marta**, A. Formicola, Gy. Gyürky, D. Bemmerer, C. Broggini, A. Caciolli, P. Corvisiero, H. Costantini, Z. Elekes, Zs. Fülöp, G. Gervino, A. Guglielmetti, C. Gustavino, G. Imbriani, M. Junker, R. Kunz, A. Lemut, B. Limata, C. Mazzocchi, R. Menegazzo, P. Prati, V. Roca, C. Rolfs, C. Rossi Alvarez, E. Somorjai, O. Straniero, F. Strieder, F. Terrasi, H.P. Trautvetter, and A. Vomiero  
*Precision study of ground state capture in the  $^{14}\text{N}(p,\gamma)^{15}\text{O}$  reaction.*  
Phys. Rev. C 78, 022802 (2008) Rapid communication
- On-resonance data from Dresden (chapter 3)  
**M. Marta**, E. Trompler, D. Bemmerer, R. Beyer, C. Broggini, A. Caciolli, M. Erhard, Zs. Fülöp, E. Grosse, Gy. Gyürky, R. Hannaske, A.R. Junghans, R. Menegazzo, C. Nair, R. Schwengner, T. Szücs, S. Vezzù, A. Wagner, and D. Yakorev:  
*Resonance strengths in the  $^{14}\text{N}(p,\gamma)^{15}\text{O}$  and  $^{15}\text{N}(p,\alpha\gamma)^{12}\text{C}$  reactions.*  
Phys. Rev. C 81, 055807 (2010)
- Absolute data from LUNA (chapter 2, sec. 2.9)  
**M. Marta**, A. Formicola, D. Bemmerer, C. Broggini, A. Caciolli, P. Corvisiero, H. Costantini, Z. Elekes, Zs. Fülöp, G. Gervino, A. Guglielmetti, C. Gustavino, Gy. Gyürky, G. Imbriani, M. Junker, A. Lemut, B. Limata, C. Mazzocchi, R. Menegazzo, P. Prati, V. Roca, C. Rolfs, C. Rossi Alvarez, E. Somorjai, O. Straniero, F. Strieder, F. Terrasi, H.P. Trautvetter, and A. Vomiero:  
*The  $^{14}\text{N}(p,\gamma)^{15}\text{O}$  reaction studied with a composite germanium detector.*  
Phys. Rev. C 83, 045804 (2011)

This work was in part supported by DFG (BE 4100/2-1).



# Chapter 1

## Astrophysics:

## Carbon-Nitrogen-Oxygen cycle

In the last century mankind witnessed a rapid development in the scientific understanding of the cosmos. Questions like: “Has the universe always been the same as what we observe now?” or “What are stars and what makes them shine?” have found answers with astronomy, cosmology and astrophysics. The night sky looking so peaceful and quiet, is instead a place in evolution, where huge furnaces produce new elements and end up in violent explosions.

Astronomy reports about the physical quantities characterizing celestial objects that can be detected and measured. The task of astrophysicists is to explain what is observed with theoretical models based on known physics. The physics of a star involves a wide spectrum of fields, from gravitation to electromagnetism, from plasma hydro/thermodynamics to particle and nuclear physics.

In 1920 Eddington asserted that the energy corresponding to the difference in mass between four protons and one helium nucleus could explain the huge power output of stars. A new branch of physics was born, nuclear astrophysics, which aims to measure and quantitatively understand nuclear reactions of interest for astrophysics.

### 1.1 Evolution of stars

Stellar evolution [1, 2] starts with the gravitational collapse of a cloud of gas and dust. The gravitational potential energy is transformed into thermal and radiation energy which is mostly lost at the beginning due to the transparency of the matter. With increasing density and opacity, some of the radiation is retained, temperature and pressure in the inner part start to rise and counterbalance the gravitational contraction.

Then, when the temperature reaches several million Kelvin, the fusion of hydrogen to helium starts. By this time the star has reached a hydrostatic and thermal equilibrium: the inward-pushing gravitational force and the outward-going radiative pressure balance

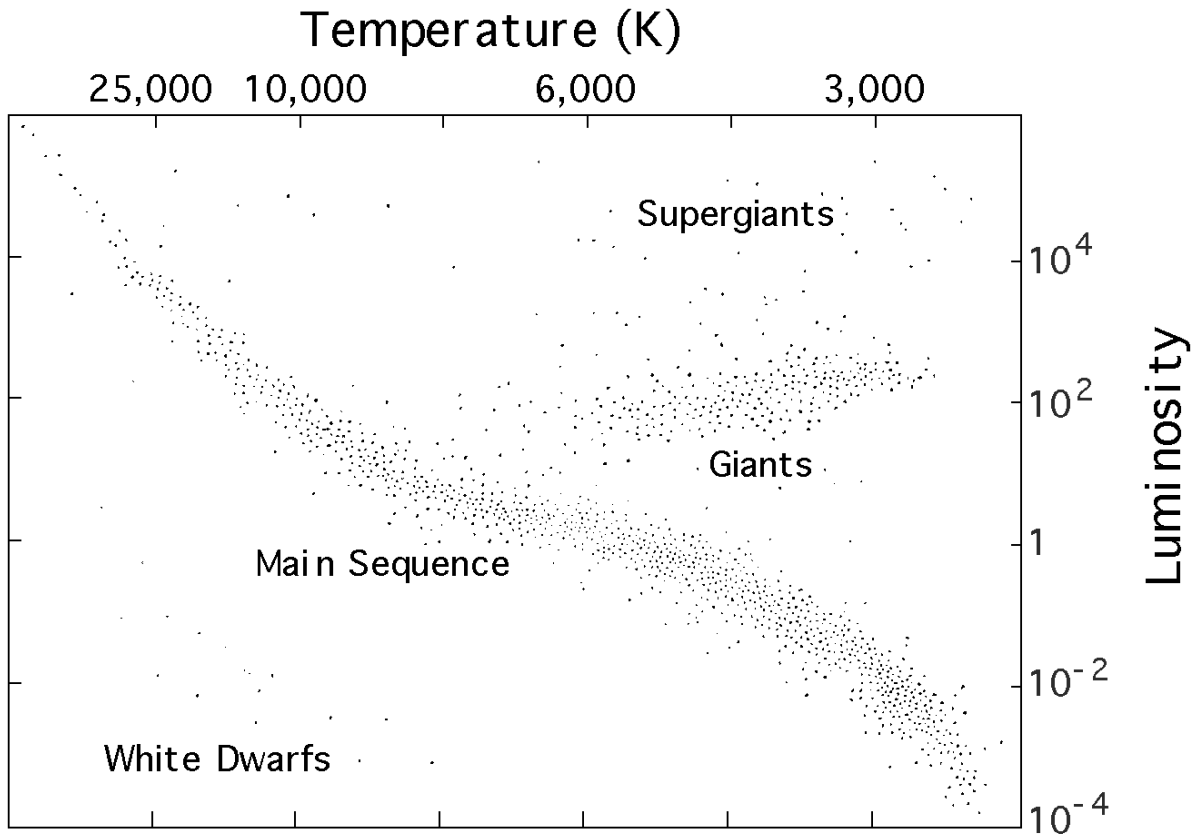


Figure 1.1: Hertzsprung-Russel (or color-magnitude) diagram: luminosity (relative to the Sun's luminosity  $L_{\odot}$ ) versus effective surface temperature. The regions of main sequence, giants and white dwarfs are indicated (Source: <http://edu-observatory.org>).

one another, the temperature and density gradients are stable. In the Hertzsprung-Russel diagram (fig. 1.1) of relative luminosity versus effective surface temperature, a diagonal narrow band groups all the stars that reached this stable phase of hydrogen burning in the core; it is referred to as the *main sequence*. The stars spend 99% of their life in this phase. The absolute value of time depends on their initial mass: it ranges from twenty billion years for stellar mass  $M < M_{\odot}$ <sup>1</sup> to only a few hundreds million years for  $M > 100 M_{\odot}$ .

During the hydrogen-burning phase, two main mechanisms are possible for the production of energy by the conversion of four protons into one helium nucleus: the p-p chain and CNO cycle. The p-p (proton-proton) chain is the most active process in low mass stars, where the core temperature is less than 20 million degrees [2]. Its first step  ${}^1\text{H} + {}^1\text{H} \rightarrow {}^2\text{H} + e^+ + \mu$  is the slowest reaction, because it involves the weak nuclear interaction. That strongly limits<sup>2</sup> the rate of energy production and hydrogen conversion.

<sup>1</sup> $M_{\odot}$  indicates the total mass of the Sun.

<sup>2</sup>Fortunately! so stars do not consume all their fuel too fast in a big explosion and give mankind enough time to evolve on Earth, think about the universe and possibly write a PhD thesis.

The CNO cycle is the other possible set of reactions during hydrogen burning, given that a catalytic abundance of carbon is present in the gaseous nebula of origin, coming from the ashes of previous stars. This cycle will be extensively discussed in section 1.2. At this stage, no further reactions produce stable elements heavier than  ${}^4\text{He}$ , except for  ${}^7\text{Li}$  which is rapidly converted into two helium nuclei after a proton capture. That is due to the lack of stable nuclei of mass 5 and 8.

When the quantity of hydrogen decreases and its burning rate is not enough to produce a power output able to counterbalance the gravitational force anymore, the core shrinks and heats up until another equilibrium is reached. That corresponds to the onset of other nuclear reactions, that will proceed at a much higher rate with respect to hydrogen burning, due the higher core temperature and density.

The next burning stage converts helium into carbon by means of the triple-alpha process, which overcomes the mass stability gaps at  $A = 5$  and  $8$ . As a first step, two helium nuclei form  ${}^8\text{Be}$ , which decays rapidly back to two  $\alpha$ -particles with lifetime of the order of  $10^{-16}$  s. Nevertheless, if another  ${}^4\text{He}$  interacts with  ${}^8\text{Be}$  during its negligibly short existence, a carbon nucleus can be produced via the  ${}^8\text{Be}(\alpha, \gamma){}^{12}\text{C}$  reaction. A further radiative  $\alpha$ -capture on carbon yield a significant amount of  ${}^{16}\text{O}$ , the most abundant element in the universe after H and He.

During the helium-burning era, the star leaves the main sequence and its outer appearance changes dramatically. The hotter and denser core produces energy at a higher rate, the increased radiative pressure makes the outer envelopes expand and cool: the star becomes a red giant, increasing the radius by a factor 50.

If the initial mass is large enough, several other burning stages in the core follow producing heavier nuclei, while previous burning processes occur in the shells surrounding the core. The heaviest elements produced via direct fusion of lighter mass elements are iron and nickel, in the region of  $A \approx 60$ . Due to the decreasing trend of nuclear binding energy per nucleon beyond the iron peak, no further energy release can be obtained via fusion.

Elements heavier than mass 60 are mainly produced via the so-called *s-, r-, and p-processes*. The slow s-process produces the larger amount of heavy elements by consecutive neutron captures on “seed”-nuclei present in the star and  $\beta^-$  decays of unstable species. The flux of neutrons at this stage makes a further neutron capture on radioactive nuclei a negligibly probable process, therefore the process follows closely the line of stability.

The r- and p-processes both occur very rapidly and as a consequence of non-equilibrium endothermic processes, for instance during Supernova explosions. Nucleosynthesis of proton-rich nuclei may be obtained via the *rp-process*, a series of fast consecutive proton captures on the CNO seed nuclei and following  $\beta^+$ -decays close to the proton drip line in the chart of nuclides.

When no further energy production from fusion prevents the gravitational collapse,

the star reaches its end. The star “death” also depends on its mass: the larger the mass, the denser will be the remnant object after the explosive emission of the outer layers. The Chandrasekhar limit of about  $1.4 M_{\odot}$  establishes whether the core left behind becomes a white dwarf or an even denser object such as a neutron star or a black hole, after a Supernova explosion. In a white dwarf, a further gravitational collapse of matter is prevented by the electron degeneracy pressure of the high density matter, about one solar mass compressed in an Earth-like volume.

Beyond the Chandrasekhar limit, the Fermi energy of the electrons is so high that they can react with protons and convert them to neutrons: the final object is referred to as a neutron star, even though its inner content and structure are matter of debate. When the remaining mass is so high that also the neutron degeneracy pressure is not enough to prevent further collapse, a black hole is formed. Its intense gravitational field curves the space-time so that even light cannot escape and it can be detected only indirectly from the behaviour of its surroundings.

Beside producing the energy needed to counterbalance the gravitational collapse, the thermonuclear reactions in stars are also responsible<sup>3</sup> for neutrinos of various energies and intensities. Due to their negligible interaction probability with matter, neutrinos bring direct information about the astrophysical site they originated from. The solar neutrinos detected on Earth have already been used to confirm our models about how our Sun produces its energy and can be used to obtain other information about its interior (section 1.3).

A few neutrinos from much farther away have been detected in 1987, when we were reached by the radiation following the first Supernova explosion in our Galaxy after the invention of the telescope. A total number of about 24 anti-neutrinos were detected in neutrino observatories a few hours before its observational confirmation in the visible light, giving experimental reliability to the theory that neutrinos are produced during a core-collapse Supernova.

In the future, neutrinos will probably enlarge the observational window on the cosmos, opened thousands years ago by the first sky observers, continued after the invention of telescopes and extended by space satellites and huge detectors on Earth to a wide spectrum of electromagnetic radiation and particles.

## 1.2 Bethe-Weizsäcker (CNO) cycle

The reaction presently studied is the  $^{14}\text{N}(p,\gamma)^{15}\text{O}$ , the bottleneck of one mechanism for burning hydrogen, the CNO (Carbon-Nitrogen-Oxygen) or Bethe-Weizsäcker cycle [3, 4]. The process (the first part of CNO bi-cycle) was independently proposed by Carl Friedrich von Weizsäcker and Hans Bethe in 1938 and 1939, respectively. The latter was

---

<sup>3</sup>Often not directly, but through  $\beta$ -decays of the reaction products.

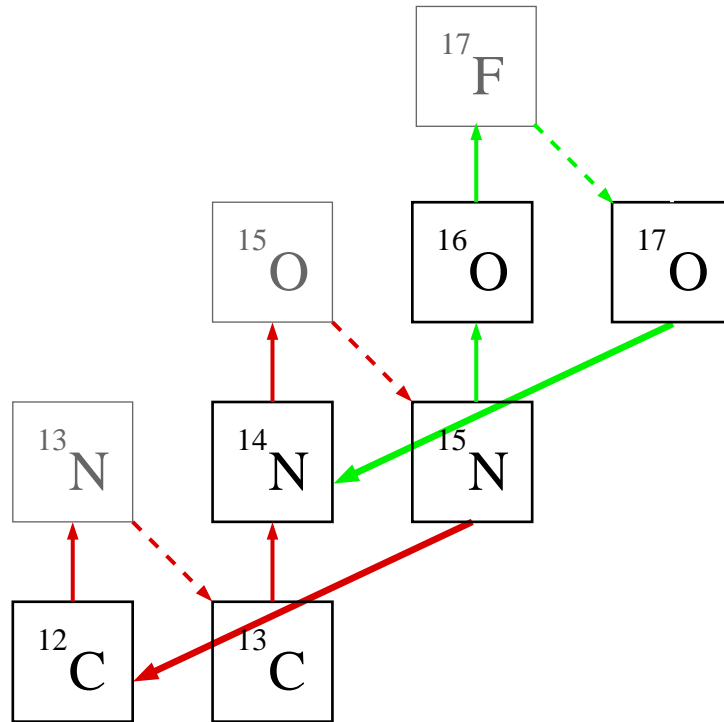


Figure 1.2: The CNO bi-cycle (cycle I in red, cycle II in green) presented on the (Z,N) chart of nuclides. The reactions between stable (black) and unstable nuclei (grey) are: (p,γ) radiative capture (solid), (p,α) (solid bold), β<sup>+</sup> decay (dashed).

a German-American physicist, forced to emigrate from Germany in 1933 after the Nazi party came to power. Nobel laureate in physics in 1967 for his work on the theory of stellar nucleosynthesis, Bethe also made important contributions to quantum electrodynamics, nuclear physics, solid-state physics and particle astrophysics. During World War II, he was head of the Theoretical Division at the secret Los Alamos laboratory developing the first atomic bombs.

The former was a German physicist and philosopher, elder brother of Richard von Weizsäcker who was president of the Federal Republic of Germany from 1984 to 1994, and thus the first president after German reunification in 1990. He was the longest-living member of the research team which performed nuclear research in Germany during the Second World War, under Werner Heisenberg's leadership. His special interest as a young researcher was the binding energy of atomic nuclei and the nuclear processes in stars.

The two physicists suggested the same combination of reactions starting from <sup>12</sup>C, as a more efficient way of converting four protons into one helium nucleus and producing energy in stars, than having two protons interacting directly. Only later, the complete proton-proton chain was found to be the most probable mechanism for low mass and metal-poor stars.

The CNO cycle is a set of nuclear reactions (fig. 1.2) that requires a catalytic amount of carbon already present in order to occur. The conversion of four hydrogen nuclei into

one helium nucleus proceeds through several proton captures and radioactive decays, the last proton capture ended by the emission of an  $\alpha$ -particle and the starting-point carbon nucleus. The overall output consists of an increase in He abundance, energy release, two positrons (converted to thermal energy) and two electronic neutrinos from the  $\beta^+$  decay of  $^{13}\text{N}$  and  $^{15}\text{O}$  with end point energy 1.20 and 1.73 MeV respectively, which escape the star at the speed of light. The energy converted into star thermal energy corresponds to the reaction Q-value of 26.73 MeV, exactly as for the p-p chain, minus the energy taken away by the two neutrinos. Due to the higher Coulomb repulsion, this cycle's rate is much lower than the concurrent p-p chain<sup>4</sup> at core temperatures  $T_6^5 < 20$ , but increases steeper with temperature, being its energy generation for core temperature around  $T_6 = 20$  proportional to  $T^{18}$ , whereas the contribution from the p-p set of reactions is proportional to  $T^4$ . Therefore the CNO cycle is the main source of energy in intermediate and massive stars during their main sequence phase.

Recently the CNO cycle received further attention in the astrophysics community. During the Asymptotic Giant Branch (AGB) phase when energy is produced in two different He- and H-burning shells around the CO core, the rate of the  $^{14}\text{N}(p,\gamma)^{15}\text{O}$  and triple-alpha reactions influences the strength of *dredge-up* events following He flashes, i.e. the transfer of nuclear processed material from high-temperature stellar interior to the low-temperature stellar surface, where it can be observed spectroscopically. This material is also blown into the interstellar medium by stellar winds, thus contributing to the galactic chemical evolution.

Published uncertainty estimates for each of these two rates propagated through stellar evolution calculations cause uncertainties in carbon enrichment of about a factor of 2 [5]. The increase of mixing in low and intermediate mass stars due to a slower CNO cycle can be the reason for a special kind of red giants that show to contain more carbon than oxygen in their atmosphere, so-called carbon stars.

Moreover, the CNO cycle rate drives the luminosity of stars that run out of hydrogen fuel and start leaving the stable main sequence phase for the red giant one. This very luminous short period of their lifetime corresponds to a position in the Hertzsprung-Russel diagram still on the main-sequence, but shifted to higher temperature and luminosity, called *turnoff point*. Based on stellar evolution models that provide estimates of the surface temperature and luminosity of stars as a function of time, one could in principle infer the age of stars at different positions in the H-R diagram. However, the most robust prediction is the time it takes a star to exhaust the supply of hydrogen in its core, which corresponds to the turnoff point. From the absolute turnoff luminosity value it is possible to obtain the age of the star [6], if a reliable theoretical calibration of the turnoff luminosity-age relation can be obtained. This relies on ingredients such as our knowledge

---

<sup>4</sup>Assuming C, N or O species concentration of 1% by mass.

<sup>5</sup> $T_6$  is the temperature expressed in million degrees Kelvin.

of the physical processes of energy generation (nuclear reactions) and transport (opacity, convection) taking place in H-burning stars, and their chemical composition.

Of great importance is the case when the stars at the turnoff point belong to a globular cluster. Those are groups of up to millions of stars gravitationally bound together that populate the halo of the Milky Way and are thought to have formed from the primordial gas cloud that then became our galaxy. They are the oldest observable objects in the galaxy, as proven by their very low metallicity: their iron content is less than one hundredth of the solar system abundance, suggesting that the gas which they formed from did not experience previous significant metal enrichment associated with star formation and evolution. The CNO cycle rate helps dating the globular clusters, the fossils of our Galaxy, thus constraining the age of the universe [7, 8].

Lastly, even though the CNO cycle contributes less than 1% [9] to the energy production in our Sun, the neutrinos produced by it can help solving a recent discrepancy about the solar chemical composition. A detailed description of this issue is given in the following section 1.3.

The  $^{14}\text{N}(p,\gamma)^{15}\text{O}$  is the slowest reaction in the CNO cycle. It means that all  $^{12}\text{C}$  is converted into  $^{14}\text{N}$  in a much shorter time than the following conversion of  $^{14}\text{N}$  into  $^{15}\text{O}$ . One can talk about lifetimes of the different species involved, which are inversely proportional to their consumption rate into the next specie and depend on temperature. In this view, the  $^{14}\text{N}$  lifetime is much larger than the  $^{12}\text{C}$  one at same temperature. The complete CNO cycle includes other less probable reactions, starting with the  $^{15}\text{N}(p,\gamma)^{16}\text{O}$  [10] whose probability is only one thousandth of the competing  $^{15}\text{N}(p,\alpha)^{12}\text{C}$ . The set of reactions starting from  $^{16}\text{O}$  forms a second loop, usually referred to as CNO-II (fig. 1.2), and reaches up to a fluorine isotope. Further reactions beyond this loop are also possible, especially at higher core temperature in massive stars.

A modification of the Bethe-Weizsäcker cycle occurs in special conditions of very high temperatures (above 0.1 GK) e.g. during novae outbursts of accreting material around a white dwarf star. The nuclear reaction rates are so enhanced by the temperature increase that they are faster than the radioactive decays. The so-called hot CNO cycle still converts four protons to one helium nucleus, but via a different reaction path, and its speed is only constrained by the decay half life of the unstable isotopes included in the cycle.

### 1.3 Our Sun: chemical composition problem

The solar system originated 4.57 billions years ago [9], based on radiometric dating of the oldest meteorites [11, 12]. It started from the collapse of a dense cloud of gas (mainly hydrogen and helium) and dust, like the many similar clouds we can observe in the universe around us. After an initial pre-main sequence phase where strong solar wind swept over the forming planets, it stabilized and entered the main sequence in the hydrogen-burning

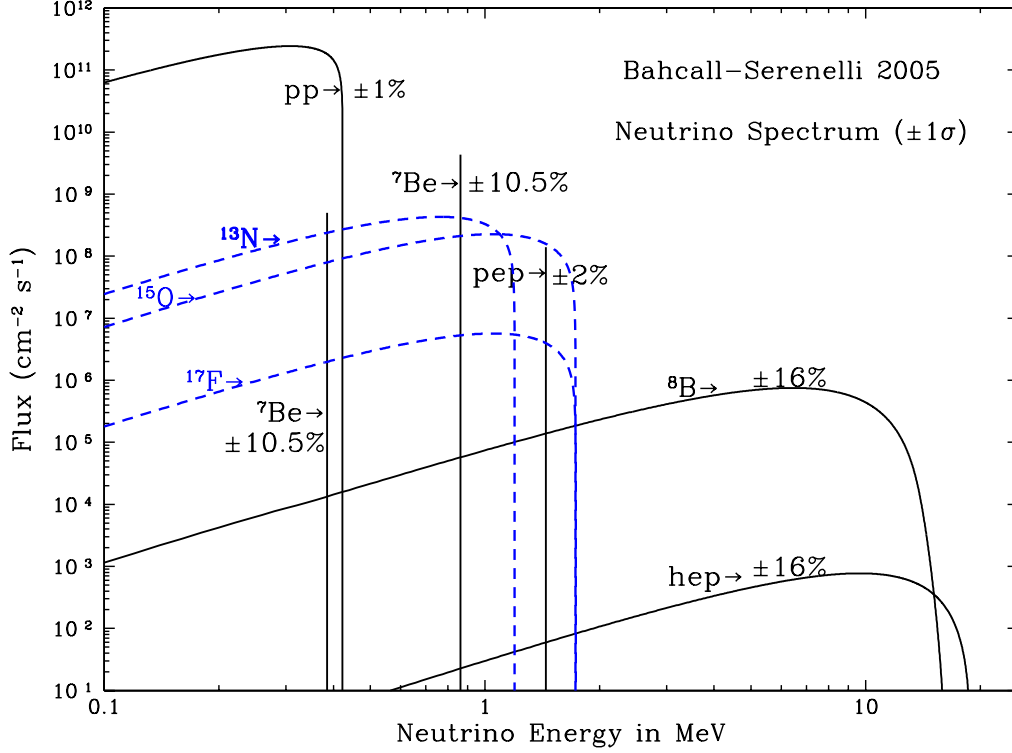


Figure 1.3: Expected neutrino spectrum based on BS05 model calculation [13]: both fluxes from p-p chain (solid black) and CNO (dashed blue) are shown. Figure taken from Ref. [13].

phase.

Since it is a low mass star, the Sun has been burning hydrogen for almost five billion years. In about another 5 billion years it will enter the red giant phase: the helium burning in the core will make the outer layers expand (and cool) beyond the present orbit of the planet Mercury. By that time, life on our planet would be probably already extinguished starting one billion years from now, due to the gradual increase in solar luminosity (10% per billion years) that would boil all the liquid water away.

Finally, after intense thermal pulses, the outer layers will be ejected and the Sun will end up as a planetary nebula, with a white dwarf (the previous star's core) at the center, enriched in carbon and oxygen, the products of previous He-burning.

Starting from when the thermonuclear reactions were found responsible for the huge power output of the stars, many efforts have been done to understand how our Sun works. The Standard Solar Model (SSM) is a framework of calculations and data based on known physics, ranging from gravitation to thermodynamics, from interaction of photons with matter to nuclear physics, and some assumptions, i.e. a chemically homogeneous zero-age Sun. It predicts solar properties such as the surface chemical composition, luminosity, neutrino fluxes (fig. 1.3), internal structure. The model yields as a result quantities that can be observed and measured, thus constraining it and testing its reliability.



Recent SSM [9, 14] states that 99% of nuclear reactions occur in the inner core of the Sun, up to 0.25 of the total solar radius  $R_{\odot}$  (containing almost half of the solar mass, due to the high density), the temperature being  $T_6 = 15.7$  at the center and decreasing to  $T_6 = 7$  at the zone border. 99% of the energy is produced by the p-p chain and the rest by the CNO cycle. The elemental abundances in the core have changed because of the active reactions: the  ${}^4\text{He}$  mass fraction has increased from the primordial value of 26% to more than 60% [14] depending on the model and all the original  ${}^{12}\text{C}$  has been converted into  ${}^{14}\text{N}$ .

Around the core there is a radiative region extending up to  $0.7 R_{\odot}$ , with temperature decreasing down to  $T_6 = 2$ , where heat is transferred outwards by the photons scattering in the plasma. Outside this region, the lower temperature allows the heavier nuclei to be only partially ionized, making the matter opaque. The masses in contact with the radiative zone are heated until they are less dense than the surrounding and start ascending, forming convective cells, the tops of which are observed at the surface as granulation. In the convective zone the heat is transferred outside the star by the convection mechanism. The region is characterized by much lower density with respect to internal regions and large temperature and density gradients. Despite its large volume, it contains only a few percent of the solar mass.

At the surface of the Sun there is the photosphere, where the observed radiation comes from. Its spectrum is similar to the one from a black body, with surface temperature of  $\approx 5800$  K. The solar atmosphere is divided into chromosphere, transition region and corona. In the corona, the strong magnetism and shock waves may be the reason for the very high temperature (few million degrees) observed in this very low density region.

Increasingly detailed and reliable SSM models have been produced, motivated and continuously constrained by the variety and precision of observed data: the photosphere elemental composition, helioseismic measurements, and recently neutrino fluxes detected in big experiments in underground laboratories on Earth.

The neutrinos bring a direct signature of the reaction and environment of origin, due to their negligible probability of interaction with matter after being produced. One particle in every 100 billion is intercepted on its flight toward the solar surface, corresponding to a mean free path in the solar matter much larger than the solar radius. For comparison, the mean free path of photons in the convective zone is just a few centimeters due to the large opacity.

The neutrino fluxes corresponding to the p-p reaction [15], the boron [16] and beryllium decays [17] have already been detected on Earth, by several experiments [18]. At first they were found in disagreement with expectations from the standard solar model, which raised the so-called solar neutrino puzzle. The solution was found 30 years later in the underlying physics, when the oscillation in neutrino flavor was experimentally discovered by the SNO experiment [19], that was able to discriminate between electronic and mu/tau neutrinos.

Presently the neutrino fluxes keep on probing our understanding of the processes in our Sun.

Helioseismology studies the Sun based on the oscillation modes observed at the Sun's surface via Doppler interferometry. Similarly to geoseismology and seismic waves, the thousands of possible acoustic p-modes (pressure) can provide information about the internal structure of the Sun.

The most precise sources of observed oscillation frequencies presently available are the Global Oscillation Network Group (GONG) project [20] and the Michelson Doppler Imager (MDI) instrument on board the Solar and Heliospheric Observatory (SOHO) [21]. Most of the frequencies are in the range 1-4.5 mHz and are determined to a precision of about 0.01% [22, 23], which allows one to make stringent tests of solar models.

Since different oscillation modes penetrate to different depths, the sound speed profile versus radius can be mapped by solving the inverse problem over a broad range reached by the acoustic waves, namely from 0.05 to 0.95  $R_{\odot}$ . The innermost and outermost regions cannot be covered at the moment, due to the lack of respectively very low and very high frequency modes from observations. Other correlated quantities can be measured, such as the position of the base of the convection zone, where the sound speed profile has a discontinuity in the second derivative, and the helium content in this region, thus offering valuable insight into very opaque regions.

Photospheric chemical abundances are inferred based on observed absorption lines in the solar spectrum and realistic models of the solar atmosphere and spectrum formation process. The latest model [24, 25] includes improvements in atomic and molecular transition probabilities, 3D hydrodynamical atmospheres and relaxes the assumption of Local Thermodynamical Equilibrium (LTE) in the spectral line formation.

As opposed to one-dimensional models, the updated 3D approach manages to reproduce the observed solar granulation topology, convective velocities and with respect to previous models, it better matches the absorption line shape and the observed center-to-limb intensity variation as a function of wavelength.

The results on elemental abundances [24, 25] agree well with the mass spectroscopy analyses of old meteorites and independent estimates provided by spectra of solar-type stars, absorption nebulae and interstellar matter in the solar neighbourhood. The best samples for elemental analysis are the so-called *CI carbonaceous chondrites*, which belong to the class of meteorite showing the least evidence for chemical fractioning and remelting after condensation. They retained most of the elements as they were at the formation of the solar system, except the volatile elements H, He, C, N, O, Ne which have been depleted since then.

There are no photospheric lines of the noble gases (He, Ne, Ar, Kr and Xe), due to their high excitation potentials, thus their abundances are estimated through indirect methods (He abundance is taken from helioseismic results). The present accuracy for

Model	$Z_{\text{surf}}$	$Y_{\text{surf}}$	$R_{\text{CZ}}/R_{\odot}$	$\langle \delta c/c \rangle$
GS98, high- $Z$ (1D)	0.0170	$0.2423 \pm 0.0020$	$0.713 \pm 0.001$	0.0010
AGSS09, low- $Z$ (3D)	0.0134	$0.2314 \pm 0.0020$	$0.724 \pm 0.001$	0.0038
Helioseismology		$0.2485 \pm 0.0035$	$0.713 \pm 0.001$	0

Table 1.1: State of the art Standard Solar Models [14] based on different metallicity calculated from chemical compositions GS98 [26] and AGSS09 [24].  $Z_{\text{surf}}$  and  $Y_{\text{surf}}$  are the metallicity and helium abundance by mass at the surface,  $R_{\text{CZ}}/R_{\odot}$  is the position of the convection zone base relative to the solar radius and  $\langle \delta c/c \rangle$  the relative difference between model and helioseismic sound speed, averaged along the whole radius. In the last row the results by helioseismology [22].

most elements is 10%, mainly due to the poor atomic and molecular data available, such as transition probabilities corresponding to spectral lines.

The improved model leads to significantly lower 25% abundances for C, N, O, and Ne compared to the values used one decade ago [26], obtained with a 1D model for the solar atmosphere. As a consequence, the value for the metallicity<sup>6</sup>  $Z$  has decreased from 0.017 in 1998 to present 0.0134, the hydrogen and helium abundances by mass at the surface being respectively  $X = 0.7380$ ,  $Y = 0.2485$  (by definition  $X+Y+Z=1$ ) [25].

The state of the art SSM [14] which uses an input metallicity  $Z = 0.0134$  obtained from these latest revised abundances (AGSS09) [24] disagrees with the helioseismological data [22] by several standard deviations (tab. 1.1), whereas the agreement had been perfect with previous high- $Z$  models [9] using  $Z = 0.0170$  (BS05-GS98) [26]. The discrepancy affects the depth of the convection zone ( $R_{\text{CZ}}$ ), the helium abundance at the surface ( $Y_{\text{surf}}$ ) and the sound speed ( $c$ ) and density profiles versus radius.

The decrease in opacity, a consequence of the lower metallicity, makes it possible for convectively-stable layers to exist at comparatively low temperatures, hence the shift of the limit of convective regime towards higher radii in the low- $Z$  model, in disagreement with helioseismic measurements.

The sound speed profile shows a maximum difference of 1% between the new low- $Z$  model and helioseismology data right below the base of the convection zone and an averaged discrepancy over the whole solar radius of 0.4% (tab. 1.1, last column). That is beyond the uncertainties of both model and measurement.

Several solutions have been suggested to solve the Sun’s composition problem, by assuming a strong variation of input parameters to the SSM. It has been calculated [14] that an increase of the opacity by 15% right below the convection zone and over an extended range of solar radius could resolve the problem, but it is improbable that this property is affected by such a large error. Besides, this would solve only [24] the sound speed profile discrepancy, leaving the surface helium abundance prediction  $Y_{\text{surf}}$  unchanged

---

<sup>6</sup>The metallicity is the proportion by mass of all the elements heavier than helium.

and still in contradiction with helioseismology. The low-metallicity models that have the least disagreement with seismic data require changing all input physics to stellar models beyond their acceptable ranges [22]. The helioseismic results favour models with high-Z inner solar composition.

A possible solution that would bring agreement between observations and models, would be a process that lowered the metallicity of the outer layers, leaving the elemental abundances in the inner sections unchanged. One should not forget that all SSMs are based on one assumption, i.e. a homogeneous metallicity at the early stage of the Sun, due to a fully convective, highly luminous phase that homogenized the Sun [27]. According to the model, after entering the main sequence a radiative core was established which strongly limited the material exchange, letting the abundances in the two regions change independently from that moment on. An interesting possibility suggested by the authors of Ref. [27] assumes that a metal-depleted gas accreted onto the surface after the Sun reached the main-sequence phase, when the radiative zone was already formed. That would explain the low metallicity observed at the surface of the Sun and the substantially metal-rich atmospheres of the giant gas planets, with respect to the solar system average. Assuming a homogeneous metallicity of the gas cloud from which the Sun and planets formed, a metallicity higher than average in one region means that an equivalent lower metallicity mass is produced. A rough calculation of the increased metallicity of the planets results approximately in the decreased one in the solar atmosphere, but a more solid confirmation is missing.

New interest has been raised on the CNO cycle because a precise enough measurement of CNO neutrinos could bring the missing information on the core content of C and N elements, through an independent method. In our Sun, the CNO cycle accounts for less than 1% of energy production, but for 100% of the neutrino flux from the  $\beta^+$  decay of  $^{13}\text{N}$  and  $^{15}\text{O}$ . It has been proposed [27] to make use of the future measurement of the solar neutrino flux in experiments such as Borexino [17, 16, 28] and the SNO+ to obtain direct information on the Sun's core metallicity, based on:

**T<sub>core</sub>:** the core temperature is obtained from the  $^8\text{B}$  neutrino flux measured at Super-Kamiokande I with a precision of 3% [18] and the oscillation parameters which have by now been well-constrained (4.6%), most notably by data from the SNO [29] and KamLAND [30] neutrino detectors;

**Environmental data:** opacity, diffusion are known to less than 5% error;

**Nuclear reactions (S-factors):** leading to  $^8\text{B}$  and the CNO neutrinos, the latter being known with 7% error [31]. Less than 5% is advisable for the present purpose.

The flux of CNO neutrinos has not yet been measured online, but it is believed that both Borexino and the planned SNO+ detector [32] can provide such data in the near future, hopefully with uncertainties at the same level of the other quantities involved.

core temperature	3%
solar environmental data	1%
neutrino oscillation	4.9%
nuclear reactions [31]	7%

Table 1.2: Uncertainty budget in the determination the CN chemical composition of the core based on CN neutrino detected on Earth [27].

## 1.4 The bottleneck reaction $^{14}\text{N}(\text{p},\gamma)^{15}\text{O}$ : literature overview

In low-energy nuclear astrophysics it is a general rule to parameterize reaction cross sections  $\sigma(E)$  in terms of astrophysical S-factors  $S(E)$  [33]:

$$S(E) = \sigma(E)E \exp\left(2\pi\eta\sqrt{\mu/E}\right); \quad \text{with } \eta = \frac{Z_1 Z_2 e^2}{\hbar v} \quad (1.1)$$

with  $E$  denoting the effective energy in the center of mass system and  $\mu$  the reduced mass.  $\eta$  is the Sommerfeld parameter, function of the charge of interacting nuclei  $Z_1$  and  $Z_2$ , their relative velocity  $v$ , electron charge  $e$  and Planck's constant  $\hbar$ . The astrophysical factor  $S(E)$  varies slowly with energy far from resonances and it contains only the nuclear properties of the reaction. The exponential accounts for the probability of tunneling through the Coulomb barrier for reactions between charged particles. For the present reaction, equation 1.1 expressed in numerical form is:

$$S(E) = \sigma(E)E \exp\left(212.4/\sqrt{E}\right) \quad (1.2)$$

with  $E$  given in keV.

The reaction is a radiative capture into one of the excited states of  $^{15}\text{O}$  (fig. 1.4), either via the resonant or the nonresonant (Direct Capture) mechanism. Every reaction is followed by the emission of one or two (rarely three) prompt  $\gamma$ -rays in cascade: a *primary* emission corresponding to the capture to one level of  $^{15}\text{O}$ , either the ground state or an excited state. In this last case, a *secondary* emission follows, due to the decay of the level to the ground state.

The resonances play a major role in the reaction cross section versus energy and in the extrapolation procedure to very low energies of astrophysical interest. The narrow resonance at  ${}^7E_p = 278$  keV has been well studied in the past years, due to several experiments [36, 37, 35] performed relatively recently in the energy region below  $E_p = 500$  keV. Its recommended strength is known with 4.6% total uncertainty [31], and it is used as a reference in the present work. The resonance at  $E_p = 1058$  keV was last studied by an

---

${}^7E_p$  denotes the beam energy in the laboratory system, while  $E$  is the effective beam energy in the center of mass frame.

$Q$ [keV]	$E$ [keV]	$E_x$ [keV]	$J^\pi$
	2187	9484	$3/2^+$
	987	8284	$3/2^+$
	259	7556	$1/2^+$
7297		7276	$7/2^+$
$^{14}\text{N} + \text{p}$		6859	$5/2^+$
	-505	6792	$3/2^+$
		6172	$3/2^-$
		5241	$5/2^+$
		5181	$1/2^+$
		0	$1/2^-$

$^{15}\text{O}$

Figure 1.4: Level scheme [34, 35] of excited states in  $^{15}\text{O}$ , relevant to the  $^{14}\text{N}(p,\gamma)^{15}\text{O}$  reaction.

experiment performed in 1987 [38], its reported strength has 13% error. A new result based on present experimental data is obtained in chapter 3.

At low energies, subthreshold resonances play a role if their high energy tail is still competitive with the off-resonance direct capture contribution to the cross section. This is the case for the subthreshold resonance at  $E = -505$  keV, corresponding to the 6792 keV excited state in  $^{15}\text{O}$ . It is believed to enhance the contribution of the capture to the ground state to the total  $S_{\text{tot}}(0)$  in the energy region  $E < 150$  keV.

The results from experimental studies in the past yielded a recommended value for extrapolated total S-factor of  $S_{\text{tot}}(0) = 3.5_{-1.6}^{+0.4}$  keV b [39]. The most updated data taken into account in that compilation were from an experiment performed in 1987 [38] which covered a wide range of energy, from  $E_p = 0.2$  to 3.6 MeV. The subthreshold resonance at  $E = -505$  keV was included into the extrapolation procedure, letting its energy width vary as a free parameter in the fit to the data. That made the capture to the ground state account for half of the total reaction cross section.

However, after year 2000 it became clear that this contribution was much overestimated by previous compilations for astrophysics [40, 39, 41], based on new and independent experimental results. Among those, the reduction of the  $\gamma$ -width ( $\Gamma_\gamma$ ) of the 6.79 MeV excited state, observed via Doppler shift attenuation [42, 43] and Coulomb excitation [44]. The first finding in 2001 [42] triggered a re-evaluation of 1987 data in the R-matrix work

Transition	Schröder [38]	Brussels [45]	LUNA [35]	TUNL [37]	TexasA&M [46]	Nelson [49]
5181			0.010±0.003			
5241			0.070±0.003			
6172	0.14±0.05	0.06 <sup>+0.01</sup> <sub>-0.02</sub>	0.08±0.03	0.04±0.01	0.13±0.02	0.16±0.06
6792	1.41±0.02	1.63±0.17	1.20±0.05	1.15±0.05	1.4±0.2	
GS	1.55±0.34	0.08 <sup>+0.13</sup> <sub>-0.06</sub>	0.25±0.06	0.49±0.08	0.15±0.07	
total	3.20±0.54	1.77±0.20	1.61±0.08	1.68±0.09	1.68±0.2	

Table 1.3: Astrophysical factor  $S(0)$  [keV b] from previous works.

that lowered dramatically the extrapolation of S-factor for capture to the ground state  $S_{GS}(0)$  (to  $0.08_{-0.06}^{+0.13}$  keV b) [45]. Following experiments also pointed in the same direction of reducing the capture to the ground state contribution to the S-factor: investigations via indirect method [46, 47] and direct measurements of the reaction cross section at LUNA (Gran Sasso underground laboratories) [36, 35] and TUNL (North Carolina) [37] facilities.

One uncertain parameter in the fits is the energy width  $\Gamma_\gamma$  of the subthreshold resonance corresponding to the 6.79 MeV excited state, because its very short lifetime of less than a few femtoseconds makes it difficult to measure it precisely experimentally. Table 1.6 summarizes the efforts that have been done, using different methods, direct and indirect. The strength of the subthreshold resonance influences the rise of the  $S_{GS}$  towards low energy, decisive for the contribution of the capture to the ground state in the overall cross section budget.

The value of the S-factor being halved, led to a re-calculation [7] of the age of globular clusters (sec. 1.2). The lower the reaction rate, the higher the predicted turnoff luminosity: since the latter is fixed by observation, older and lower than previously believed mass stars account for the observed luminosity. The change is an increase of 0.7 - 1 Gy [7] in the age of the oldest galaxy cluster, increasing the lower limit to the age of the universe to about  $14 \pm 1$  Gy. This is still in agreement with an independent estimation of the age of the universe of  $13.7 \pm 0.2$  [48], based on the cosmic microwave background measurements and the data from the WMAP space satellite.

The extrapolated S-factor corresponding to capture to several excited states of  $^{15}\text{O}$  resulting from recent experiments in literature are summarized in table 1.3. The lower  $S(0)$  is included in a recent compilation [31]. Note the strong decrease in the ground state contribution, and consequently also in the total S-factor, after the experiment of Schröder et al.[38] and the still large uncertainty, especially between LUNA and TUNL, which is the main motivation for the re-measuring of the reaction with a special setup.

The experiments that directly measured the reaction cross section are described in the subsequent paragraphs, before discussing the present, new study. The experiment [38] from 1987 was performed in three different facilities in Münster, Bochum and Toronto and covered a wide energy range from  $E_p = 0.18$  to 3.6 MeV. The characteristics of the

Facility	Energy range $E_p$	$E_p$ spread	$\Delta E_p$	Max $I_p$
350 kV Universität Münster	0.18–0.35 MeV	<0.5 keV	<1 keV	320 $\mu$ A
1 MV JN Van de Graaff, Univ. of Toronto	0.27–1.1 MeV	<1 keV	<2 keV	160 $\mu$ A
4 MV Dynamitron tandem, Ruhr-Universität Bochum	0.8–3.6 MeV	<3 keV	0.4%	40 $\mu$ A
(present) LUNA 400 kV, Gran Sasso (Italy)	0.15–0.4 MeV	0.1 keV	0.3 keV	500 $\mu$ A
(present) 3 MV Tandetron, Dresden	0.27–2.5 MeV	1.1 keV	$\leq 0.4\%$	15 $\mu$ A

Table 1.4: Beam properties at the three facilities used in the experiment in [38]: (from second to last column to the right) proton energy ranges, spread, energy calibration uncertainty  $\Delta E_p$  and maximum beam intensity  $I_p$ . In the last two rows, the same is shown for the present facilities for comparison.

three accelerators involved are summarized in table 1.4 and compared with the two used in the present work. Solid and gas targets were used to obtain the excitation function: as to the solid targets, two different kind of targets were employed. The first set was obtained by evaporating a thin Ti layer on thick Ta backings and nitriding it in a nitrogen atmosphere by resistance heating. These thin TiN targets (10 keV at  $E_p = 278$  keV) were used for  $E_p < 400$  keV and high intensity beam at the 350 kV Münster accelerator, because of their good stability versus beam dose. In addition, a windowless extended gas target was used.

At higher energy, beam induced background from the  $^{15}\text{N}(p,\alpha\gamma)^{12}\text{C}$  reaction becomes important. In order to have  $^{15}\text{N}$  depleted targets, a second set of targets was prepared by implanting  $^{14}\text{N}$  ions at  $55 < E_{^{14}\text{N}} < 200$  keV on Ta backings because nitrogen gas depleted in its  $^{15}\text{N}$  isotope was not commercially available. Following target profiles based on resonance scans showed the  $^{14}\text{N}$  atoms nearly homogeneously distributed over a thickness of 50 keV at  $E_p = 278$  keV, with a stoichiometry of circa  $\text{Ta}_1\text{N}_{1.5}$  and the content of the isotope 15 reduced by two orders of magnitude with respect to the natural abundance.

One to four Ge(Li) detectors with volumes 80 to 104 cm<sup>3</sup> (corresponding to 20–26% relative efficiency) surrounded the target chamber at close distance (2 to 4 cm) at different angles (0°, 45°, 90°, 135°), which allowed for angular distribution measurements. No anti-Compton shields were used.

The data from primary and secondary  $\gamma$ -ray transitions were both analyzed and found in agreement with each other. The statistical uncertainty was in most cases around 10% for the off resonance data. The absolute cross section at  $E_p = 813$  keV was obtained with methods relative to known resonances (13% systematic error) and used as a reference for the other data.

The data from this experiment underwent some corrections after their publication. The true coincidence summing-in effect on the  $\gamma$ -ray emission corresponding to the capture to the ground state transition had not been taken into account in the original analysis and was corrected for by the authors in [36, 35], before performing the R-matrix fit. In addition, a renormalization of all data based on a more precise reference data made



available later on is recommended in [31].

The LUNA (Laboratory for Underground Nuclear Astrophysics) experiment [36, 35] was performed in the Gran Sasso National Laboratories underground, where 1400 meter rock thickness reduces the cosmic ray-induced background. The proton beam of up to  $500\ \mu\text{A}$  intensity was provided by a 400 kV electrostatic accelerator and sent to solid TiN targets. The targets were fabricated with the reactive sputtering technique [50] on Ta backing, with typical 80 keV thickness at the  $E_p = 278\ \text{keV}$  resonance. The stoichiometry was measured via Rutherford backscattering and found to be  $\text{Ti:N} = 1:1.1$ . The information was used as an input to measure the resonance strength  $\omega\gamma = 12.9 \pm 0.4(\text{stat}) \pm 0.8(\text{syst})\ \text{meV}$  [35].

The excitation functions were obtained in the energy region  $140 < E_p < 400\ \text{keV}$  by measuring the photons with a 126% rel. efficiency HPGe detector surrounded by 5 cm lead shield and placed at  $55^\circ$  with respect to the beam direction, at 1.5 cm from the target. The distance from the target was increased to 20 cm to study the branching ratios on the resonance, in a configuration of reduced true coincidence summing-in effect. Three detectors at distance 7 cm and angles 0, 90 and 125 degrees were used to study the angular distribution at a few energies off resonance [51].

At the Triangle University Nuclear Laboratory (TUNL) facility [37], a 1 MV Van de Graaf accelerator provided proton beams with intensity 100-150  $\mu\text{A}$  and  $155 < E_p < 524\ \text{keV}$ . Solid targets were fabricated by implanting nitrogen ions into tantalum backings at different energies, obtaining thickness from 5 to 18 keV measured at the  $E_p = 278\ \text{keV}$  resonance. The resonance strength was found to be  $\omega\gamma = 13.5 \pm 1.2\ \text{meV}$ , this uncertainty mainly coming from the systematic uncertainty on the energy loss in the material. The  $\gamma$ -rays were detected in a 135% HPGe detector placed at  $0^\circ$  with respect to the beam direction, at a distance of 0.9 cm from the target. A long annulus of NaI(Tl) enclosed both target chamber and germanium detector, acting as cosmic-ray veto but also affecting the events producing  $\gamma$ -ray cascades. The branching ratios on resonance were measured after increasing the distance of the detector from the target to 23 cm, again to reduce the summing effects. No angular distribution was measured and the excitation functions were obtained considering the secondary emitted photons, assumed to be isotropic (from calculation).

In the configuration of detector at close distance, that was used for the cross section determination, both experiments at LUNA and TUNL suffered from a large true coincidence summing-in correction to be applied to the capture to the ground state. The effect increases with the detection solid angle, i.e. by placing a large detector volume at close distance from the source of  $\gamma$ -rays. For LUNA the correction amounted to 130-180% of the signal for beam energies in the region above the resonance in  $300 < E_p < 400\ \text{keV}$ , and was larger than 2 times the signal below the resonance energy (tab. 1.5), due to the smaller branching ratio of the ground state  $BR_{\text{GS}}$  with respect to all other transitions

LUNA [35] S-factor data				
$E$	$S_{\text{GS}}(E)$	$\Delta S_{\text{GS}}(E)$	$BR_{\text{GS}}(E)$	$SumIn_{\text{calc}}$
118.9	$0.040 \pm 0.030$	75%	2.4%	200%
157.0	$0.015 \pm 0.004$	27%	0.7%	670%
311.4	$0.073 \pm 0.008$	11%	2.6%	170%
350.3	$0.045 \pm 0.003$	7%	2.8%	170%

Table 1.5: Summing-in corrections for S-factor data for capture to the ground state from LUNA-2005 [35]. The two cases below resonance corresponds to the lowest investigated energy and the worst case for the summing-in effect. The corrections  $SumIn_{\text{calc}}$  have been calculated as in eq. (2.11), based on literature branching ratios  $BR_{\text{GS}}(E)$  [35] and detection efficiencies in close geometry (1.5 cm from target) from [52]. The pairwise angular correlation of the  $\gamma$ -rays in cascade has been neglected.

at those energies. Similar values apply for the TUNL experiment. The detectors were moved to “far” geometry only for on-resonance data.

LUNA and TUNL experiments agree well on the strength of the  $E_p = 278$  keV resonance and the branching ratios (tab. 2.22 in section 2.8) and fairly well on the experimental data in the overlapping energy range for all transitions. However, the extrapolated S-factor  $S_{\text{GS}}(0)$ , the second most important contributor to the total S-factor  $S_{\text{tot}}(0)$ , shows a strong discrepancy (see tab. 1.3). One reason for this factor two difference, given that the data themselves are not in disagreement, resides in how the sets of data were used in the R-matrix framework. Whereas LUNA performed a global fit, based on its own and the high-energy Schröder et al.[38] data corrected for summing-in, the TUNL group applied the same general procedure and starting values [45] as the LUNA fit, assuming some parameters fixed from previous analysis [45], but considering in their R-matrix fit only their own data set (more details in section 4.2).

However, the discrepancy can also arise from an underestimation of the errors in the data themselves, namely the error coming from the strong summing-in correction that had to be applied in both analyses. Angular pairwise correlation of  $\gamma$ -rays in cascade being emitted at the same angle, even though smeared out by the large solid angle, affects directly the calculated summing (eq. 2.11). It was assumed to be negligible for all the transitions in both LUNA-2005 and TUNL analyses. However, that is for sure not the case on the resonance, where it was measured [53] and found to be  $\approx 10\%$  different from the uncorrelated case for the two most intense  $\gamma$ -cascades. For reactions off resonance, a correlation is also expected based on calculations in the present work (appendix A).

The angular pairwise correlation changes the summing-in effect by about 10% both on and off resonance. This value can be used as a good estimation of the uncertainty on the correction applied in both experiments and results in about 17% relative error on the cross section data obtained above the resonance, in the same energy region investigated

Group	Method	Data base	$\Gamma_{\gamma,6792}$	$S_{\text{GS}}(0)$
Schröder et al. [38]	Breit-Wigner fit	Schröder et al. uncorrected	$6.3\pm 1.9$	$1.55\pm 0.34$
Texas A&M [46]	R-matrix fit	Schröder et al. uncorrected	0.35	$0.15\pm 0.07$
LUNA [36]	R-matrix fit	Schröder et al.+LUNA	$0.8\pm 0.4$	$0.25\pm 0.06$
TUNL [37]	R-matrix fit	TUNL	1.7–3.2	$0.49\pm 0.08$
Solar Fusion II [31]	R-matrix fit	Schröder et al.+LUNA+TUNL	1.2	$0.27\pm 0.05$

Table 1.6: Gamma width  $\Gamma_{\gamma,6792}$  [eV] of the state at 6792 keV in  $^{15}\text{O}$  and extrapolated  $S_{\text{GS}}(0)$  [keV barn].

presently, and much more for the data sets below the resonance, leading to an error in most cases larger than the quoted one (tab. 1.5).

Finally, a direct measurement covering the lowest energy range was performed at LUNA, with a nitrogen gas target and a BGO surrounding detector [54, 55]. Data points of less than 10% statistical uncertainty were obtained at proton energy down to  $E_p = 80$  keV, where the cross section is less than 1 picobarn. The measurement was possible thanks to the negligible laboratory background in the  $\gamma$ -ray spectra for  $E_\gamma > 5$  MeV, a consequence of the strongly suppressed cosmic radiation (muons) in the LUNA underground facility [56]. The data agree with previous experimental data in the overlapping energy region and extend the direct knowledge of the reaction cross section down to  $T_6 = 60$  with no need of extrapolation. The temperature corresponds to the H shell burning scenario of AGB stars and influences the dredge up events. The experimental results provided also an independent cross check of both previous data and R-matrix fits. However, this check could be done only on the sum of the single contributions to the total cross section, leaving the factor two discrepancy between LUNA and TUNL results on the  $S_{\text{GS}}(0)$  unsolved.

The goal of this thesis is to increase the precision for the  $^{14}\text{N}(p,\gamma)^{15}\text{O}$  reaction cross section, first of all by solving the  $S_{\text{GS}}(0)$  discrepancy. In addition to more reliable ground state data, the precision of the extrapolated S-factors can be improved by more precise information of the resonance strengths and a new measurement of high energy off-resonance data, possibly with lower uncertainty than the only data set up to now present in literature [38]. It underwent several corrections after publication.

The information on the resonances, beside directly influencing the R-matrix extrapolation to lower energy, can be used as normalization point for the off-resonance data. In fact it is easier to calculate a relative yield ratio with respect to the closer resonance strength instead of having to deal each time with an absolute measurement starting from target information.



# Chapter 2

## $^{14}\text{N}(\text{p},\gamma)^{15}\text{O}$ experiment at LUNA, $E = 0.3 - 0.4 \text{ MeV}$

The first experiment described in the present work was performed at the LUNA (Laboratory for Underground Nuclear Astrophysics) facility in Italy, up to now the only underground accelerator worldwide. An intense proton beam from the LUNA 400 kV electrostatic accelerator was sent on solid TiN sputtered targets. The prompt photons emitted from the reaction were detected with an anti-Compton vetoed composite germanium detector, with considerably reduced summing corrections with respect to previous studies.

The reaction  $^{14}\text{N}(\text{p},\gamma)^{15}\text{O}$  has been studied at three energies above the  $E_p = 278 \text{ keV}$  resonance. The cross sections for capture to the ground state and to the 5181, 6172, and 6792 keV excited states in  $^{15}\text{O}$  have been measured in absolute, based on the information on target content, beam current and efficiency. The S-factor for capture to the ground state has also been determined relative to the well-known capture to the 6792 keV excited state, solving a discrepancy in literature of a factor two on the extrapolated  $S_{\text{GS}}(0)$  value. In addition, the branching ratios for the decay of the  $E_p = 278 \text{ keV}$  resonance have been remeasured in a condition of almost negligible summing-in correction.

## 2.1 Experimental Setup

### 2.1.1 Underground laboratory

The LUNA facility is housed at the Laboratori Nazionali del Gran Sasso (LNGS) underground laboratory in Italy, located in the core of the Gran Sasso mountain, and reachable with the double tunnel-highway passing through it. The rock thickness is 1400 m, that corresponds to a 3800 m.w.e. (meters of water equivalent) shielding. It reduces the fluxes of neutrons and muons by respectively three and six [57] orders of magnitude with respect to the surface.

The background in a  $\gamma$ -ray detector, i.e. all the events that do not belong to the

reaction of interest, is made of laboratory and beam-induced background. The latter is produced by the beam interacting with the setup materials or impurities in the targets. The laboratory background is produced by all the events occurring in the environment where the setup is installed, when no beam is present, and it has two sources. The  $\gamma$ -ray lines at  $E_\gamma < 3\text{MeV}$ , from the decay of radioisotopes, such as  $^{40}\text{K}$  or belonging to the natural decay chains of Thorium and Uranium, in the rocks, air (Radon), building materials or detector itself. Some more events are caused by energetic neutrons that are produced by  $(\alpha, n)$  reactions.

The remaining background is due to the cosmic radiation: high-energy charged particles from outer space, mainly protons, interact with the nuclei in the atmosphere and produce showers of secondary radiation. At sea level it mainly consists of muons and electrons, the former being very penetrating. The interaction of muons in the detector volume may be direct, producing ionization or bremsstrahlung by losing energy, or indirect by generating prompt or delayed radioactivity following muon spallation  $(\mu, n)$  on nuclei. At the surface of the Earth muons are the main source of events at  $E_\gamma > 3\text{MeV}$ : they are reduced by three orders of magnitude with respect to the surface in such an underground facility [56].

For the present detector a factor  $10^3$  background reduction in the high-energy region has also been observed. On the other hand, the low-energy  $\gamma$ -lines from the decay of radionuclides are almost unchanged by going underground. However, the  $\gamma$ -ray continuum in this range is reduced by a factor three with respect to the runs at the surface [58], again due to the reduced contribution of the muons.

The main activity of the LNGS lab is not nuclear astrophysics: experiments in other fields of physics are performed there, that need the extremely low background in order to detect the rare events caused by e.g. dark matter, neutrinoless double  $\beta$  decay and solar neutrinos.

### 2.1.2 Accelerator and beam line

The LUNA setup is located in a connection tunnel and the whole setup is contained in a room. During beam operation, the control of the accelerator and data acquisition are performed in a close-by separated room. The whole electrostatic 400 kV accelerator [59] is embedded in a tank filled with a mixture of  $\text{N}_2$  and  $\text{CO}_2$  gas at 20 bar for insulation. The high voltage is generated by an Inline-Cockcroft-Walton power supply and the radio frequency (RF) ion source can provide hydrogen or helium beams of high intensity. The accelerator can deliver on the target up to 0.50 mA  $\text{H}^+$  and 0.25 mA  $\text{He}^+$  in the energy range between 150 and 400 keV, with 300 eV accuracy on the absolute value of the beam energy, 100 eV energy spread and 5 eV / hour long term stability. The values had been determined experimentally [59] using reactions with well known narrow resonances in that energy range.

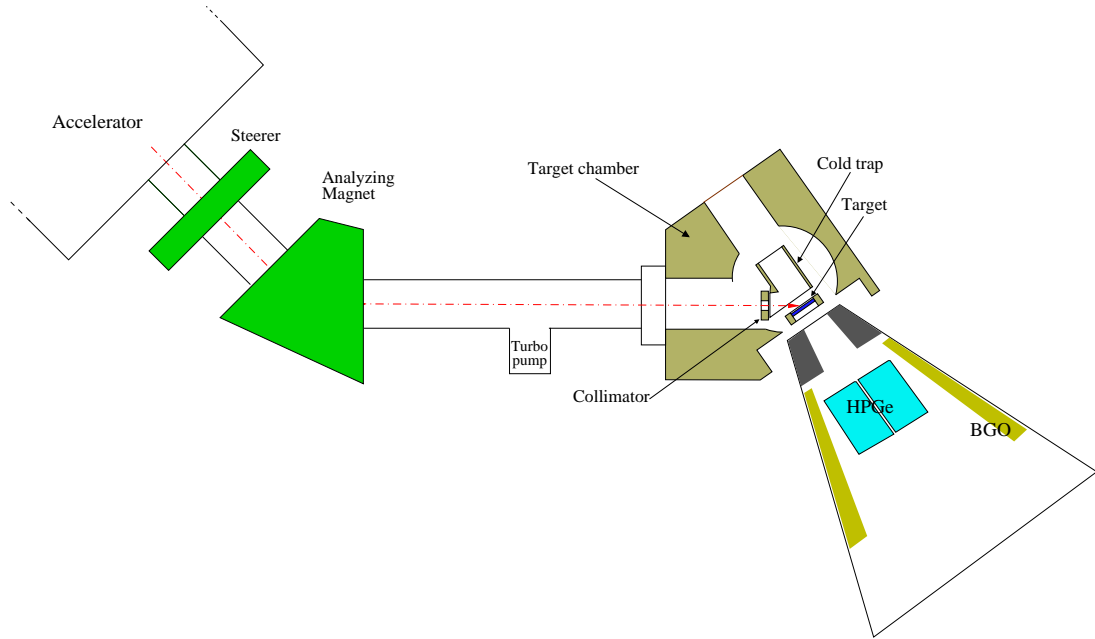


Figure 2.1: General scheme of the setup: beam transport, target chamber and detector. A detailed structure of the detector is shown in fig. 2.4, section 2.1.4.

During the experiment, the LUNA2 400 kV accelerator provided a  $H^+$  beam of  $E_p = 359, 380, \text{ and } 399 \text{ keV}$  respectively, with 0.25-0.45 mA intensity. A rough scheme of the setup is given in fig. 2.1 and a photo in fig. 2.2. After passing through a vertical steerer and an analyzing magnet at  $45^\circ$ , the ion beam passes a collimator of 5 mm diameter, which absorbs a few percent of the full beam intensity, and a cold trap cooled by liquid nitrogen to prevent Carbon build-up, before hitting the target. The targets were installed on a movable and water cooled target ladder that allowed to successively use up to three different targets, without breaking the vacuum. The target ladder was located close to the 1 mm thick Al wall of the chamber at  $55^\circ$  with respect to the beam axis, right in front of the detector. A beam wobbling was applied on x- and y-axis to homogeneously distribute the beam intensity on target. The number of ions deposited was measured with the Faraday cup current method and the accumulated charge was collected in a current integrator. Secondary electrons emitted from the target surface were suppressed by applying -300 V suppression voltage to the cold trap. Because of imperfections in the Faraday cup formed by cold trap and target, the current reading in some runs showed sudden changes, from few to tens of percent from the average value. A measurement of the reaction yield during such instabilities indicated that the proton rate at the target did not change within 1.6% statistics error. Based on that and on the observed long-term monotonous decrease of the yield due to target degradation, 5% uncertainty is adopted for the absolute current measurement, and 2% for the reproducibility of the current from run to run.

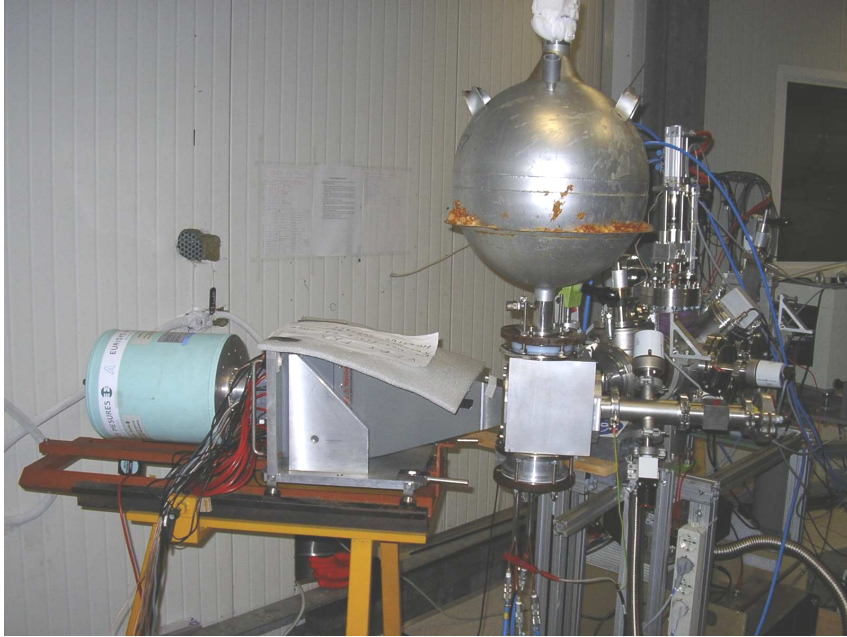


Figure 2.2: Photo of the Clover-BGO detector system positioned close to the target chamber: the detector dewar and the liquid nitrogen buffer for the cold trap are visible.

### 2.1.3 Targets

Titanium nitride (TiN) targets produced by reactive sputtering [50] on 0.2 mm thick Ta backings at Laboratori Nazionali di Legnaro were used for the experiments. The target was placed with its normal at  $55^\circ$  relative to the beam axis and had 60 keV energetic width at the  $E_p = 278$  keV resonance, when irradiated under  $55^\circ$  angle.

In order to properly correct for the degradation of the target under intense proton bombardment, its profile was monitored every day during the experiment by scanning the  $E_p = 278$  keV resonance. The beam energy was set to a few keV less than the energy of the resonance and increased by steps of one to a few keVs. The counts integrated in the wide  $\gamma$ -energy region at  $E_\gamma > 4.5$  MeV up to 8 MeV were considered, which included the events from all high-energy photons only due to  $^{14}\text{N}(p,\gamma)^{15}\text{O}$ . These counts divided by the charge were recorded for each step to give the plot in figure 2.3. Each point is related to the target composition at a certain depth: higher energy points corresponds to layers deeper in the target. The sudden increase of yield at  $E_p = 340$  keV is due to the  $E_p = 342$  keV resonance in the  $^{19}\text{F}(p,\alpha\gamma)^{16}\text{O}$  reaction, producing photons of  $E_\gamma = 6.13$  MeV. The sharp low-energy edge of the profile is given by the convolution of the 0.1 keV energy spread of the beam [59] and the  $(1.03 \pm 0.05)$  keV natural width of the resonance [35] (laboratory frame). The height of the constant plateau is proportional to the inverse of the effective stopping power per  $^{14}\text{N}$  nucleus in the compound (eq. 3.5 in sect. 3.4).

For the present purpose, the precise stoichiometry was obtained based on the stopping power at the resonance energy and the strength of the resonance used for the scan. For



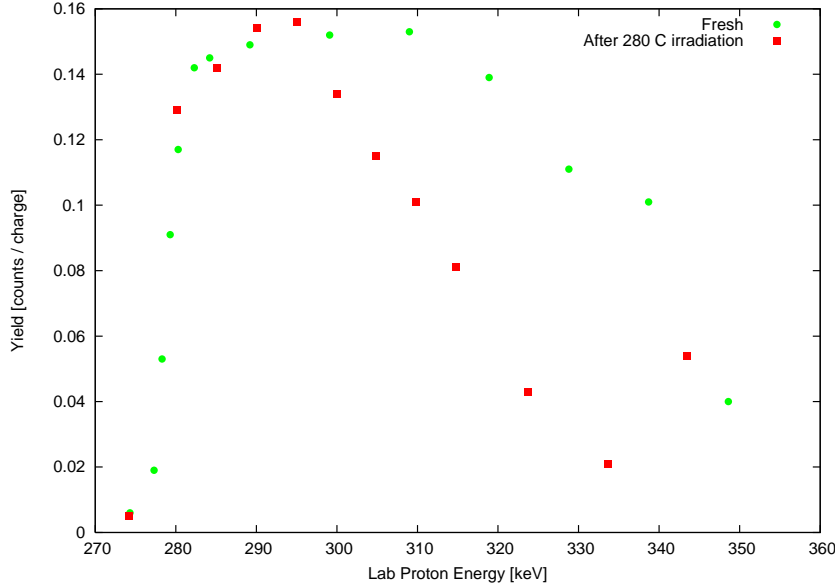


Figure 2.3: Scans of TiN target #16 at the beginning and after 280 C beam dose.

the stopping of protons in titanium and nitrogen, the values from the SRIM software [60] have been used. For the strength of the resonance,  $\omega\gamma = 13.1 \pm 0.6$  meV was adopted, the recommended value from Ref. [31]. Based on these numbers, a stoichiometric ratio Ti:N of  $1:(0.93 \pm 0.07)$  has been determined for the fresh target #16. This error is made up mainly by the uncertainties on  $\omega\gamma$  and the 5% on absolute beam current. However, this value is not entering the present analyses. No information on the beam enters the relative analysis at all. The charge measurement must only be reproducible (2% error, tab. 2.23) from run to run in the absolute analysis, lowering the contribution of stoichiometry to the systematic uncertainty to 6%.

An average reduction of 7% in the integral of the target profile was observed from day to day, with a typical dose of 24 C ( $1.5 \cdot 10^{20}$  H<sup>+</sup> ions) brought on the target per day. Based on these considerations, it is estimated that the change of the target composition relative to its original composition is known with 5% precision for any given time during the experiment.

#### 2.1.4 The Clover composite detector

The  $\gamma$ -rays emitted following the radiative captures occurring at the target position were detected in a Eurisys Clover-BGO detection system [61, 62, 63], property of the Institute of Nuclear Research ATOMKI in Debrecen (Hungary). It was placed at an angle of 55° with respect to the beam axis, with front end of the crystals at 9.5 cm distance from the target (**close geometry** configuration). The distance was increased to 19.5 cm (**far geometry**) for the measurement of branching ratios on the resonance, in order to decrease the summing correction.

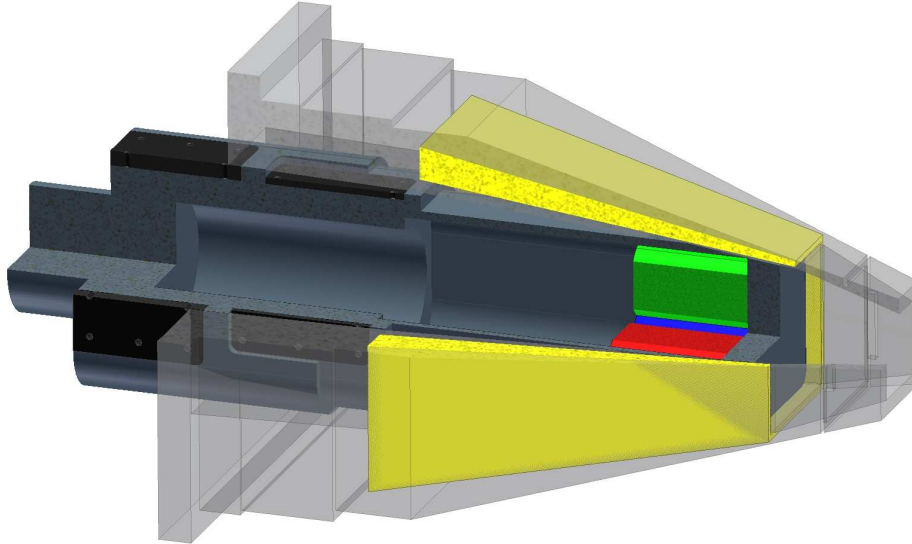


Figure 2.4: Scheme of the Clover-BGO system: three HPGe crystals (red, blue, green) and the BGO (in yellow) are shown (courtesy of Tamás Szücs).

This composite detector (fig. 2.4 and 2.2) is made up of four n-type HPGe crystals closely arranged as a four-leaf clover. They are mounted in the same cryostat and named red, green, blue, and black. The sum of their active volumes is about  $470\text{ cm}^3$  and the single crystals have a measured rel. efficiency of about 21% [61]. They are surrounded by a truncated pyramid-shaped structure of sixteen bismuth germanate (BGO) crystals. The BGO is used in anticoincidence to suppress partial absorption of photons, including Compton, single and double escape events, as well as any events able to trigger both HPGe and BGO, such as muons. The pyramid ends at its top with a heavy-met<sup>1</sup> collimator that shields the BGO from photons coming directly from the target, thus reducing the vetoing occurring on cascade  $\gamma$ -rays.

Standard NIM – Nuclear Instrumentation Module electronics coupled to the analog-to-digital converter (ADC) Ethernim 919E 14-bit made up the data acquisition system (DAQ), shown in fig. 2.5. The output signal from the preamplifier of each of the four Clover crystals was split into two branches, to give the singles and addback modes. The signal from the BGO crystals was combined with the HPGe pulse to produce the veto for the ADC of the addback mode. For the **singles mode**, each of the four signals was amplified and digitized separately, and the four spectra were gainmatched and summed up in the offline analysis. The **addback mode** [61] was given by the online hardware sum of coincident events in the separated crystals, via a dedicated home-made analog summing unit [63]. The resulting analog signal was amplified, digitized in a Ortec 919/919E unit [64] and with the possibility to be acquired in anticoincidence with events in the surrounding

---

<sup>1</sup>Heavy-met is a tungsten alloy, consisting of tungsten and nickel with either copper or iron.

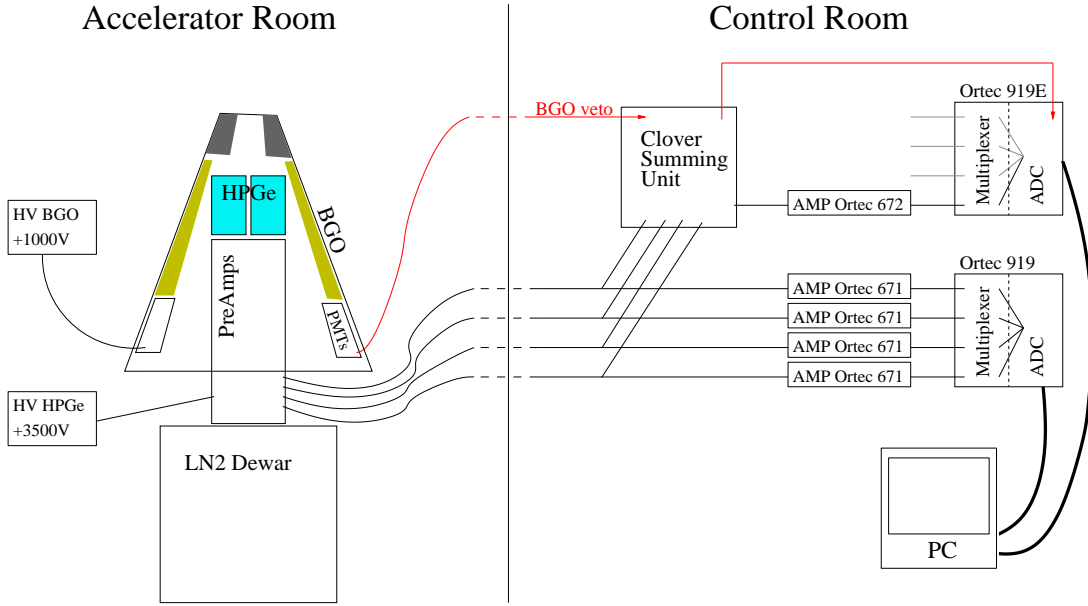


Figure 2.5: Scheme of the electronic setup: the pulse from the BGO is used as a veto to obtain the addback anticoincidence spectra.

BGO. That was done by producing a gate pulse that combined the signals from the HPGe crystals with the condition of BGO not firing (fig. 2.5). A computer-controlled multichannel analyzer accumulated all the spectra.

Typical energy resolutions for addback mode were 9 keV at  $E_\gamma = 1.3$  MeV and 12 keV at 6.8 MeV. For the singles mode the resolution was 3.3 and 6 keV. The latter resolution is better because the gain matching is much easier when summing the singles spectra offline than the matching done in the summing unit of the analog signals from the preamplifiers.

For few runs on the  $E_p = 278$  keV resonance, the free running spectra with BGO veto disabled were used in order to check the influence of BGO suppression on the lines of interest (sec. 2.2.2). The detection efficiency curve and the branching ratios were obtained from not suppressed spectra, as well.

## 2.2 $\gamma$ -ray spectra and data acquisition

The presence of the BGO veto causes not only the suppression of disturbing counts in the spectra, but also the rejection of a non-negligible amount of events of interest. A similar effect is expected from the 14-bit histogramming Ortec 919/919E unit [64], that was used instead of a full list-mode system with a separate 13-bit ADC for each channel as in [65], because it consists of a single ADC unit connected to four input channels. In order to study these issues, radioactive sources of  $^{60}\text{Co}$  and  $^{137}\text{Cs}$  as well as in-beam on resonance runs were used, and data obtained in different configurations of electronics setup were compared.

Source	$\gamma$ -energy [keV]
$^{214}\text{Bi}$	609.31
$^{214}\text{Bi}$	1764.49
$^{40}\text{K}$	1460.83
$^{208}\text{Tl}$	2614.53
in-beam	
6.17 MeV	6176.73
6.79 MeV	6796.42

Table 2.1: Spectrum lines and  $\gamma$ -ray energies [67, 35] used for the energy calibration. The recoil and Doppler corrections for the two in-beam lines have been calculated for  $E_p = 278.3$  keV.

For close and far distances geometry configuration, data were collected for the adback mode in two possible ways:

**BGO on** anticoincidence veto active, Compton suppression;

**BGO off** anticoincidence veto disabled, all events acquired;

and for the singles mode:

**all** the signals for all four crystals collected by the same multiplexed ADC;

**one** just the black segment connected to the multiplexed ADC.

The net peak area was calculated by subtracting a 'straight line' background from the raw integral of counts in a region that included the whole peak [66]. The statistical uncertainty was 1% or better for the full energy peaks in the single crystal spectra.

The contributions from all X-rays up to 50 keV emitted from both sources are negligible due to their strong absorption in the materials before reaching the detector. In this view, the cesium produces only one photon and the cobalt just two.

### 2.2.1 Gain-matching and summing of individual spectra

The spectra have been calibrated in energy based on the most intensive laboratory background lines and the lines corresponding to the 6.18 and 6.79 MeV secondary  $\gamma$ -rays, corrected for recoil and Doppler shift (table 2.1). The centroid of each peak of interest has been found through a Gaussian fit, then a linear fit of expected energies versus centroids has been adopted. This procedure was applied to many randomly selected spectra both on and off resonance, and for a long laboratory background run as well. The calibration procedure was also applied where changes in calibration had to be expected based on the logbook (changes in the setup, detector high voltage shut down, ...).

Subsequently, all spectra have been rebinned to 1 keV per bin. The four singles have been summed up to give a singles mode spectrum for each run. Finally an overall sum

Line	ADC channel	Individual spectrum	Gain-matched and summed
$^{214}\text{Bi}$ , 1238 keV	adddback mode	9.6	9.1
	red	5.0	3.3
	black	2.5	
6.79 MeV, 6796 keV	adddback mode	12.0	12.0
	red	7.0	6.3
	black	5.6	

Table 2.2: FWHM resolution in keV for individual spectra and the overall sum.

Geometry	$^{137}\text{Cs}$	$^{60}\text{Co}$	
	662 keV	1173 keV	1332 keV
close	$1.019 \pm 0.005$	$1.064 \pm 0.006$	$1.059 \pm 0.006$
far	$1.011 \pm 0.004$	$1.027 \pm 0.006$	$1.027 \pm 0.005$

Table 2.3: Ratio  $\frac{\text{BGO off}}{\text{BGO on}}$  of the full energy counting rates for different distances and sources

of the spectra for each of the three beam energies  $E_p = 359, 380, \text{ and } 399 \text{ keV}$  has been obtained, both for singles and addback mode. The width of the peaks did not increase, showing that the calibration has been done properly (table 2.2). One Clover segment (red) shows bad resolution because of a well-known defect in its preamplifier.

## 2.2.2 Addback mode: Study of the BGO veto

Couples of addback spectra in configuration BGO on and off were compared for each configuration of distance and radioactive source. The most important effect of the BGO veto is a suppression in the counts below the Compton edge and a consequent rise in the peak to Compton ratio [66, p.237], by a factor 3 (fig. 2.6). In order to study possible effects on the full energy peak area, the ratio of net full energy peak counting rates obtained for BGO off and on for different distances has been calculated. The results are summarized in table 2.3: the effect is a reduction of observed net counts in the spectra when the BGO is active. The reduction for both the cascade photons from the  $^{60}\text{Co}$  is larger than the one observed with the  $^{137}\text{Cs}$  single  $\gamma$ -ray detected and it decreases in far distance, whereas no difference due to the distance is observed in the case of the  $^{137}\text{Cs}$  source.

The reduction in the single line of the cesium source can be explained with random coincidences with the laboratory background events, which are independent from the detector's position. Assuming a background trigger rate of 500 Hz in the BGO crystals and  $20 \mu\text{s}$  for the average duration of the BGO veto, a no-acquisition time of 0.01 s in 1 second is calculated for the addback mode. This expected 1% effect is consistent with the observed average  $(1.2 \pm 0.3)\%$  for  $^{137}\text{Cs}$ . As a confirmation, the same value has

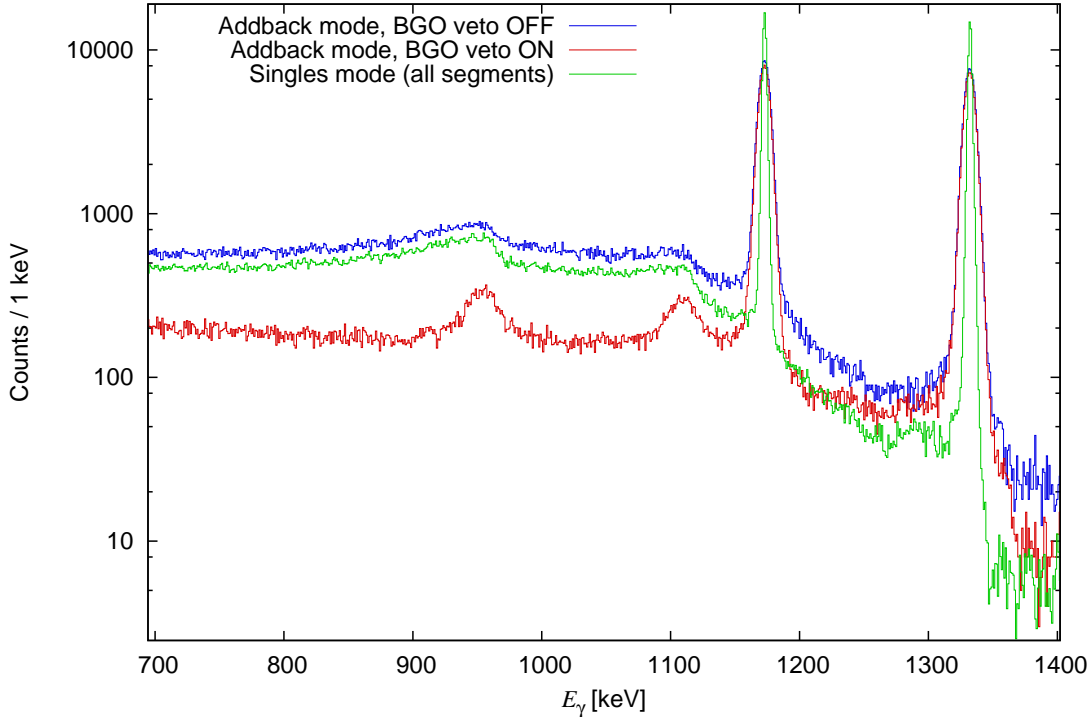


Figure 2.6: Comparison between addback mode spectra for  $^{60}\text{Co}$  source in close geometry: notice the effect of BGO suppression in the Compton region. The singles mode spectrum is also shown: notice the smaller detection efficiency of full energy events and its superior energy resolution.

been measured also for the peak at 1461 keV corresponding to the decay of  $^{40}\text{K}$  in the background spectra.

For cobalt there is an additional 2 to 5% reduction of the measured counts with BGO on, depending on the geometry. This effect is due to true coincidence with events detected in the BGO caused by the other cascade  $\gamma$ -ray entering the detector. The effect decreases with increasing distance, most probably due to the different probability for those events in a different configuration of the detector with respect to the source (solid angle  $\propto 1/r^2$ ).

As to the in-beam case, by considering two BGO off runs on resonance and the correspondent BGO on runs acquired right after or before, it was possible to verify the suppression of events in the full energy peaks for the three most important cascade transitions. A slight difference with respect to the value found with cobalt was observed (table 2.4) and especially a big difference in suppression between primary and secondary emission for 6.79 MeV transition is observed. That may be due to two reasons: one is that the heavy-met collimator absorbs more effectively 765 keV  $\gamma$ -rays than a few MeV ones, thus allowing more photons to reach the BGO and the corresponding low-energy photons to be vetoed. The second reason is that high-energy  $\gamma$ -rays have a higher probability to generate further  $\gamma$ -rays through e.g.  $e^-e^+$  pair production and Compton, and reach the BGO crystals with respect to the low-energy ones.

Line	$E_\gamma$	$\frac{\text{BGO off}}{\text{BGO on}}$
6.79 primary	765.4	$1.083 \pm 0.006$
6.79 secondary	6796.4	$1.047 \pm 0.012$
6.17 primary	1385.3	$1.077 \pm 0.004$
6.17 secondary	6176.7	$1.066 \pm 0.008$
5.18 primary	2377.6	$1.060 \pm 0.009$
5.18 secondary	5184.7	$1.080 \pm 0.017$

Table 2.4: Effect of the BGO anticompton shield in suppressing the full energy peak areas of three most important transitions 1.4, for in-beam on-resonance runs in close geometry.

### 2.2.3 Singles mode: Study of the ADC multiplexer

A multiplexed ADC is the heart of the Ortec 919/919E multichannel analyzer unit. Four input channels are all connected to a single ADC component. Since coincident events from cascade photons are expected in the present experiment, the influence of the multiplexer on the detected counting rate in the singles mode spectra has been investigated. Different combination of radioactive sources, distances and in-beam runs were considered. Two measurements for each case were performed: one with only one channel connected to the 919 unit and one collecting all four signals coming from the single crystals. Consequently, in the first case only the black segment spectrum is present, in the other case all four spectra are available.

A first understanding of how the multiplexer operates comes from the analysis of the dead time in the two electronics configurations. The 16k-channel ADC has a constant digitization time  $< 7 \mu\text{s}$  [64], and the 919 unit furnishes a dead time correction based on the Gedcke-Hale method. An average time needed to process one event  $\tau$  has been calculated for all spectra, given by the difference between real and live time quoted by the 919 unit ( $t_{\text{real}}$  and  $t_{\text{live}}$ ) divided by the total number of events acquired in one spectrum  $\text{counts}_{\text{all spectrum}}$ :

$$\tau = \frac{t_{\text{real}} - t_{\text{live}}}{\text{counts}_{\text{all spectrum}}} \quad (2.1)$$

Both for single crystal alone and for the addback sum with BGO anticoincidence off,  $\tau = 19 \pm 1 \mu\text{s}$  is found. This value can be considered the reference or normal behavior of the electronics. For addback spectra with BGO on,  $\tau$  is  $35 \pm 5 \mu\text{s}$ . This higher value can be expected due to the larger time window of the gate signal when the BGO veto is active. When all four channels are active,  $\tau = 87 \pm 5 \mu\text{s}$ , much higher than before. This is explained by the fact that about four times more input pulses from all the HPGe crystals require accordingly longer time to be processed in the only ADC available. As a check, if  $\text{counts}_{\text{all spectrum}}$  is substituted with the total number of events in all four crystals' spectra,  $\tau = 21 \pm 2 \mu\text{s}$  is obtained again, in good agreement with the reference behavior. The results are the same for runs with radioactive sources, in beam and with laboratory background.

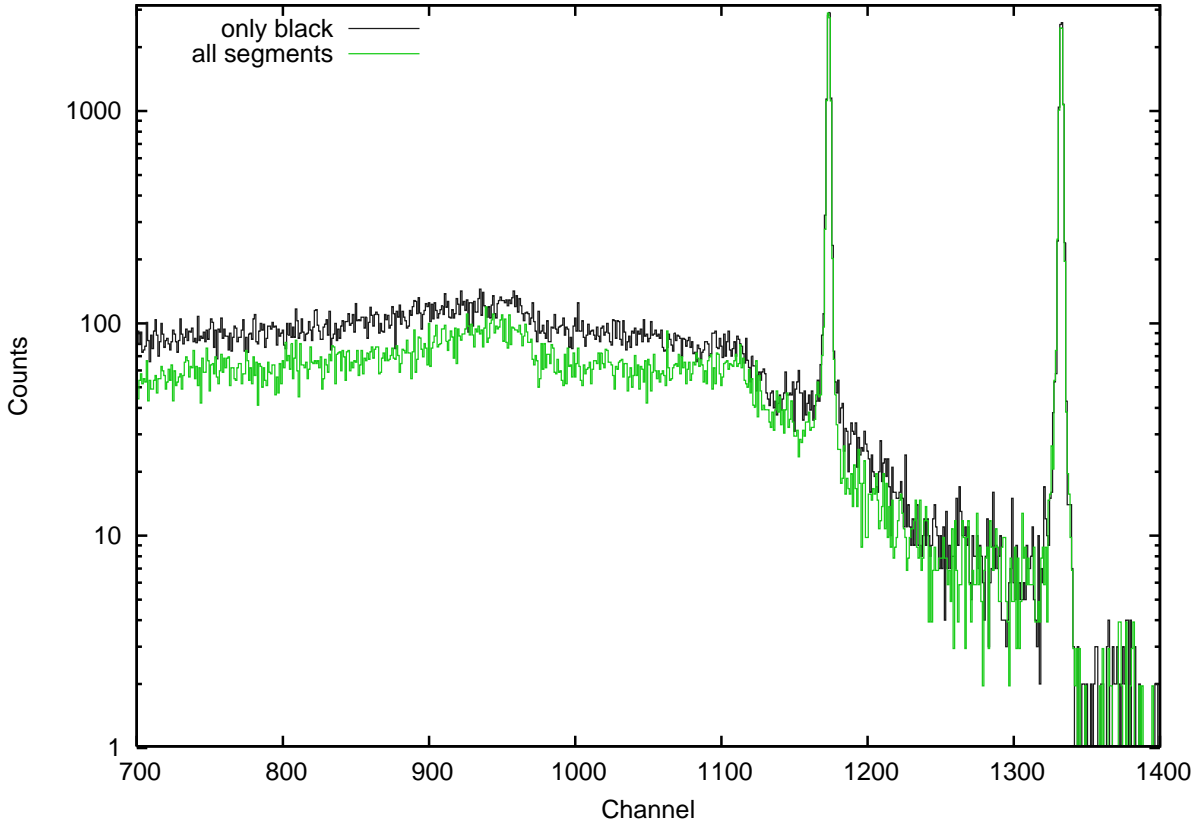


Figure 2.7: Comparison between two black segment spectra for  $^{60}\text{Co}$  source (after live time normalization) in close geometry, with only one segment and with all segments acquiring. The effect of the multiplexer is visible in the suppression of the Compton region.

The effect of the multiplexed ADC is visible from the comparison of spectra in figure 2.7. When switching from only one channel to all four channels running, the events in the “Compton region” are reduced and the peak to Compton ratio [66, p.237] increases by  $(34\pm 4)\%$  both for  $^{137}\text{Cs}$  and  $^{60}\text{Co}$ . Since there is one ADC and four channels connected to it through a router, in case of simultaneous input signals only one of the two or more coincident pulses is processed, the others are lost. If a photon interacts but is not fully absorbed in one crystal, which corresponds to an event in the “Compton region”, it may result in a second event in a nearby Ge crystal. For the detectors, the second event is simultaneous with the first, therefore one of those two events is not processed by the multiplexed ADC and will not appear in the spectrum of one of the two segments.

As to the full energy peak areas, the observed counting rate for  $^{137}\text{Cs}$  does not change in the two electronics setup within 0.8% statistical uncertainty. For the two  $\gamma$ -rays from  $^{60}\text{Co}$ , the full energy peak rate decreases by  $(1.7\pm 0.7)\%$  in close geometry when all four channels are used for acquisition. A decrease  $(1\pm 2)\%$  is observed also in the 6.79 MeV  $\gamma$ -ray for in-beam runs on the resonance in close geometry.

In the case of  $^{137}\text{Cs}$ , if the single (high-energy) photon of 661.6 keV is completely absorbed as a full energy peak event, there can not be other coincidence events in nearby



crystals, so no suppression is observed. Actually random coincidences with laboratory background are expected, but the effect is negligible because the rate of such events in a single HPGe crystal is less than 10 Hz ( $\ll$  500 Hz in the BGO that accounts for 1% suppression, sec. 2.2.2).

In the case of  $^{60}\text{Co}$  and in-beam runs, there is the possibility of interaction in the crystals of  $\gamma$ -rays from the same physical cascade. A calculation has been performed to model the counting rate reduction due to this effect. Suppose that the first  $\gamma$ -ray gives a full energy peak count in one crystal. The probability, that an event due to the second  $\gamma$ -ray occurs, is the sum of the total absolute efficiencies of the other three segments, plus a small effect due to the  $^{60}\text{Co}$   $\gamma$ -rays' angular correlation [68, p.486]. Total efficiency is obtained assuming that the ratio between the total number of events in the spectrum (laboratory background subtracted) and the peak areas is the same for all segments. After calculating this ratio for the black channel when no other segments are used for acquisition, it was multiplied with the full energy peak efficiency to obtain red, green, blue segment total efficiency. Their sum after considering a further increase of 8.0%, due to angular correlation between the two  $\gamma$ -rays at  $0^\circ$  angle [68, p.486], results in 2.5% for both energies. That corresponds to the fraction of coincidence events occurring in the Clover detector per one full energy absorption.

Assuming that the ADC router randomly “decides” which channel to serve if two signals arrive simultaneously, the full energy events from the first  $\gamma$ -ray are vetoed only one half (on average) of the times there is a coincidence. Therefore, a calculated  $(2.5/2 = 1.2)\%$  is obtained for the relative reduction of the counting rate in the full energy peak, in agreement with the experimental  $(1.7 \pm 0.7)\%$ .

In order to extend the prediction to higher energy, total absolute detection efficiencies for the primary emission at energies ranging from 765 keV (on resonance) to 878 keV ( $E_p = 399$  keV) were obtained from the ratio between whole spectrum and full energy peak counts for the black segment alone. Different from the previous calculation, this latter number has been obtained interpolating between the observed ratios from the  $^{137}\text{Cs}$  and  $^{60}\text{Co}$  experiments. The full energy peak efficiencies were obtained by the singles mode efficiency curve (sec. 2.4), rescaled by a factor 0.745 to reflect only the three non-black segments (red, green, blue). Finally, an expected 1.2% reduction in the 6.79 MeV peak is obtained, consistent with the experimental number of  $(1 \pm 2)\%$  reduction.

The experimental and calculated values are summarized in table 2.5. According to these considerations, for the cross section determination based on the singles mode a  $-(1.2 \pm 0.7)\%$  correction in the counting rate of any peaks corresponding to photons in cascade is applied.

No reduction in the counting rate of the peak corresponding to ground state (GS) capture is expected, because no other coincident emissions are present if such event is acquired. The same applies when the signal is not due to a true single emission but to

Run	predicted	observed
cobalt (both peaks)	1.2%	$(1.7 \pm 0.7)\%$
resonance (6.79 MeV)	1.2%	$(1 \pm 2)\%$
resonance (GS)	none	too high uncertainty

Table 2.5: Predicted and observed reductions in the full energy peak counting rate due to the ADC multiplexer suppression.

Operation	Repositioning	Shifting target 2 mm
adddback mode	$1.1 \pm 0.6$	—
red	$2.5 \pm 1.3$	$-1.0 \pm 1.3$
green	$-0.5 \pm 1.2$	$2.5 \pm 1.3$
blue	$0.4 \pm 1.3$	$0.0 \pm 1.3$
black	$2.7 \pm 1.3$	$0.4 \pm 1.3$
singles mode	$1.1 \pm 0.6$	$0.7 \pm 0.6$

Table 2.6: Change in the full energy peak rates (in %) after geometry change, for addback mode, all segments and singles mode spectra.

the summing-in of two cascade  $\gamma$ -rays that are both detected in the full-energy peak in the same segment.

## 2.2.4 Uncertainty due to geometry reproducibility issues

Some additional  $^{137}\text{Cs}$  spectra were recorded to check the change caused by just moving the detector back and forth or a shift in the target ladder. The *repositioning* procedure consisted in moving the detector to another distance after one experimental run was finished, then shifting back to the original position, with the maximum precision achievable. This procedure caused a  $(1.1 \pm 0.6)\%$  change in the peak area in the addback spectrum. For the single segments, the effect is even higher but goes in different directions depending on the segment. The effect is therefore diminished in the singles mode spectrum formed by their sum, which is finally affected by the same uncertainty as the addback mode. Shifting the target ladder 2 mm upward produces a similar effect on the counting rates of the single segments.

A summary of geometry reproducibility is given in table 2.6. Based on these experiments, an uncertainty of 1.1% resulting from geometry issues is applied for addback and singles spectra. For just one single segment, this uncertainty is 2.7%.

## 2.2.5 Summary of corrections and uncertainties due to DAQ issues

Summarizing the present section, the necessary corrections because of the use of the Ortec 919 unit depend on whether addback or singles mode is used and also on the  $\gamma$ -ray to be studied (table 2.7).

Spectrum	Effect	$\gamma$ -ray	Correction	Uncertainty
Addback mode	BGO veto	single	1.2%	$\pm 0.3\%$
		cascade	(4.7–8.3)%	$\pm(0.4–1.7)\%$
	Multiplexer		none	—
	Geometry		none	$\pm 1.1\%$
Singles mode	Multiplexer	single	none	—
		cascade	1.2%	$\pm 0.7\%$
	Geometry		none	$\pm 1.1\%$
Single	Geometry		none	$\pm 2.7\%$

Table 2.7: Summary of corrections and uncertainties adopted for the data analysis.

## 2.3 Net peak area calculation

The net counts corresponding to the capture to (and decay of) the excited levels at 6792, 6172, and 5181 keV and the ground state of  $^{15}\text{O}$  have been calculated from the  $\gamma$ -ray spectra. For each  $\gamma$ -cascade, net counts were obtained for the primary (separated into resonant and nonresonant contribution) and secondary photon emission from the decay of excited states  $E_x$  in  $^{15}\text{O}$ .

The counts of interest from the spectra are the first ingredient for calculating the reaction cross section. Care must be taken, that all and only the events belonging to full-energy events in the detector from the reaction are included. The region of interest (ROI) corresponds to the range of channels in the  $\gamma$ -spectrum where such counts are expected. For simple peaks made of events of well-defined energy, like the secondary emissions  $E_x \rightarrow 0$ , the ROI is chosen by observing the shape visible from the spectrum. In the case of the extended structure of the primary nonresonant  $\gamma$ -rays  $\text{DC} \rightarrow E_x$ , the ROI's position is selected based on the high-energy edge of the structure arising over the  $\gamma$ -continuum, which is easy to localize and that corresponded to the maximum energy calculated with the initial beam energy. The extension of the ROI depends on the target thickness observed in resonance scans performed before or after the run and the detector energy resolution.

The spectra have been checked for parasitic structure within and around the peak regions. No peaks due to beam-induced background could be found in the relevant

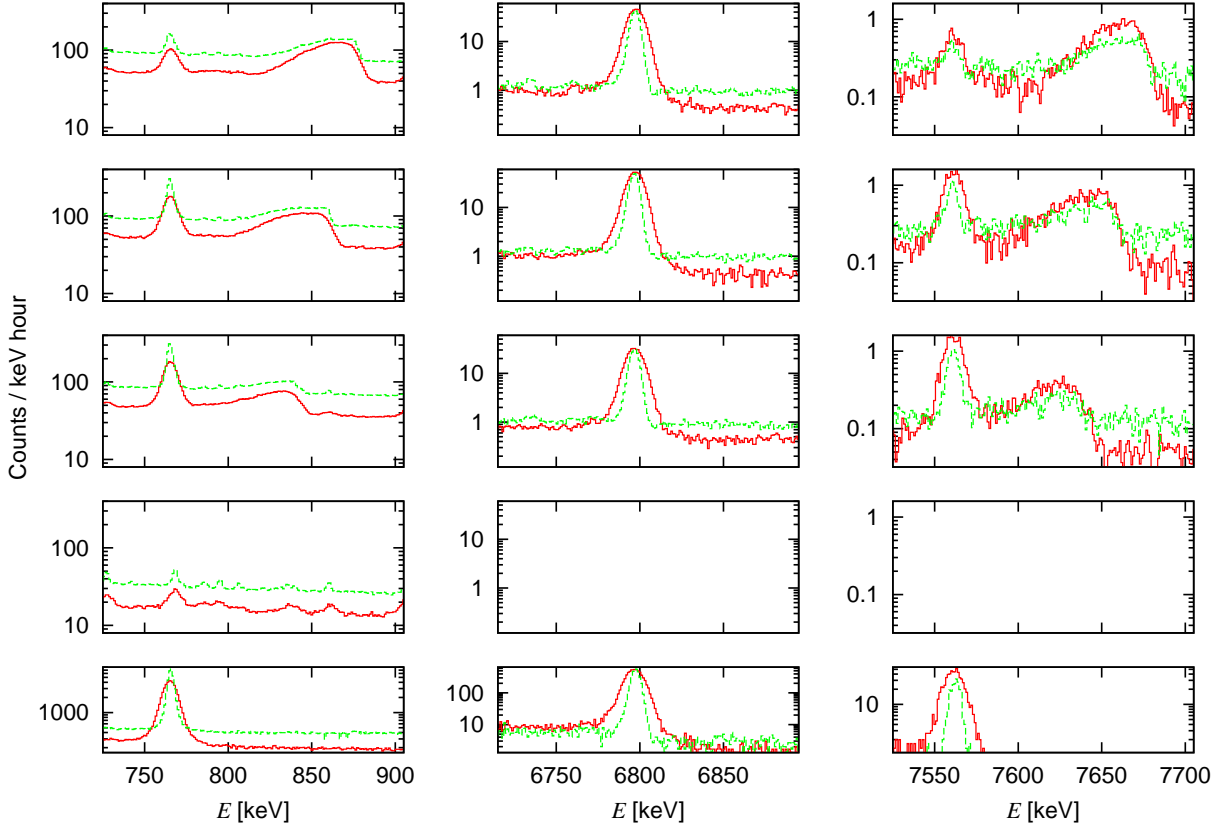


Figure 2.8:  $\gamma$ -ray spectra for adddback (red, solid) and singles (green, dashed) mode. First column: 6.79 MeV primary, second column: 6.79 MeV secondary, third column: ground state. First three rows: 399, 380, 359 keV off-resonance spectra, fourth row: laboratory background spectra, fifth row: on-resonance spectra.

regions of the  $\gamma$ -ray spectra. Also, no peak area used here is affected by single or double escape lines from higher-energy peaks.

The laboratory background affects only the low-energy part of the spectra, which is the domain of the primary  $\gamma$ -rays ( $DC/RES \rightarrow E_x$ ). In particular, the presence of the lines at  $E_\gamma = 768$  keV from the decay of  $^{214}\text{Bi}$  and at  $E_\gamma = 860$  keV from  $^{208}\text{Tl}$  complicated respectively the resonant and nonresonant part of the capture to the 6792 keV state (fig. 2.8). The worst case is represented by the primary for the capture to the excited state at 6172 keV (fig. 2.9 middle column and 2.10 left): the line at 1460.8 keV from  $^{40}\text{K}$  has a higher rate than the events of interest. A summed-up averaged laboratory background spectrum has been subtracted from the in-beam spectra, after normalizing for the different acquisition live times (fig. 2.9).

The change in the radioactivity level during the experiment has been checked. The main line from  $^{214}\text{Bi}$  had a maximum increase of  $(12 \pm 2)\%$  from the beginning to the end of the experimental campaign, probably due to different Radon concentration and ventilation in the facility. Since its contribution to the primary is less than 20%, a

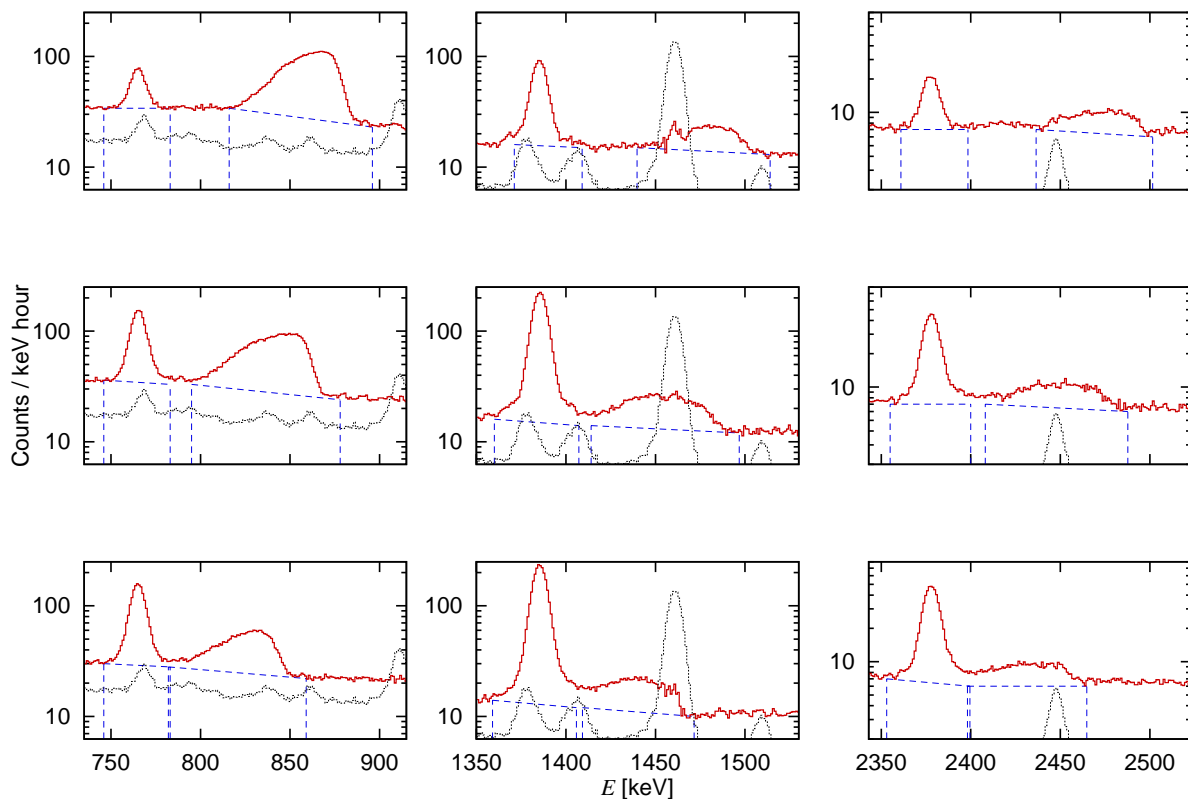


Figure 2.9: Low-energy part of the  $\gamma$ -ray spectra for addback mode (red full line) after subtraction of the laboratory background, also included (black dotted line). Rows from top to bottom:  $E_p = 399, 380, 359$  keV. Columns from left to right: Primary  $\gamma$ -ray for capture to the excited state at 6792, 6172, 5181 keV. The peak from resonant capture (by the tail of the target) is clearly visible at the left of each panel. The nonresonant capture has a shape reflecting the profile of the target, convoluted with the energy-dependent reaction cross section. Net counts have been obtained by subtracting the area (delimited by dashed blue line) in the region of interest for resonant and nonresonant capture.

maximum uncertainty of 2% has been considered on the live time-subtracted spectra. No change in time has been observed for the  $^{40}\text{K}$  line at 1460.8 keV. The uncertainties for laboratory background subtraction are in all cases smaller than the error estimated for the separation of resonant and nonresonant part and straight-line subtraction (see below).

In order to obtain the net counting rate, a straight-line background based on two flat regions to the left and right of the ROI has been subtracted from the integral over the ROI (method M1). This procedure was applied for every secondary except for the decay of the 6172 keV excited state, where a different method was applied (M2). It was repeated for each transition of the run at 399 keV, both for the primary (resonant and nonresonant) and secondary  $\gamma$ -rays.

In certain cases, it was not possible to apply the method M1. For instance, the peaks corresponding to primary transitions for off resonance runs at 359 and 380 keV could

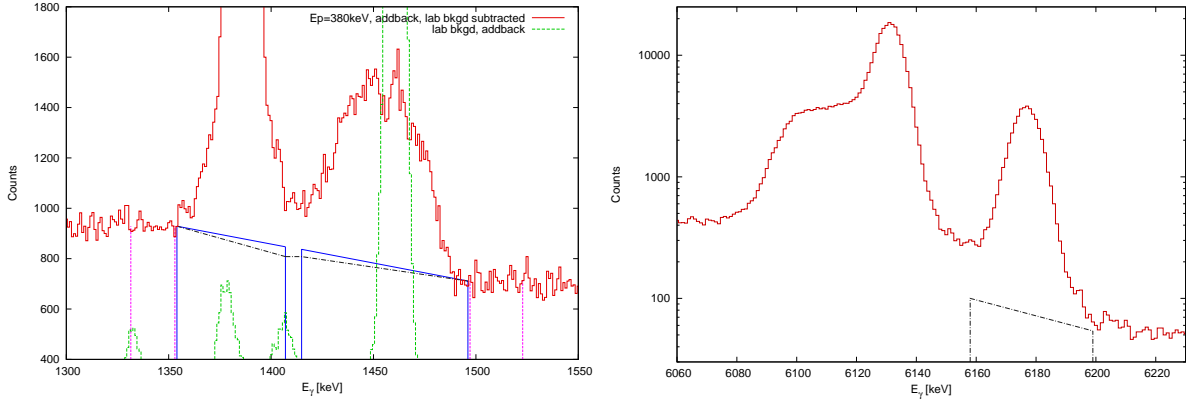


Figure 2.10:  $\gamma$ -ray spectra for addback mode, run at 380 keV (red full line) and laboratory background (green dashed line). **Left:** primary (DC/RES  $\rightarrow$  6172) peaks, region subtracted based on method M1 (solid blue line) and M2 (black dash dotted line). The pink dashed vertical lines define the regions and height of the chosen background. **Right:** secondary (6172  $\rightarrow$  0) peak, region subtracted based on method M2 (black dash dotted line). Background chosen on the region to the right of the peak.

not be easily analyzed because the resonant and nonresonant parts lie very close to each other (see fig. 2.9, last row); the effect is bigger for DC  $\rightarrow$  6172, 5181 keV captures due to the steeper rise of the S-factor towards low energy for these two transitions. A similar problem occurred also for the calculation of the net counts of the secondary  $\gamma$ -ray at  $E \approx 6172$  keV, due to the presence of an intense nearby peak (at  $E_\gamma = 6130$  keV) due to the beam-induced reaction  $^{19}\text{F}(p,\alpha\gamma)^{16}\text{O}$  (fig. 2.11). The peak is broadened due to Doppler effect, but only towards lower  $\gamma$ -energies because the majority of  $^{16}\text{O}$  nuclei emitted in the direction of the detector are completely stopped in the target before the photon is emitted. Therefore, no positive Doppler effect is observed (the lifetime of the 6.13 MeV excited state in  $^{16}\text{O}$  is 18 ps, whereas less than 1 ps is needed to stop one  $^{16}\text{O}$  nucleus of  $v/c < 0.005$  in TiN).

Whenever it was not possible to determine one of the two background regions like in the former cases, a complementary method (hereafter called M2) was used based on the ratio of the difference in average counts per channel observed to the left and right of peak  $bg_{\text{left/right}}$ , and the net area of the peak itself  $C_{\text{NET}}$ :

$$R = \frac{(bg_{\text{left}} - bg_{\text{right}})}{C_{\text{NET}}} \quad (2.2)$$

The ratios  $R$  observed in spectra acquired on the resonance, where the peaks are intense and easy to analyze, have been used to calculate the background area of peaks at same energy in the problematic spectra. A summary of the values of  $R$  used in the analysis are given in table 2.8. Notice that the values of  $R$  vary with  $E_\gamma$ , due to the different distribution of events for partial energy absorption in the detector.

For the special case of the decay of the 6172 keV excited state, where a very intense

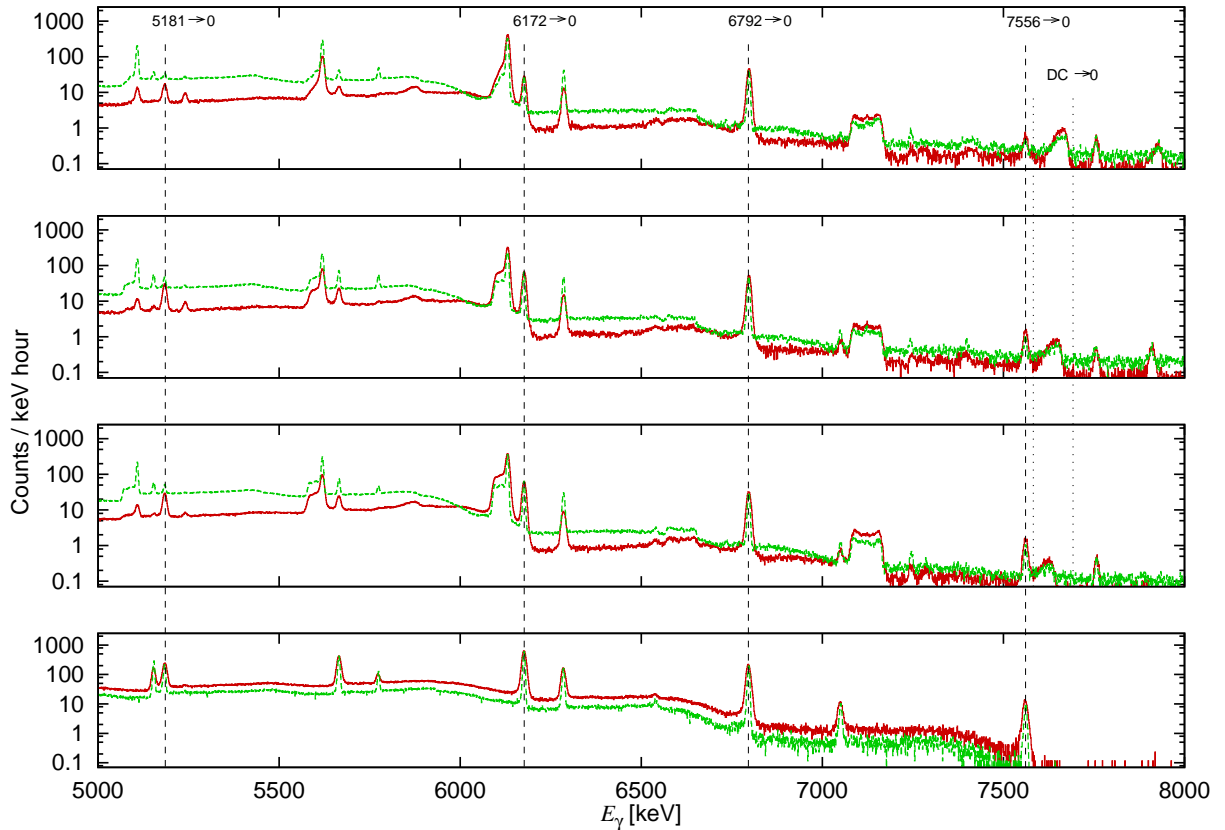


Figure 2.11:  $\gamma$ -ray spectra for addback mode (red full line) and singles mode (green dashed line). From top to bottom: Off-resonant spectra at  $E = 353, 334, 318$  keV, with the detector at 9.5 cm distance from the target. On-resonance spectrum at  $E = 259$  keV, with the detector at 19.5 cm distance from the target. Also in the off-resonance spectra (top three panels), the resonant contribution by tail of the target is well visible for the capture to the ground state. The main contaminant peaks are from the  $^{19}\text{F}(p,\alpha\gamma)^{16}\text{O}$  reaction.

peak at 6.13 MeV (from the  $^{19}\text{F}(p,\alpha\gamma)^{16}\text{O}$  beam induced reaction) is present, the net counts is the mean of values obtained with method M1 and M2, the uncertainty being the half of the difference in net counts based on one or the other method. They are considered to be the two extreme cases, corresponding to (i) no events from the 6.13 MeV peak in the ROI, even after Doppler (M2) or (ii) reasonably maximum number of events from the 6.13 MeV peak (M1).

The uncertainty has been calculated with an analytical formula based on counts and number of channels in the regions adopted for the peak and the background subtraction [66]. In cases of intense laboratory background subtraction (6.17 primary) or due to great variability of the net counts when choosing slightly different ROIs, an additional 5% error of the subtracted quantity has been included. In all other cases, at least 3% error on the subtracted counts has been taken into account.

If necessary, the final  $1\sigma$  uncertainty has been increased even more to include any dis-

$E_x$	$R \cdot 10^3$	
	DC $\rightarrow E_x$	$E_x \rightarrow 0$
6796	$1.77 \pm 0.17$	$1.05 \pm 0.07$
6176	$0.89 \pm 0.10$	$0.99 \pm 0.11$
5184	$0.89 \pm 0.08$	$0.99 \pm 0.11$
0	$1.22 \pm 0.40$	$0.00 \pm 0.00$

Table 2.8: Ratios  $R$  defined in eq. (2.2) obtained from on-resonance spectra (addback mode), for transitions to and from different excited states  $E_x$ . All ratios (and their uncertainties) are to be multiplied by a factor  $10^{-3}$ .

crepancy observed among the different results of net counts when applying other possible methods and choices of the regions.

For the following relative (sec. 2.7) and absolute (sec. 2.9) analyses, the peak corresponding to secondary emission is preferred to the primary because much less laboratory background is present in the high-energy region of the spectrum and it is usually a well defined peak, so it is trivial to obtain its area. However, this peak contains also some counts due to the 259 keV resonance, because the proton beam loses energy in the target and eventually still finds a small nitrogen concentration deep in the target when its energy corresponds to the resonance one. These events are not of interest and have been subtracted considering the ratio  $(\frac{Res}{NonRes})_{prim}$  between resonant and nonresonant counts of the primary transition, where the ratio (circa 1.06) of the detection efficiencies at the two energies (the effective energy for the nonresonant part) is already included. This ratio has been used to obtain the nonresonant part  $NonRes_{sec}$  in the total secondary peak area  $(Res + NonRes)_{sec}$ :

$$NonRes_{sec} = \frac{1}{1 + (\frac{Res}{NonRes})_{prim}} (Res + NonRes)_{sec} \quad (2.3)$$

The method is better than directly using the counts from the nonresonant part of the primary, because it relies on the factor  $1 + (\frac{Res}{NonRes})_{prim}$  which is less sensitive to their single errors. The errors have been propagated as if they were purely statistical and Gauss-like distributed, because (i) one part is pure counting statistics and (ii) the rest of the uncertainty is not, but the method is used as a conservative approach. The reason is that this second source of uncertainty is due to the separation and straight-line background subtraction procedures which are respectively negative or positive correlated. They each contribute about the same to the total uncertainty and would eventually cancel out.

The results are summarized in table 2.9, for all transitions observed in summed up spectra acquired at same beam energy. Corrections for electronics (tab. 2.7) and summing in/out effects (section 2.6.2 and 2.6.1) are taken into account. The values in the row “secondary NonRes” are the ones used for the following analyses.



run	peak	capture to GS	capture to 5181 keV	capture to 6172 keV	capture to 6792 keV
359 keV	primary Res	1284±40	45611±1727	242917±4060	132806±3351
	primary NonRes	875±60	11501±2158	44908±3551	118769±5933
	secondary Res+NonRes		27331±1406	70721±4811	39477±577
	secondary NonRes		5602±898	11330±1087	19072±611
380 keV	primary Res	735±34	27681±1404	148212±2716	80473±2546
	primary NonRes	1291±58	11267±1706	39708±3444	169122±4786
	secondary Res+NonRes		19048±865	46980±2665	40214±582
	secondary NonRes		5623±680	10251±916	27747±537
399 keV	primary Res	301±30	11017±1166	59815±2646	29482±2816
	primary NonRes	1607±59	9177±1608	23879±3713	210950±5229
	secondary Res+NonRes		10819±813	22931±2758	40084±580
	secondary NonRes		5011±666	6777±1122	35461±652

Table 2.9: Net counts already corrected for electronics and summing-in/out effects.

## 2.4 $\gamma$ -ray detection efficiency

The detection efficiency for addback and singles mode was measured at low energies with calibrated radioactive sources and extended to higher energies using the 1:1 ratio of cascade photons from the  $^{14}\text{N}(p,\gamma)^{15}\text{O}$  reaction on the  $E_p = 278$  keV resonance. The following procedure has been followed:

1. Calculate the efficiency  $\varepsilon_\gamma(E_\gamma)$  for  $^{137}\text{Cs}$  and  $^{60}\text{Co}$  sources, taking into account the corrections of table 2.7. For  $^{60}\text{Co}$ , additionally a summing-out correction is applied. Based on these three points, a linear fit curve in the double logarithmic plot is derived:

$$\log[\varepsilon_\gamma(E_\gamma)] = a' + b' \cdot \log[E_\gamma] \quad (2.4)$$

2. Calculate the ratio between primary ( $E_\gamma = 765, 1385, 2317$  keV) and secondary ( $E_\gamma = 5185, 6177, 6796$  keV)  $\gamma$ -ray for transitions through the levels at 6.79, 6.17, and 5.18 MeV. The summing-out and BGO suppression corrections have been calculated separately for primary and secondary  $\gamma$ -ray because they depend on  $\gamma$ -energy.
3. Derive the efficiencies for the 6.79 and 6.17 primaries ( $E_\gamma = 765, 1385$  keV) from eq. (2.4) and obtain the efficiencies for the 6.79 and 6.17 high-energy secondaries from the above ratios.
4. Derive a quadratic fit curve from the three radioactive source lines and the two in-beam secondary lines at 6796 and 6177 keV:

$$\log[\varepsilon_\gamma(E_\gamma)] = a + b \cdot \log[E_\gamma/6.791 \text{ MeV}] + c \cdot (\log[E_\gamma/6.791 \text{ MeV}])^2 \quad (2.5)$$

5. The reliability of the curve (2.5) is then checked using the ratio of primary to secondary  $\gamma$ -ray for the transition through the 5.18 MeV state.

Transition through	experimental	GEANT4
6.79 MeV	$6.36 \pm 0.05$	$6.33 \pm 0.09$
6.17 MeV	$3.95 \pm 0.02$	$3.92 \pm 0.04$
5.18 MeV	$2.12 \pm 0.02$	/

Table 2.10: Ratio of primary to secondary peak areas for BGO anticoincidence off, from the experiment and from a GEANT4 simulation.

The reference case for the detection efficiency curve are spectra taken with the BGO anticoincidence off. This is necessary since the BGO anticoincidence effect depends on the decay scheme and would otherwise shift the efficiency curve.

The point-like sources of  $^{137}\text{Cs}$  and  $^{60}\text{Co}$  were placed on the target ladder in the chamber in front of the detector, in the same geometry used for the data taking. They were fixed to a blank tantalum backing to include all passive material of the setup. Their quoted activity was known with 0.75–1.5% uncertainty and were used to obtain absolute detection efficiencies for  $\gamma$ -rays of 662, 1173, 1333 keV. The branching ratios for  $\gamma$ -rays [67] have been taken into account:  $(85.1 \pm 0.2)\%$  was used for the  $\gamma$ -emission of  $^{137}\text{Cs}$ .

For the two cobalt peaks, summing-out losses have been calculated, based on eq. (2.8) in section 2.6.1, where the angular correlation  $\rho^{\gamma\gamma}$  is 1.08. For the total efficiency, the sum of all events in the cobalt spectrum (background subtracted) divided by two has been used. The  $^{60}\text{Co}$  summing-out correction is found to be 2.8% for addback and 0.9% for singles mode. The latter number is based on the black segment data only, and a similar behavior is assumed for the other three segments.

When extending the efficiency curve to high energy, the known 1:1  $\gamma$ -ray cascades for the excited states at 6172 and 6792 keV [34] was used. The  $\gamma$ -rays from the decay of this  $1/2^+$  resonance are isotropic [34]. This assumption is later verified experimentally in the present work (section 3.2.1).

After correcting for summing-out (section 2.6.1), experimental primary to secondary ratios have been obtained from the on-resonance spectra with BGO off (table 2.10). The values are in agreement with the values from spectra simulated with GEANT4.

The fit resulted in the following curve for the addback mode, BGO off (fig. 2.12):

$$\begin{aligned} \log[\varepsilon_\gamma(E_\gamma)] &= -(2.969 \pm 0.001) & (2.6) \\ &\quad -(1.137 \pm 0.008) \cdot \log[E_\gamma/6.791 \text{ MeV}] \\ &\quad -(0.303 \pm 0.008) \cdot (\log[E_\gamma/6.791 \text{ MeV}])^2 \end{aligned}$$

and for singles mode:

$$\begin{aligned} \log[\varepsilon_\gamma(E_\gamma)] &= -(3.289 \pm 0.004) & (2.7) \\ &\quad -(1.387 \pm 0.033) \cdot \log[E_\gamma/6.791 \text{ MeV}] \\ &\quad -(0.384 \pm 0.035) \cdot (\log[E_\gamma/6.791 \text{ MeV}])^2 \end{aligned}$$

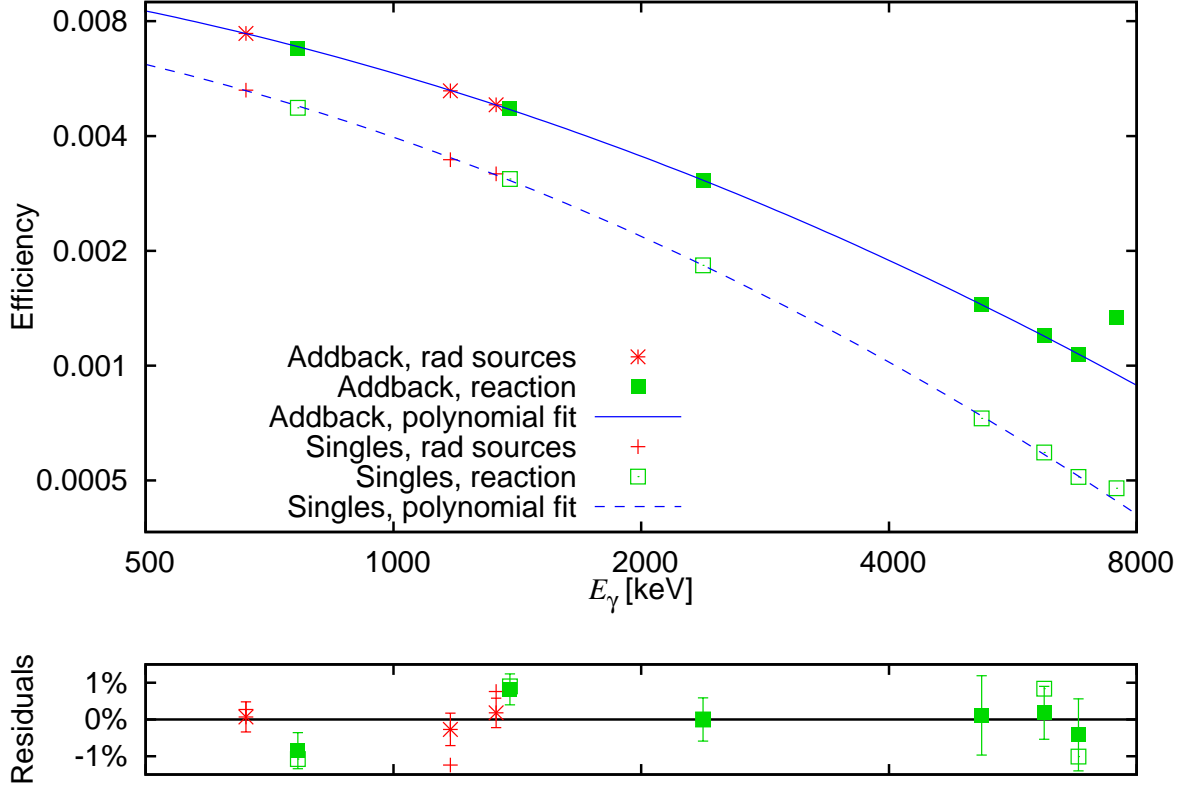


Figure 2.12: Upper panel:  $\gamma$ -ray detection efficiency for the detector at 9.5 cm distance from the target, as determined with radioactive sources and the two-line method at the 259 keV resonance. Solid (dashed) curve, efficiency for addback (singles) mode. Lower panel: Residuals. The data point at 7556 keV is not corrected for summing-in and was not included in the fit, therefore no residual is shown here. The pair of  $\gamma$ -rays at 5181 and 2375 keV was also not included in the fit but is plotted here as a check on the reliability of the curve.

The uncertainty on the offset, i.e. the absolute normalization at 6791 keV, is 1.8%, based on

- 1.1% stat. uncertainty in the 6.79 primary/secondary ratio,
- 1.1% uncertainty from the geometry (table 2.7),
- 0.7% from the source certificates obtained by combining 0.75% for  $^{60}\text{Co}$  source and 1.5% for  $^{137}\text{Cs}$ ,
- 0.4% from the difference between the summing-out corrections.

The efficiency curve in eq. 2.6, 2.7 and fig. 2.12 refers to a situation in which the effects of the BGO anticoincidence, the multiplexed ADC suppression and the summing-out effect have been removed. This means that the experimental counting rates must be corrected according to tables 2.7 and 2.13, depending on the nature of the peak under study, before these efficiency curves are used.

## 2.5 Effective energy

The typical distribution of counts observed in the  $\gamma$ -spectra for the primary's nonresonant peak (fig. 2.9 in section 2.3) spreads over an energy range which corresponds to the target thickness at that beam energy. Because of the energy loss of the protons, the reactions occur at different energies and have consequently a slightly different cross section. If one is willing to give only one value of cross section from the net area over the whole nonresonant part, this must be referred to only one representative value of energy, called effective energy. It is quite important to furnish a reliable value of energy because the cross section strongly depends on  $E$ , in the low energy regime. As an example, 1 keV uncertainty at  $E = 300$  keV results in 1.8% error on the cross section.

Here, the effective energy is calculated as the weighted mean of all possible energies, the weight being their relative contribution to the total cross section. In order to obtain an effective energy at the different run energies, two methods are compared here.

**Method A** considers the target scans (sect. 2.1.3) between the runs at the three energies. Instead of an analytical fit to the profiles, the numerical integral (trapezoidal method) of each interval between two scan points has been calculated. The beam energy at each scan point has then been weighted with a calculated cross section based on literature S-factor curves from LUNA 2005 [35], times the scan yield at this point (eq. 2.18). The results for the four most important transitions are summarized in table 2.11 (column A). The values differ due to the different behavior of the S-factor versus energy, that changes the weight of each energy.

**Method B** consisted in evaluating the centroid of the nonresonant part in the  $\gamma$ -spectra, using the same ROIs and background subtraction as in section 2.3. An average is calculated for the energy, weighted for the net counts in the corresponding channel. Recoil and Doppler effect are considered and the position of the resonant peak is checked for small shifts due to the energy calibration procedure. Straight-line subtraction causes negative values in some channels at the ROI edges, due to statistics: they are included in the average without correction because they balance the other positive contributions in the region.

The results for both Method A and B are compared in table 2.11: the adopted value is the average of the results from the two methods, with uncertainty half of their difference (a minimum 1 keV error is assumed). For the cross section ratio values, the average of 6.79 and GS energies is considered, with uncertainty the maximum between the two single errors and the difference between 6.79 and GS effective energies.

Run $E_p$	GS			6.79		
	A	B	adopted	A	B	adopted
359 keV	314.3	314.9	314.6±1.0	314.6	317.2	315.9±1.3
380 keV	332.8	334.3	333.6±1.0	331.6	333.6	332.6±1.0
399 keV	353.4	354.4	353.9±1.0	351.9	353.5	352.7±1.0

Run $E_p$	5.18			6.17		
	A	B	adopted	A	B	adopted
359 keV	308.4	312.8	310.6±2.2	309.7	311.2	310.4±1.0
380 keV	326.0	329.1	327.6±1.6	326.8	326.3	326.6±1.0
399 keV	348.4	353.3	350.9±2.5	348.9	353.2	351.0±2.1

Table 2.11: Comparison between effective energies obtained with method A and B, and the adopted value of effective energy for all four transitions.

## 2.6 True coincidence summing

The true coincidence summing effect is the loss or gain of events in a particular energy region of the  $\gamma$ -spectrum, due to the simultaneous (within the resolving time of the electronics) interaction of two or more photons in the detector that yield only one event with energy equal to the sum of the coincident events' energies. The effect increases for large solid angles, thus whenever detectors are placed close to the source of radiation.

### 2.6.1 Summing-out effect calculation

The summing-out corresponds to the events lost from a peak area of interest, due to coincidence between this fully absorbed photon and a full or partial absorption of a second simultaneous photon interacting in the detector. The calculation is based on the following formula [66], where  $\epsilon_1$  is the full-energy peak efficiency for the first  $\gamma$ -ray, and  $\epsilon_{2,\text{tot}}$  is the total efficiency for the second  $\gamma$ -ray to be detected.  $A$  is the time-corrected source activity or in-beam reaction rate,  $rate_1$  is the counting rate observed in the first peak,  $\rho^{\gamma\gamma}$  is the pairwise angular correlation at  $0^\circ$ :

$$\epsilon_1 = \frac{rate_1}{A} \frac{1}{1 - \epsilon_{2,\text{tot}} \rho^{\gamma\gamma}} = \frac{rate_1}{A} (1 + \text{summing-out correction}) \quad (2.8)$$

For the total efficiency at low  $\gamma$ -energies, the sum of all events in the spectrum (background subtracted) has been considered for the cobalt source, similarly to what has been done in section 2.2.3. Then it was extended to higher energies taking into account the tabulated [69] attenuation coefficients  $\mu(E)$  of photons in germanium. The total efficiency  $\epsilon_{\text{tot}}(E)$  is roughly proportional to  $1 - \exp[-\mu(E)x]$ , where  $x$  ( $\text{g}/\text{cm}^2$ ) is the length of the crystal times the density of germanium.

The pairwise correlation factors on the resonance have been obtained from the experimental results of [53], which are summarized in table 2.12. In [53], a TiN target was irradiated with protons at  $E_p = 278$  keV and two NaI detectors measured the  $\gamma$ -rays: one counting only the high-energy secondary photons, fixed at  $45^\circ$  with respect to the beam axis, and the other one at  $90^\circ$  or  $180^\circ$  with respect to the previous detector. The ratio  $I(180^\circ)/I(90^\circ)$  between the number of coincident  $\gamma$ -rays in the two detectors when positioned at angles 180 or 90 degrees apart, was obtained for the three cascades through the 6.79, 6.17, 5.18 excited states. Because the angular correlation function is symmetric around  $90^\circ$ , the ratios correspond to its maximum change. For the present experiment, the increase (or decrease) of coincidence at  $0^\circ$  with respect to the non-correlated case is needed. The  $\rho^{\gamma\gamma}$  on resonance for the present setup has been derived starting from those experimental values. The details of the calculation are given in appendix A, as well as an independent prediction based on the spin and parity of nuclear states involved, that matches the observation by [53].

Since no experimental data are available at energies off resonance, the pairwise angular correlations have been also calculated (appendix A) and are presented in table 2.12. On resonance the relative uncertainties from the experiment were considered, while for the off-resonance case, a relative error of 100% has been assumed, to be very conservative.

Transition	$\frac{I(180^\circ)}{I(90^\circ)}$ [53]	$\rho^{\gamma\gamma}$ on res	Calculated $\rho^{\gamma\gamma}$ off res
6.79	$1.20 \pm 0.03$	$1.13 \pm 0.03$	$0.92 \pm 0.08$
6.17	$1.165 \pm 0.03$	$1.11 \pm 0.03$	$0.98 \pm 0.02$
5.18	$1.01 \pm 0.03$	$1.00 \pm 0.03$	$1.00 \pm 0.03$

Table 2.12: Cascade  $\gamma$ -rays angular correlations on and off the  $E = 259$  keV resonance.

Summing-out corrections have been calculated for the in-beam lines on resonance (table 2.13) and off resonance. A conservative relative uncertainty of 20% is estimated for these corrections, based on the possible uncertainty of calculated angular correlations (10%) and total efficiencies ( $\approx 20\%$ ).

## 2.6.2 Summing-in effect for the ground state capture line

The summing-in refers to the artificially gained events in the peak area of interest, caused by the coincidences between two or more simultaneous photons fully absorbed in the detector, the energies of which sum up to the one of interest. For the present experiment, it is very important to study the summing-in effect because it affects strongly the measurement of the cross section corresponding to the capture to the ground state in  $^{15}\text{O}$ . The summing-in effect  $SumIn$  is defined as the number of “false” events  $GS_{\text{coinc}}$ , due to the coincidences of cascade  $\gamma$ -rays, divided by the “true” events  $GS$ , the total events  $GS_{\text{tot}}$

Line	$\rho^{\gamma\gamma}$	$\mu$ [cm <sup>2</sup> /g]	Calc. summing out correction	
			adddback	singles
<sup>60</sup> Co	1.08	0.051	(2.8±0.6)%	(0.9±0.2)%
6.79 primary	1.13	0.031	(1.8±0.4)%	(0.5±0.1)%
6.79 secondary		0.064	(3.7±0.7)%	(1.1±0.2)%
6.17 primary	1.11	0.031	(1.8±0.4)%	(0.5±0.1)%
6.17 secondary		0.051	(2.9±0.6)%	(0.9±0.2)%
5.18 primary	1.00	0.032	(1.6±0.3)%	(0.5±0.1)%
5.18 secondary		0.038	(1.9±0.4)%	(0.6±0.1)%

Table 2.13: Angular correlations, attenuation coefficients  $\mu$  of partner line [69], and calculated summing-out corrections for <sup>60</sup>Co source and in-beam on-resonance cascade photons both for addback and singles mode.

being the sum of the two:

$$SumIn = \frac{GS_{coinc}}{GS} = \frac{GS_{tot} - GS}{GS}. \quad (2.9)$$

Two approaches have been used to study the summing-in:

**exp** obtain information directly from the experimental counts for capture to <sup>15</sup>O levels at 6.79, 6.17, 5.24, 5.18;

**calc** rely on a formula [66] that depends on literature branching ratios and calculated pairwise angular correlations (table 2.12 in previous section 2.6.1).

Both methods depend on the detection efficiency (sec. 2.4, eqns. (2.6) and (2.7)) and on the branching ratio of the capture to the ground state.

Equation (2.10) shows the experimental approach:  $C_{GS}$  and  $C_i$  are the observed counts in the peaks of the ground state transition and of the other four primary (or secondary)  $\gamma$ -rays through  $i = 6.79, 6.17, 5.24, 5.18$  states. The  $C_i$  are already corrected for DAQ issues and summing-out,  $C_{GS}$  just for DAQ corrections.  $\varepsilon_{GS}$  and  $\varepsilon_i$  are the experimental efficiencies and  $BR_{GS}$  is the ground state branching ratio,

$$SumIn_{exp} = \frac{GS_{tot} - GS}{GS} = \frac{\frac{C_{GS}}{\varepsilon_{GS}} - \left( \sum_{i=E_x} \frac{C_i}{\varepsilon_i} \right) \frac{BR_{GS}}{1 - BR_{GS}}}{\left( \sum_{i=E_x} \frac{C_i}{\varepsilon_i} \right) \frac{BR_{GS}}{1 - BR_{GS}}} \quad (2.10)$$

The sum of branching ratios for all transitions except the ground state  $\sum_{i=E_x} BR_i$  is substituted by  $1 - BR_{GS}$ .

A similar formula (2.11) gives the calculated summing correction at a certain energy, by considering: experimental efficiencies for ground state  $\varepsilon_{GS}$ , and for four couples of

primary and secondary  $\gamma$ -rays  $\varepsilon_{i,\text{pri}}$ ,  $\varepsilon_{i,\text{sec}}$ ; literature branching ratios [35]  $BR_i$ ,  $BR_{\text{GS}}$ ; pairwise correlation factors  $\rho_i^{\gamma\gamma}$  (table 2.12 in previous section 2.6.1):

$$SumIn_{\text{calc}} = \frac{GS_{\text{coinc}}}{GS} = \frac{\sum_{i=E_x} \varepsilon_{i,\text{pri}}\varepsilon_{i,\text{sec}}BR_i\rho_i^{\gamma\gamma}}{\varepsilon_{\text{GS}}BR_{\text{GS}}}. \quad (2.11)$$

All the efficiencies and literature branching ratios [35] have been derived considering the effective energies obtained in 2.5 for each set of runs acquired with same nominal beam energy.

### 2.6.2.1 Summing-in on resonance

Experimental and calculated summing-in effect on resonance were compared, considering the  $BR_{\text{GS}}$  as a free parameter (table 2.14 and fig. 2.13). Then it was possible to find the value of  $BR_{\text{GS}}$  that yields

$$SumIn_{\text{exp}}(BR_{\text{GS}}) = SumIn_{\text{calc}}(BR_{\text{GS}}) \quad (2.12)$$

The uncertainty has been evaluated for both formulae (2.10) and (2.11): the main uncertainty comes from the statistical errors of counts in the ground state peak for the **exp** approach. The final error on the ground state branching ratio is defined as the range of values leading to equation 2.12 within their  $1\sigma$  uncertainties, i.e. the areas defined by the intersecting uncertainty curves in the middle of the two plots in figure 2.13.

Spectrum	Method	1.70% [37]	1.60% [35]	1.53%	1.51%
Addback mode	experiment	(28±2)%	(36±3)%	(42±3)%	(45±3)%
	calculated	(38±1)%	(40±1)%	(42±1)%	(43±1)%
	GEANT4		(38±5)%		
Singles mode	experiment	-(3±2)%	(2±2)%	(6±2)%	(7±2)%
	calculated	(6.6±0.2)%	(7.0±0.2)%	(7.3±0.2)%	(7.4±0.2)%
	GEANT4		(5±6)%		

Table 2.14: Summing-in effect for the ground state capture peak at resonance energy for different values of the ground state branching ratio.

Equation 2.12 is satisfied for the addback mode when assuming a  $(1.53\pm 0.07)\%$  branching ratio for capture to the ground state. The value obtained independently for singles mode is  $(1.51\pm 0.04)\%$ . The present  $BR_{\text{GS}}$  has better precision than the  $(1.6\pm 0.1)\%$  previously reported by LUNA [35]. The result is only in fair agreement with the previously reported  $(1.70\pm 0.07)\%$  branching by TUNL [37].

The final summing correction and corresponding uncertainty are calculated considering the value for ground state branching just obtained and eq. (2.11) to give the values quoted in table 2.16.



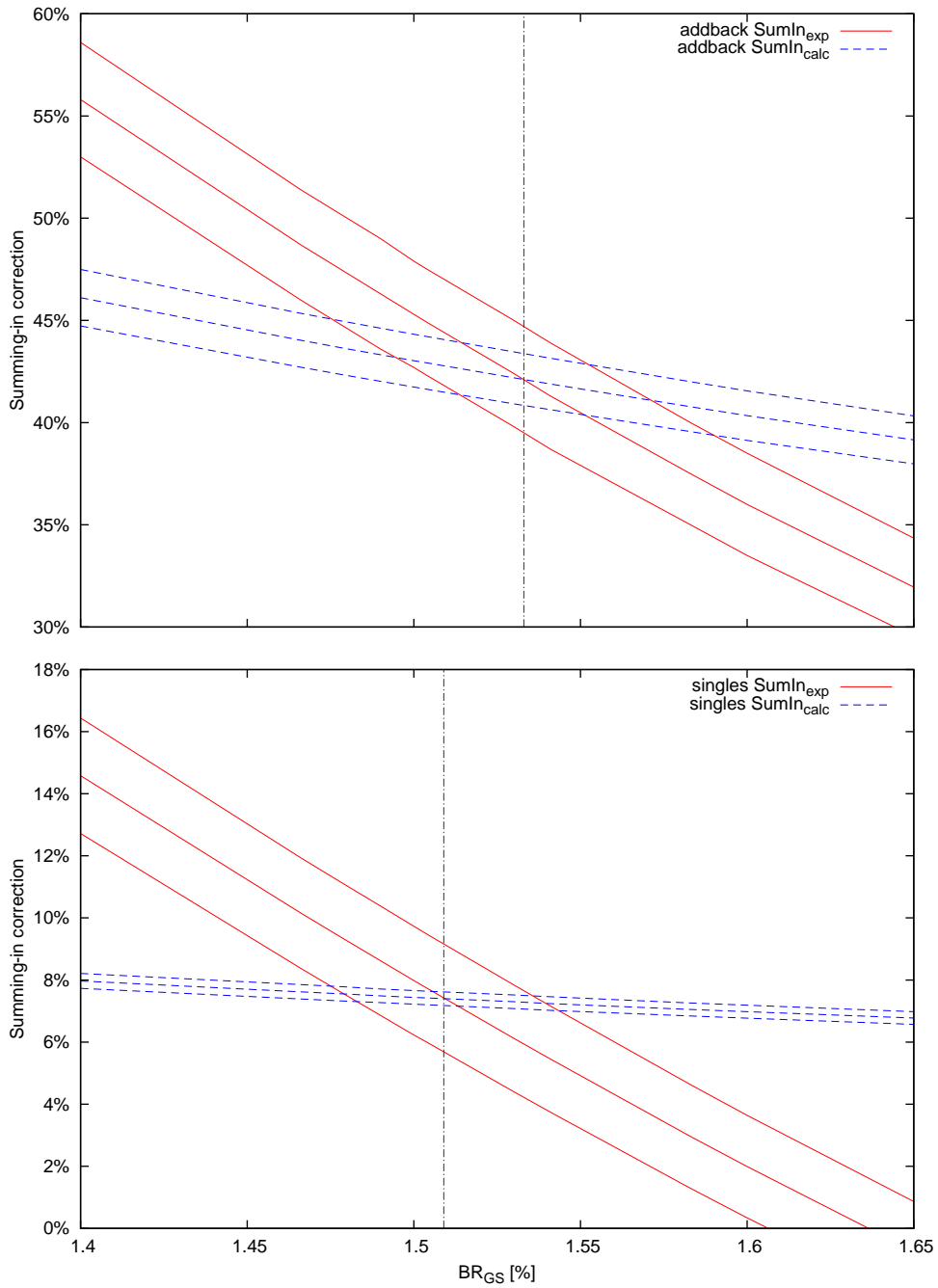


Figure 2.13: Summing-in corrections on 259 keV resonance, in close geometry, versus assumed branching ratio for Ground State transition  $BR_{GS}$ , both for addback (top panel) and singles mode (bottom panel), calculated (dashed, blue) and experimental (solid, red). Thinner lines delimit the  $1\sigma$  level regions.

### 2.6.2.2 Summing-in at energies off resonance

The same procedure has been applied also to off-resonance runs to obtain a ground state branching ratio (and corresponding summing-in effect) for each bombarding energy (table 2.15). Some difficulties arise due to the smaller intensity of the reaction lines relative to the laboratory background, thus requiring large subtractions in the peak areas, especially for the primary emission through the 6.17 MeV state. Good agreement was observed between the summing-in and the GEANT4 simulation (table 2.14 and 2.15).

Spectrum		359 keV	380 keV	399 keV
Addback	obtained	(30±5)%	(21±3)%	(19±2)%
	GEANT4	(30±4)%	(27±4)%	(17±3)%
Singles	obtained	(4.3±0.9)%	(3.4±0.6)%	(3.2±0.5)%
	GEANT4	(9±6)%	(9±5)%	(1±5)%
LUNA04 [36, 35]	calculated	151%	129%	140%

Table 2.15: Obtained and simulated summing-in effect for the ground state capture peak, for different beam energies. The effect obtained with the previous LUNA experiment [36, 35] is shown for comparison.

$E$ [keV]	mode	SumIn [%]	$BR_{GS}$ [%]
259	addback	42±2	1.53±0.07
	singles	7.4±0.3	1.51±0.04
315	addback	30±5	2.0± 0.3
	singles	4.3±0.9	2.4± 0.4
333	addback	21±3	2.9± 0.3
	singles	3.4±0.6	3.1± 0.4
353	addback	19±2	3.2± 0.2
	singles	3.2±0.5	3.3± 0.4

Table 2.16: Summing-in correction and ground state branching ratio for both on and off resonance.

## 2.7 Relative cross section data for capture to the ground state

In this section, the ratios of cross sections for capture to the ground state and 6.79 state are presented. The 6.79 transition is chosen because its contribution to the cross section is well known in literature, so it makes sense to normalize the present analysis to it.

There are some advantages in measuring a ratio between two cross sections instead of furnishing an absolute value: many parameters are not needed, so their uncertainties do not affect the results. In the present case, the absolute knowledge of beam current, characteristics of the targets (stoichiometry, nitrogen distribution) and absolute detection efficiency do not enter the analysis. However, a precise ratio of  $\gamma$ -efficiencies is needed to normalize the rates at different energies. The experimental counts of transitions through the 6.79 and to the ground state are also necessary.

Based on the data already corrected for summing-in/out and for all the electronics issues (table 2.9) and the efficiency curve (fig. 2.12, eqns. 2.6, 2.7), the experimental ratio between the cross sections for capture to the ground state has been calculated (table 2.17).

Run	$E$ [keV]	$\sigma_{\text{GS}}/\sigma_{679}$ [ $10^{-2}$ ]	Stat	Syst	SumIn
359 keV addback	315.3 $\pm$ 1.3	5.24 $\pm$ 0.62	11%	5.4%	30%
359 keV singles			15%	2.7%	4.3%
380 keV addback	333.1 $\pm$ 1.0	5.33 $\pm$ 0.33	4.8%	3.9%	21%
380 keV singles			11%	2.5%	3.4%
399 keV addback	353.3 $\pm$ 1.0	5.20 $\pm$ 0.26	3.5%	3.5%	19%
399 keV singles			8.0%	2.3%	3.2%

Table 2.17: Experimental ratio of the cross section for capture to the ground state in  $^{15}\text{O}$  relative to the cross section for capture to the 6792 keV state. They are associated to the average of the effective energies of the two transitions. The contributions to the error given by statistical and systematical uncertainties are shown. In the last column, the applied summing-in correction.

The uncertainties (tables 2.19, 2.18) have been divided into:

**statistical** coming from the counts statistics (mainly the ground state line) and entering directly in the ratio calculation;

**systematical** errors associated to the corrections for summing-out and -in, electronics issues, detection efficiency curve and adopted effective energy.

For clarity, the sources for uncertainty of the summing-in correction and their impact on the final ratio are summarized in table 2.20.

Statistics	359 keV		380 keV		399 keV	
	addback	singles	addback	singles	addback	singles
ground state, NonRes	9.5%	14%	4.5%	11%	3.3%	7.8%
6.79 secondary	0.6%	0.9%	0.6%	0.8%	0.6%	0.8%
6.79 primary, $\frac{NonRes}{NonRes+Res}$	4.6%	6.2%	1.6%	1.6%	1.1%	1.2%
Final statistical uncert.	11%	15%	4.8%	11%	3.5%	8.0%

Table 2.18: Summary of statistical uncertainties for the cross section ratios.

Systematics	addback	singles
BGO/ADC cascade	1.2%	0.7%
BGO/ADC single transition	0.3%	0%
Summing-out	0.7%	0.2%
Summing-in (incl. ang. corr.)	2.3%–4.7%	0.5%–0.9%
Detection efficiency ratio	0.3%	0.8%
Adopted effective energy	2.0%–2.4%	
Final systematical uncert.	3.5%–5.5%	2.7%–3.0%

Table 2.19: Systematical uncertainties in the cross section ratios.

### 2.7.1 S-factors for capture to the ground state

The ratios in table 2.17 are subsequently normalized with the weighted average of the S-factor results for the 6792 keV transition given in Refs. [38, 37, 35]. The  $S_{GS}(E)$  for the three runs are shown in table 2.21 and plotted in fig. 2.14 of section 2.9). The total error is given by the sum in quadrature of the statistical uncertainty of the ratios  $\sigma_{GS}/\sigma_{679}$  and the 6% uncertainty on the 6.79 S-factor, that includes the experimental systematic errors of the data sets used to obtain it. Based on these values, new R-matrix fits have been performed, that are presented in chapter 4.

Syst. SumIn	359 keV		380 keV		399 keV	
	AB	S	AB	S	AB	S
Branching ratios (liter. + GS)	4.3%	0.9%	2.4%	0.6%	1.8%	0.5%
Detection efficiency	0.5%	0.1%	0.4%	0.1%	0.4%	0.1%
Angular correlation (100%)	1.7%	0.3%	1.4%	0.3%	1.4%	0.3%
Final SumIn uncertainty	4.7%	0.9%	2.8%	0.7%	2.3%	0.5%

Table 2.20: Absolute summing-in uncertainties and (last row) relative to the cross section ratio, for addback (AB) and singles (S) mode.

$E$	$S_{GS}(E)$	$\Delta S_{GS}$
314.6	0.0775	0.0094
333.6	0.0677	0.0053
353.9	0.0611	0.0043

Table 2.21: S-factors for capture to the ground state, obtained from the ratios of cross sections.

## 2.8 Branching ratios for the decay of the 259 keV resonance

In order to determine the branching ratios for the decay of the 259 keV  $\frac{1}{2}^+$  resonance ( $E_x = 7556$  keV in  $^{15}\text{O}$ ), the Clover detector was moved to far geometry, with its front face at 19.5 cm distance from the target position, again at an angle of  $55^\circ$  with respect to the beam direction. For the branching ratio analysis, both addback and singles mode data have been analyzed and were found to be in agreement in all cases. Only the singles mode data will be discussed here, because of their lower summing-in correction.

The detection efficiency was again established as described above (sec. 2.4), with an analogous quality of the efficiency curve (fig. 2.12). It should be stressed that this determination of the efficiency curve does not depend on the branching ratios, just on the assumption of 1:1 cascade ratios without feeding or intermediate decay corrections for the two transitions through the states at 6172 and 6792 keV, and on the assumption of isotropy for the angular distribution of emitted photons [34, 38].

For the determination of the decay branchings of the 259 keV resonance, only the secondary  $\gamma$ -rays at 5181, 5241, 6172, and 6792 keV and the ground state primary  $\gamma$ -ray at 7556 keV were used (fig. 2.11, bottom panel). Therefore only the relative  $\gamma$ -efficiency in the limited energy range 5181-7556 keV is needed. Owing to the good quality of the  $\gamma$ -efficiency curve, over this limited energy range the efficiencies relative to the 6172 keV normalization point are known on the level of  $\pm 0.5\%$ , enabling a precise determination of the branching ratios.

For the major transitions through the excited states at 5182, 6172, and 6792 keV, the present branching ratios (tab. 2.22) are in excellent agreement with the literature [34, 37, 35]. However, some minor discrepancies arise when it comes to the minor transitions.

The case with the greatest astrophysical importance is the ground state transition. It is now well-known [37, 35] that the previously accepted value of  $(3.5 \pm 0.5)\%$  [70, 71, 34] was much too high. The present value of  $(1.48 \pm 0.04)\%$  is again slightly lower than previous work [37, 35] but still in fair agreement. The value is in agreement with the value  $(1.51 \pm 0.04)\%$  of table 2.16 in section 2.6.2, which has been obtained in closer geometry, with the Clover detector front end at 9.5 cm distance from the target, resulting in 7.4% summing-in correction. In contrast, the present branching has been obtained at 19.5 cm distance with just 2.0% summing-in correction, much less than in previous works [37, 35].

		Branching [%]			
		Ajzenberg- Selove [34]	TUNL [37]	LUNA [35]	LUNA, present work
7556→	0	3.5±0.5	1.70±0.07	1.6±0.1	1.48±0.04
→	5181	15.8±0.6	17.3±0.2	17.1±0.2	17.3±0.2
→	5241			0.6±0.3	0.15±0.03
→	6172	57.5±0.4	58.3±0.5	57.8±0.3	58.3±0.4
→	6792	23.2±0.6	22.7±0.3	22.9±0.3	22.6±0.3
SumIn correction			12%	17%	2%

Table 2.22: Branching ratios for the decay of the 259 keV resonance ( $E_x = 7556$  keV in  $^{15}\text{O}$ ) obtained with the Clover detector in singles mode, at 19.5 cm distance from the target (far geometry). The numbers are compared with previous data [34, 37, 35].

## 2.9 Absolute analysis of GS, 5.18, 6.17, 6.79 cross sections

The cross sections for capture to the excited states at 5181, 6172, and 6792 keV and to the ground state of  $^{15}\text{O}$  have been derived at the three studied proton energies with an “absolute” method. It is based on target profiles and stoichiometry (sec. 2.1.3), beam current (sec. 2.1.2), detection efficiency and all DAQ corrections (sections 2.4, 2.2) and the net counts from the spectra (sec. 2.3). The behind-the-scenes ingredient is the strength of the well-studied  $E_p = 278$  keV resonance in the  $^{14}\text{N}(p,\gamma)^{15}\text{O}$  reaction. The value  $\omega\gamma_{278} = 13.1\pm 0.6$  meV [31] is used to determine the initial stoichiometry from the yield at the plateau of the target scan.

Only the addback mode branch has been considered due to the higher signal to noise ratio in the  $\gamma$ -spectra with respect to singles mode. Besides, the agreement between the two branches of DAQ was already tested for the capture to the 6792 keV and ground state in section 2.7, proving that detection efficiency and summing correction are well understood. The contribution by on-resonance events to the net counts of the secondary  $\gamma$ -ray was subtracted taking into account the corresponding primary resonant and nonresonant parts (section 2.3, fig. 2.9, tab. 2.9). The angular distribution was assumed to exhibit negligible contributions from all Legendre polynomials except for zero and second order, which cancel out at the present detection angle of  $55^\circ$ .

### 2.9.1 The absolute cross section

The experimental yield is given by  $N_\gamma$  the number of reactions occurring at the target position divided by the number of ions hitting the target during the same time  $N_p$ . The former is the  $Counts_{\text{live}}$  obtained from an integration procedure of the peak area in the

$\gamma$ -ray spectra, divided by the detection efficiency  $\varepsilon(E_\gamma)$  at the energy of the peak. The number  $N_p$  is the accumulated beam *Charge* (in C) divided by the elementary charge  $1.602 \cdot 10^{-19}$  (C/e) and corrected for dead time (0.3%) to obtain only the ions hitting the target during live acquisition:

$$Y_{\text{exper}} = \frac{N_\gamma}{N_p} = \frac{\text{Counts}_{\text{live}}}{\varepsilon(E_\gamma)\text{Charge}_{\text{live}}} \quad (2.13)$$

The cross section  $\sigma(E)$  of a reaction between charged particles is commonly expressed [1] as follows:

$$\sigma(E) = \frac{S(E)}{E} \exp\left(-31.29zZ\sqrt{\frac{\mu}{E}}\right) = S(E)f(E; Z, z, \mu) \quad (2.14)$$

where  $E$  is the proton energy (in keV) in the centre of mass frame,  $S(E)$  is the astrophysical factor (in keV barn),  $z$  and  $Z$  the charge of projectile and target nuclei,  $\mu$  the reduced mass in a.m.u. The formula can be rewritten as the product of two quantities: the astrophysical factor  $S(E)$  that can not be directly calculated and the rest of the formula  $f(E; Z, z, \mu)$  which depends only on the interaction energy and the charge and mass of the nuclei involved.

On the other hand, the expected yield is calculated from an integral over the whole target thickness from  $x = 0$  to  $x = x_{\text{end}}$  of the cross section  $\sigma(E)$  (barn) times an infinitesimal slice of target containing  $n(x)dx$  nuclei per square centimeter. Including eq. (2.14) yields:

$$Y_{\text{calc}} = \int_0^{x_{\text{end}}} S(E(x))f(E(x); Z, z, \mu)n(x)dx \quad (2.15)$$

where the energy  $E(x)$  corresponds to the proton energy (in the laboratory)  $E_p(x)$  at different depths in the target  $x$ , which in turn is given by the beam energy  $E_{p,\text{beam}}$  minus the energy loss in the target up to that point  $x$ :

$$E_p(x) = E_{p,\text{beam}} - \int_0^x \frac{dE}{n dt}(E_p(t))n(t)dt \quad (2.16)$$

$\frac{dE}{n dt}(E_p(t))$  is calculated numerically with SRIM [60] considering small steps of  $x$ .  $n(t)dt$  is obtained from the target scans and the initial stoichiometry from the literature resonance strength  $\omega\gamma_{278}$ . An interpolation must be performed between different scans to estimate the profile condition during the run considered at a particular beam energy  $E_{p,\text{beam}}$ .

The applied method consists of evaluating numerically the  $Y_{\text{calc}}$  in eq. (2.15), assuming a certain behavior for the astrophysical factor  $S(E)$  (from literature) and compare it to the yield  $Y_{\text{exper}}$  of eq. (2.13). The ratio is usually in the range 0.9 - 1.1, meaning that the present measurement does not differ much from the value in literature. The new S-factor is then given by:

$$S_{\text{exper}}(E_{\text{eff}}) = \frac{Y_{\text{exper}}}{Y_{\text{calc}}} S(E_{\text{eff}}), \quad (2.17)$$

with  $S(E_{\text{eff}})$  being the assumed astrophysical factor at the effective energy  $E_{\text{eff}}$ , as obtained in section 2.5, where the method A values are calculated as:

$$E_{\text{eff}} = \frac{\int_0^{x_{\text{end}}} S(E(x))f(E(x); Z, z, \mu)\mathbf{E}(\mathbf{x})n(x)dx}{\int_0^{x_{\text{end}}} S(E(x))f(E(x); Z, z, \mu)n(x)dx} \quad (2.18)$$

and are then averaged with the values from method B, to give the adopted ones (tab. 2.11).

One should notice that this procedure to obtain the S-factors is dependent on the choice of  $S(E)$ , because its slope influences  $Y_{\text{calc}}$  and eventually different values of  $S_{\text{exper}}(E_{\text{eff}})$  are obtained. For the present S-factor determination, the astrophysical S-factor was assumed to vary over the target thickness as given by the previous LUNA R-matrix curve [35]. The present analysis was repeated assuming different literature trends of  $S(E)$  as well as a flat slope. The maximum difference of 1-9% in the  $S_{\text{exper}}(E_{\text{eff}})$ , depending on the transition and beam energy, has been assumed as an estimation of the error (tab. 2.23).

## 2.9.2 Results and discussion

The presently obtained S-factors for all the transitions are summarized in table 2.24 and compared with literature fits and data in figures from 2.14 to 2.17. A few high-energy data from [38] reach the energy range plotted, but are not shown for simplicity. The error bars of all data points include the statistical uncertainties plus the error due to summing correction, if not otherwise written. The remaining systematics are common to the points of each data set and would affect them all in the same direction.

All the other sources of error are summarized in table 2.23. In addition to the errors already discussed in section 2.7 about the relative method to obtain the cross section, further systematics enter the calculations. A major role is played by the uncertainties on the target stoichiometry and profile and by the assumption on the S-factor slope.

The present results for capture to the ground state in fig. 2.14, obtained with the absolute and with the relative method (sec. 2.7.1, tab. 2.21) are in good agreement with each other and have the smallest uncertainty. The agreement with previous LUNA 2005 [36, 35] and TUNL [37] is good only for the two lower beam energies. The  $E_p = 399$  keV data differs by more than its  $3\sigma$  uncertainty from the others and seems to point to higher cross section, better connecting with the high-energy data from [38]. This trend is also confirmed by the LUNA 2005 fit itself, that did not include the present data set.

The present curve LUNA 2008 (discussed in sec. 4.2) lies higher than the others, because only the three relative S-factor data have been used together with the high-energy (summing corrected) data set from [38]. The literature fits are from LUNA 2005 [36, 35], TUNL [37] and the Solar Fusion 2 workshop (SF2) that reviewed the existing data and performed new fits for this reaction [31]. The LUNA 2005 and SF2 curves do not seem to represent the trend suggested by the data that they are supposed to fit. Only



Description	Amount
Summing-in, ground state line	3-5%
Escape-suppression efficiency	1.2%
Slope of $\gamma$ -efficiency curve	0.8%
Summing-out	0.6%
Target, original stoichiometry	6%
Target, profile change	5%
Assumption on S-factor slope	1-9%
Beam current reproducibility	2%
Normalization of $\gamma$ -efficiency	1.8%
Total, addback mode	9-12%

Table 2.23: Systematic uncertainties affecting absolute cross sections (sec. 2.9). The summing corrections are given for the addback mode only; for the singles mode, they are negligible when compared with the other uncertainties.

the TUNL fit goes nicely through its data set and lies lower than the other curves, which is the reason for the discrepancy in the extrapolated  $S_{\text{GS}}(0)$  mentioned in section 1.4.

As to the capture to the 6792 keV excited state in figure 2.15, all data sets and fits are in very good agreement with each other within  $\approx 5\%$ . That justifies its use as a reference cross section. The present data have a competitive small uncertainty and are more in favor of the LUNA 2005 and SF2 fits.

For the other two minor transitions through the 6.17 and 5.18 levels (fig. 2.17 and 2.16), the present results are in very good agreement with the literature data points. In the 6.17 transition, all the data favor the SF2 curve and agree in indicating that the fit must be much steeper than suggested by LUNA 2005. Notice that the extrapolation towards lower energies of this transition too has a large uncertainty and after the capture to the ground state has the largest impact on the total extrapolated S-factor.

Capture to ground state				Capture to 6792 keV state			
$E$	$S_{\text{GS}}$	$\Delta_{\text{stat}}$	$\Delta_{\text{syst}}$	$E$	$S_{6792}$	$\Delta_{\text{stat}}$	$\Delta_{\text{syst}}$
$314.6 \pm 1.0$	0.074	11%	12%	$315.9 \pm 1.3$	1.495	5.0%	9%
$333.6 \pm 1.0$	0.061	5%	11%	$332.6 \pm 1.0$	1.245	3.0%	9%
$353.9 \pm 1.0$	0.061	4%	10%	$352.7 \pm 1.0$	1.157	1.7%	9%
Capture to 5181 keV state				Capture to 6172 keV state			
$E$	$S_{5181}$	$\Delta_{\text{stat}}$	$\Delta_{\text{syst}}$	$E$	$S_{6172}$	$\Delta_{\text{stat}}$	$\Delta_{\text{syst}}$
$310.6 \pm 2.2$	0.370	16%	11%	$310.5 \pm 1.0$	1.072	8%	12%
$327.6 \pm 1.6$	0.218	12%	12%	$326.6 \pm 1.0$	0.406	18%	12%
$350.9 \pm 2.5$	0.128	13%	10%	$351.1 \pm 2.2$	0.220	15%	10%

Table 2.24: S-factor results for capture to the ground state and to the excited states at 5181, 6172, and 6792 keV. The effective energy  $E$  is given in keV, the S-factor  $S$  in keV b , and the relative uncertainties in percent.

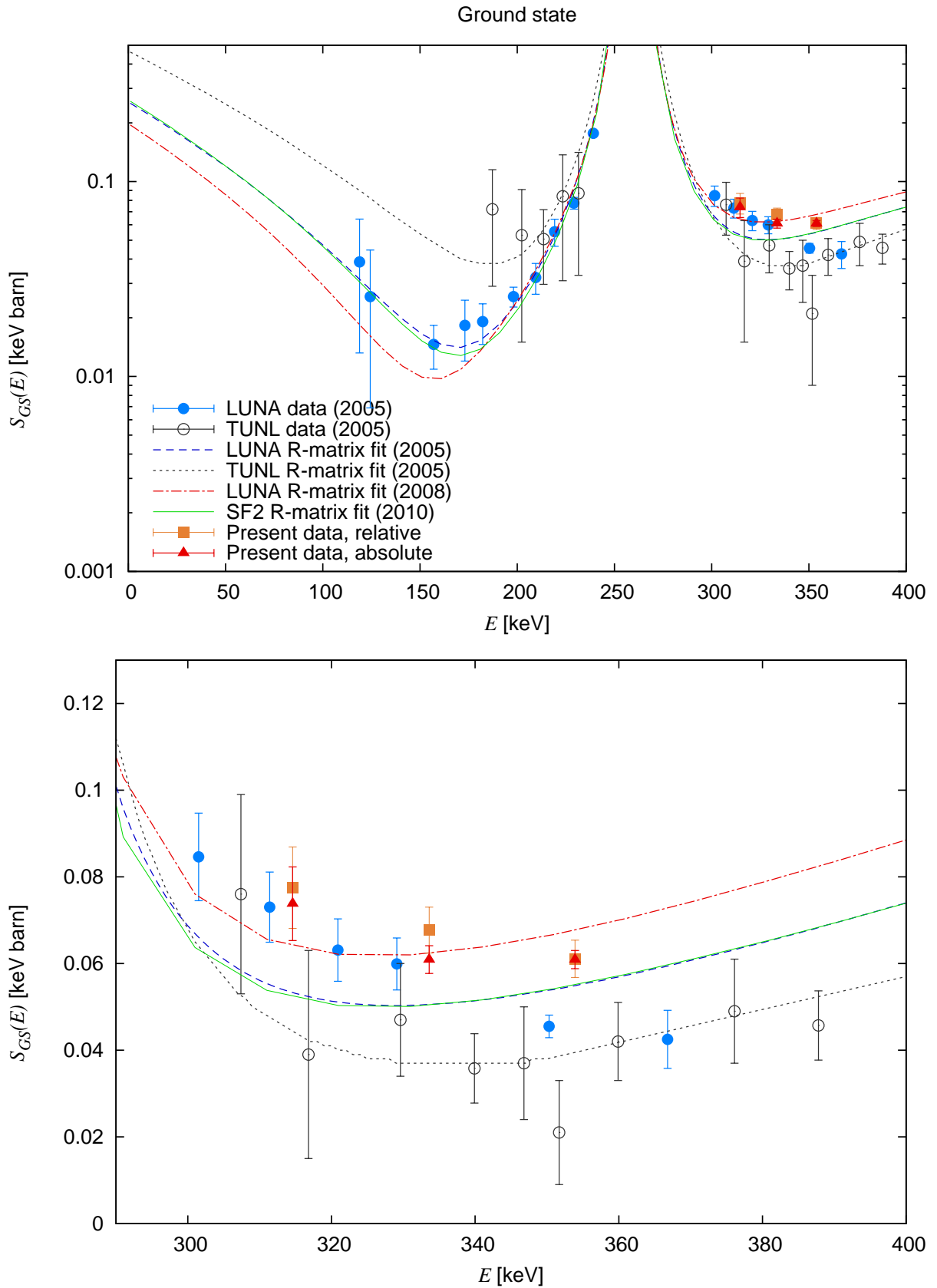


Figure 2.14: S-factor for capture to the ground state in  $^{15}\text{O}$ . The orange squares represent the present relative data, rescaled with the averaged  $S_{6.79}(E)$  as described in the section 2.7.1. The red dot-dashed curve [72] is the present fit obtained from the relative data (sec. 4.3). Error bars reflect the statistical uncertainty (except for the relative data, for which systematics are also included). A zoomed-in plot is given at the bottom.

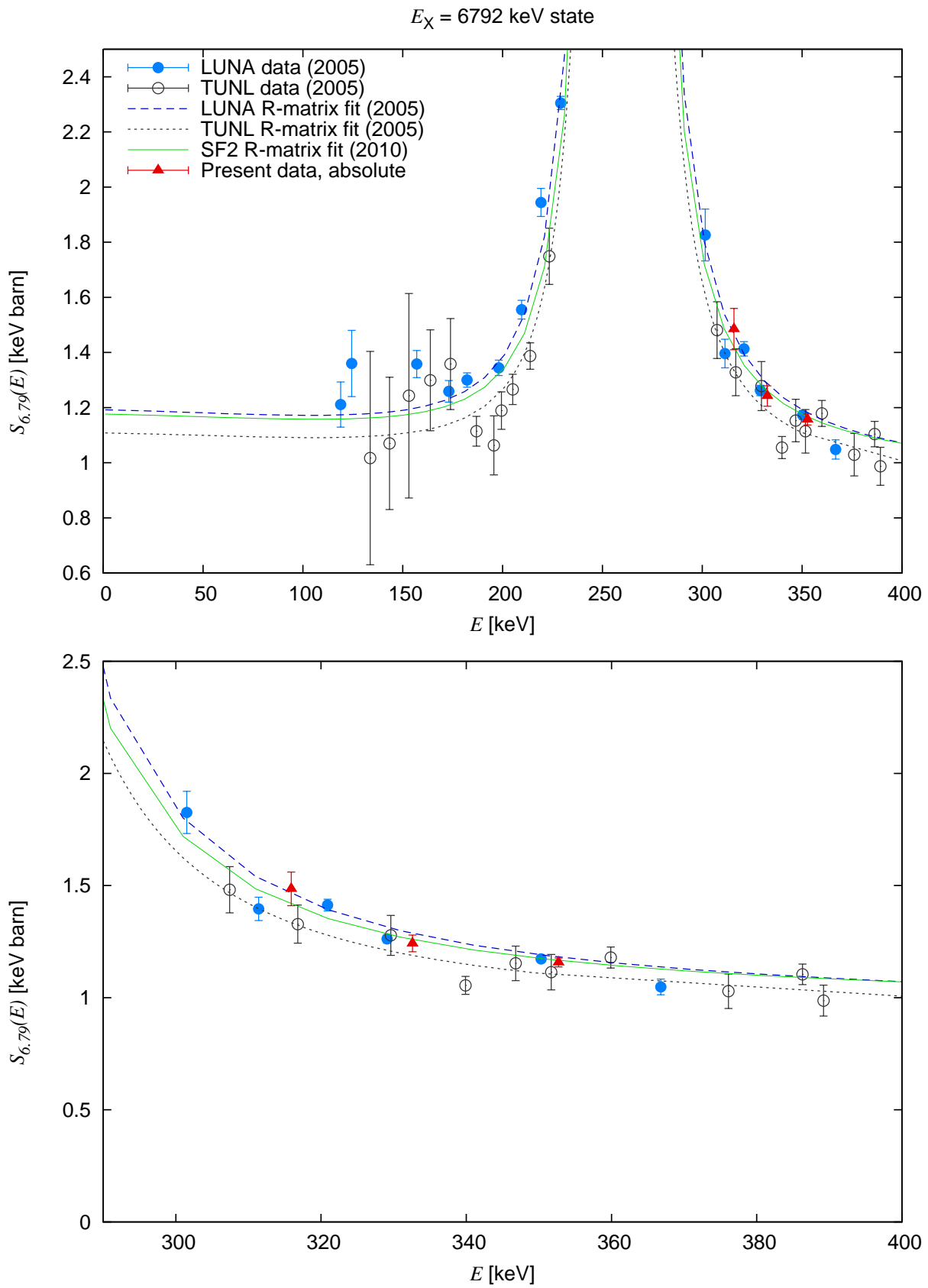


Figure 2.15: S-factor for capture to the excited states at 6792 keV in  $^{15}\text{O}$ . Data and fits as in the previous figure.

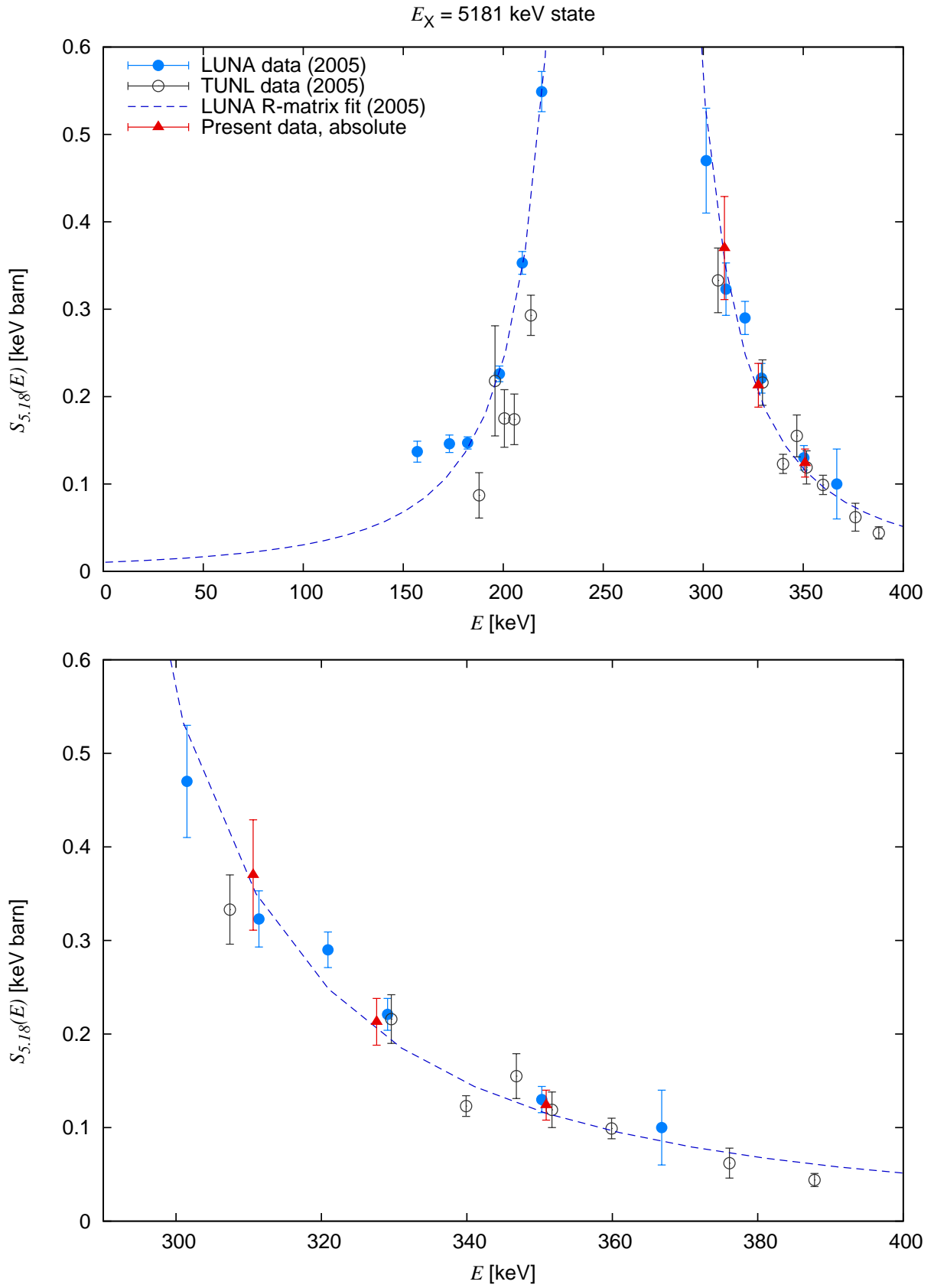


Figure 2.16: S-factor for capture to the excited states at 5181 keV in  $^{15}\text{O}$ . Data and fits as in the previous figure. No R-matrix fits are given in Refs. [37].

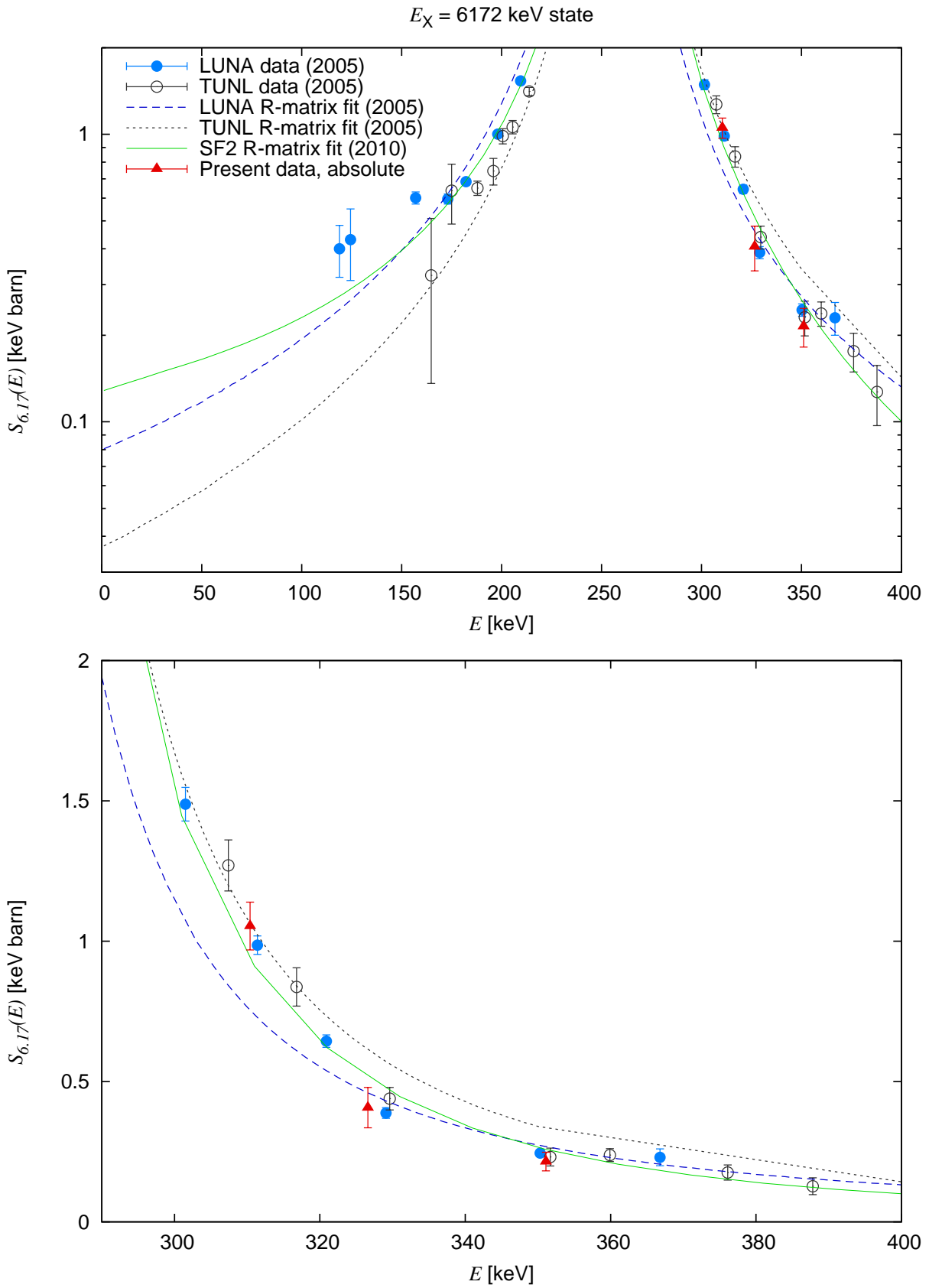


Figure 2.17: S-factor for capture to the excited states at 6172 keV in  $^{15}\text{O}$ . Data and fits as in the previous figure.

# Chapter 3

## High-energy resonances in $^{14}\text{N}(\text{p},\gamma)^{15}\text{O}$ and $^{15}\text{N}(\text{p},\alpha\gamma)^{12}\text{C}$ studied in Dresden.

The aim of this second experiment was to re-investigate the “high-energy region”, including the resonance at  $E_p = 1.058$  MeV and a few off resonance energies, up to  $E_p = 2$  MeV. The experiment was performed in the ion beam physics department of the Helmholtz-Zentrum Dresden–Rossendorf<sup>1</sup> (HZDR). A Tandem accelerator provided the proton beam, solid TiN sputtered targets were used and the target chamber was surrounded by four HPGe detectors at different angles and distances. The reaction  $^{14}\text{N}(\text{p},\gamma)^{15}\text{O}$  has been investigated at the  $E_p = 1.058$  MeV resonance (i.e. the excited state  $E_x = 8.284$  MeV of  $^{15}\text{O}$ , see fig. 1.4), and at a few energies off resonance between 0.6 and 2.0 MeV. The strength of the  $E_p = 1.058$  MeV resonance has been obtained relative to the well known resonance at  $E_p = 278$  keV, after checking the angular distribution. Newly calculated branching ratios are also provided.

The presence in the targets of the other stable nitrogen isotope  $^{15}\text{N}$  with known abundance allowed to monitor the targets’ degradation versus irradiation. Moreover, the two resonances at  $E_p = 430$  and  $897$  keV of the  $^{15}\text{N}(\text{p},\alpha\gamma)^{12}\text{C}$  reaction were strong enough to be studied, despite the very low abundance of the isotope  $^{15}\text{N}$ . Their angular distribution was checked and the resonance strengths were obtained once again relative to the  $E_p = 278$  keV resonance in  $^{14}\text{N}(\text{p},\gamma)^{15}\text{O}$ .

### 3.1 Setup

The proton beam from the high-current Tandetron accelerator in HZDR impinged onto solid TiN sputtered targets. In a first phase (*Campaign 1*) four HPGe detectors sur-

---

<sup>1</sup>Known until the end of 2010 as Forschungszentrum Dresden - Rossendorf (FZD).

rounded the target chamber at three different angles with respect to the beam axis; a few runs were acquired with only *Det1* at  $55^\circ$  to be able to resolve one weak  $\gamma$ -line very close to a beam induced background peak. In a second phase (*Campaign 2*) three detectors, including a segmented detector, have been used in two different configurations (*a* and *b*). They were positioned as close as possible to the target chamber to improve the statistics for the runs off resonance.

### 3.1.1 Accelerator and target chamber

The accelerator setup [73] consists of an ion source, injection magnet at  $90^\circ$ , terminal high voltage stage, stripper gas (nitrogen), a switching magnet and usual optics elements along the beam line to focus the beam in the target chamber. A Cs sputter ion source (model 860-C) produces negatively charged hydrogen atoms from a  $\text{TiH}_2$  pellet. An injection magnet at  $90^\circ$  operates a first charge/mass selection before the acceleration in the tandem. At this point the beam intensity can reach up to  $40 \mu\text{A}$ . Then the beam is sent inside the accelerator tube and through a gas nitrogen thickness to strip the electrons away from the protons, in order to accelerate them further in the second half of the tank characterized by an opposite voltage gradient.

The beam reaches the target chamber (fig. 3.1) after passing the switching magnet, an electrostatic quadrupole lens, electrostatic dipoles and a neutral particle trap. This device prevents the neutralized ions which cannot be accounted for in a charge measurement from reaching the target and make reactions. The neutral particle trap consists of an electric dipole positioned 1 m upstream from the target, bending the beam by  $7^\circ$ . The neutral particles continue at  $0^\circ$  and are absorbed on the internal wall.

A copper collimator of 5 mm diameter is placed 45 cm upstream from the target. A 12 cm long copper pipe of 2 cm diameter is inserted coaxial to the beam, at 5 mm distance from the target. During the experiment, the copper pipe was biased with -100 V to suppress secondary electrons from the target, which otherwise might have affected the beam current measurement in this Faraday cup. The target holder (fig. 3.2) was electrically insulated from the rest of the chamber and permitted a direct water cooling of the installed target.

Both currents on the collimator and the target holder were monitored, the latter was fed into a charge integrator coupled to a scaler, to provide the precise charge acquired during the runs. The beam intensity on the target ranged from 1 to  $15 \mu\text{A}$ , depending on the focusing conditions and the terminal voltage applied: the machine works more efficiently at energy ranges  $E_p > 0.8 \text{ MeV}$ . The current on the collimator was always comparable in size to the target current, so no beam wobbling was necessary. It is estimated that the electrical currents are accurate to  $\pm 1.0\%$ . The vacuum measured at 40 cm distance from the target was typically  $1 \cdot 10^{-7}$  mbar during the irradiation.

The absolute proton beam energy  $E_p$  was calibrated [74] based on the known energies



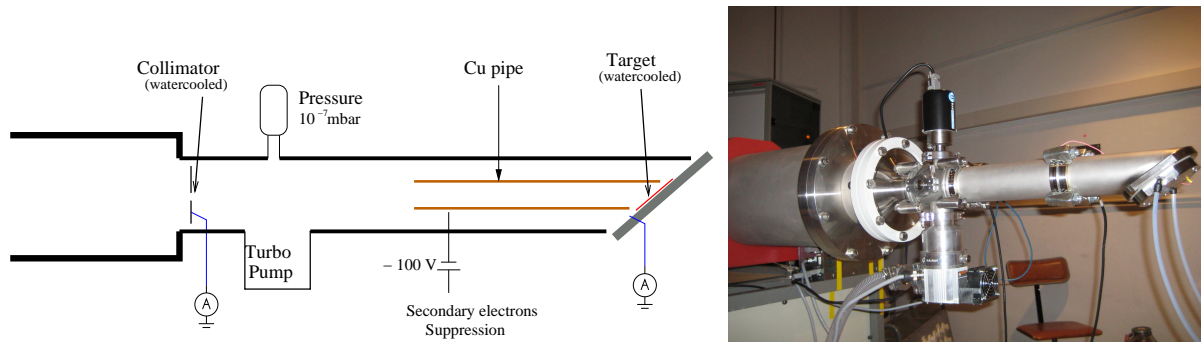


Figure 3.1: Schematic view and photo of the target chamber, with HPGe detectors removed.

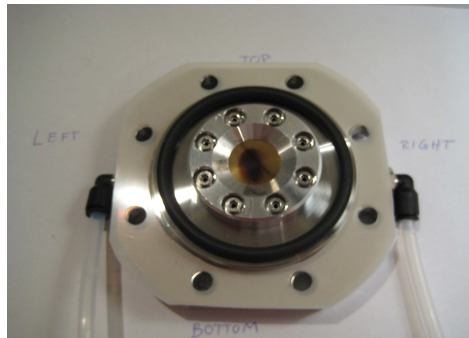


Figure 3.2: Photo of the target holder. The beam spot after irradiation is visible.

of eight resonances in the  $^{14}\text{N}(p,\gamma)^{15}\text{O}$ ,  $^{15}\text{N}(p,\alpha\gamma)^{12}\text{C}$ , and  $^{27}\text{Al}(p,\gamma)^{28}\text{Si}$  reactions ranging in energy from  $E_p = 278$  to  $2047$  keV. The observed beam energy spread was  $1.1$  keV at  $E_p = 897$  keV (sec. 3.1.2).

### 3.1.2 Targets

The solid targets have been produced with the reactive sputtering technique in the CIVEN facility in Venice/Italy. Nitrogen gas from commercial bottle was used during the production of targets, its isotopic abundance of  $^{15}\text{N}$  being not more than 1% different from the value in air ( $0.3663 \pm 0.0004$ )% [75] which has been found to be exceedingly stable [76] and assumed as the standard. In a recent study using commercial nitrogen tank gas of natural abundance, the  $^{15}\text{N}/^{14}\text{N}$  ratio was checked by mass spectrometry and found to be consistent with the natural abundance [77]. For the following analysis, the standard isotopic abundance [75] is assumed to hold with 1.0% uncertainty. Any effects of target degradation under the ion beam are expected to derive from atomic processes with negligible isotopic effects, so it is assumed here that the relevant behavior of the  $^{15}\text{N}$  atoms tracks that of the  $^{14}\text{N}$  atoms. Consequently, the same targets could be used for a parallel study of proton capture on  $^{14}\text{N}$  and  $^{15}\text{N}$ .

Two sets of targets have been used, the first set characterized by a layer of titanium nitride  $\text{TiN}^{\text{nat}}$   $200 \mu\text{g}/\text{cm}^2$  thick, on a  $0.22$  mm tantalum backing. The targets were placed

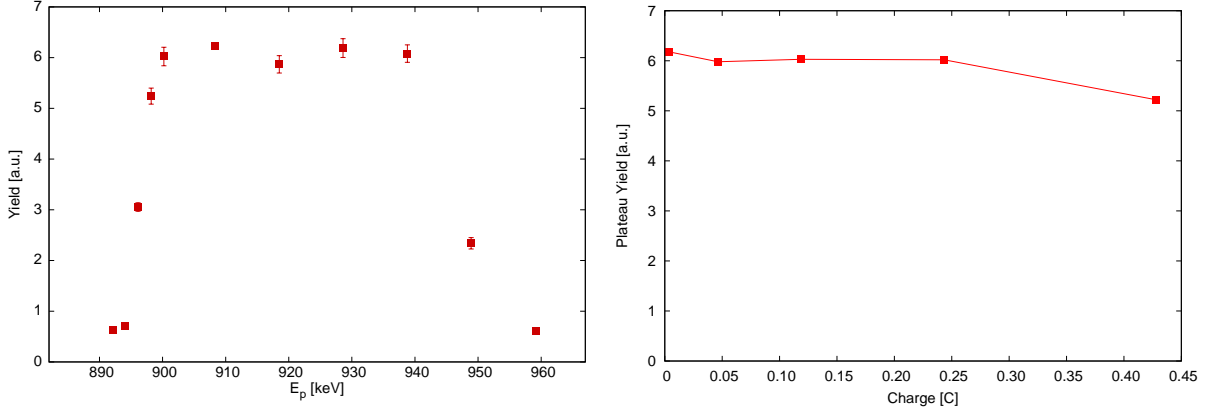


Figure 3.3: **Left:** target *Vom-TiN-3* profile obtained by scanning the  $^{15}\text{N}(p,\alpha\gamma)^{12}\text{C}$  resonance at  $E_p = 897$  keV; yield of the 4.4 MeV line versus proton energy (laboratory frame). **Right:** yield on the target plateau as a function of irradiation dose (Coulomb).

tilted by  $55^\circ$  with respect to the beam axis and directly water cooled.

The nitrogen content and distribution versus depth was monitored via the scan of the  $^{15}\text{N}(p,\alpha\gamma)^{12}\text{C}$  resonance at  $E_p = 897$  keV recording the yield of the 4.44 MeV  $\gamma$ -line from the decay of the first excited state of  $^{12}\text{C}$  (reaction scheme in fig. 3.14). The resonance is suitable for target scanning because its width  $\Gamma_{\text{lab}} = 1.57$  keV [78] is only slightly larger than the beam energy spread and its strength is large enough to allow fast scans (about one hour with usual beam intensity). That is not the case for the other available resonance at  $E_p = 430$  keV, which is narrower, thus in principle more suitable for a precise target scan, but its strength is one order of magnitude smaller than the chosen resonance.

The  $\gamma$ -ray spectra from the detector closest to the target (*Det 4*) were considered due to its higher efficiency. The proton beam energy was varied in the range from  $E_p = 880$  to 960 keV, with 1 to 10 keV step, thus measuring the stoichiometry at different depths in the TiN layer.

The target scans (fig. 3.3, left) show a rectangular profile, with an energetic width of 50 keV at  $E_p = 897$  keV and at  $55^\circ$ , a steep rise before reaching the plateau and a wide energy tail due to the increased energy straggling of the beam deep in the target. The target plateau decreased by no more than 15% during the experiment (fig. 3.3, right). The yield is not zero at the two extremes of the target scan, due to the influence of broad resonances located at higher energies and a possible nonresonant contribution. A straight line offset was subtracted based on the yields measured far enough from the resonance energy, considering the target energy thickness. The subtraction is 2% of the plateau height at 870 keV and 13% at 980 keV.

The target profiles were fitted with the following formula (adapted from [2]):

$$yield(E_p) = \frac{1}{norm} \left( \arctan \frac{E_p - E_{p,RES}}{\Gamma_1/2} - \arctan \frac{E_p - thickE_p - E_{p,RES}}{\Gamma_2/2} \right) \quad (3.1)$$

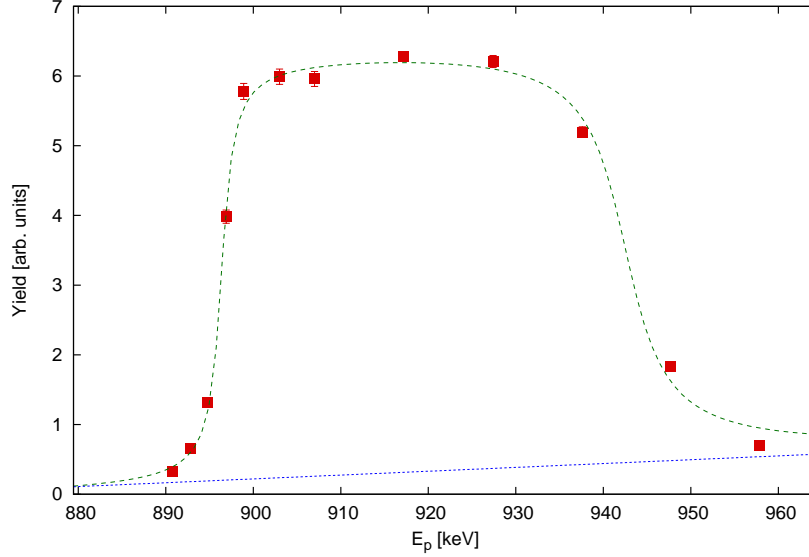


Figure 3.4: Target profile obtained by scanning the  $^{15}\text{N}(p,\alpha\gamma)^{12}\text{C}$  resonance at  $E_p = 897$  keV for target *Vom-TiN-4*, showing the yields of the 4.44 MeV  $\gamma$ -line versus proton energy (red squares). The fit to the data (green dashed line) includes a straight-line offset (blue dotted line) for nonresonant contribution.

Target scan	$E_{p,\text{RES}}$	$thickE_p$	$\Gamma_1$	$\Gamma_2$	$norm$
$^{15}\text{N}(p,\alpha\gamma)^{12}\text{C}$					
<i>Vom-TiN-4</i> , start	$896.3\pm 0.2$	$47\pm 1$	$1.9\pm 0.2$	$9\pm 2$	$0.48\pm 0.02$
<i>Vom-TiN-4</i> , end	$894.4\pm 0.2$	$48\pm 1.5$	$1.7\pm 0.3$	$8\pm 2$	$0.56\pm 0.02$
$^{14}\text{N}(p,\gamma)^{15}\text{O}$					
<i>Vom-TiN-3</i>	$1059.9\pm 0.4$		$3.9\pm 0.5$		$4.87\pm 0.07$

Table 3.1: Parameters obtained by fitting target scans with eq. 3.1.

which corresponds to the integral of the Breit-Wigner cross section  $\sigma_{\text{BW}}(E)$  from eq. (3.4) over a finite target of energy thickness  $thickE_p$  (the full width at half the value on the plateau).  $norm$  includes de Broglie wavelength, resonance strength and average effective stopping power,  $E_p$  and  $E_{p,\text{RES}}$  are the proton energy and the resonance energy in the laboratory frame. The two total widths  $\Gamma_1$  and  $\Gamma_2$  are the sums in quadrature of the pure resonance total width  $\Gamma_{\text{RES}}$  and the width due to the energy spread of the protons  $\Gamma_{\text{beam}}$ , and refer respectively to the surface and deepest layer of the target:

$$\Gamma_{1,2}^2 = \Gamma_{\text{RES}}^2 + \Gamma_{\text{beam}}^2(1,2). \quad (3.2)$$

$\Gamma_2$  is larger due to beam straggling.  $E_{p,\text{RES}}$ ,  $thickE_p$ ,  $norm$ ,  $\Gamma_1$  and  $\Gamma_2$  were all free parameters for the fit to the target profiles.

One example of a fitted target scan is shown in figure 3.4 and the fit parameters for target scans of *Vom-TiN-4* are shown in table 3.1. No difference in the parameters was observed after several days of irradiation (except  $norm$ , because of target degradation).

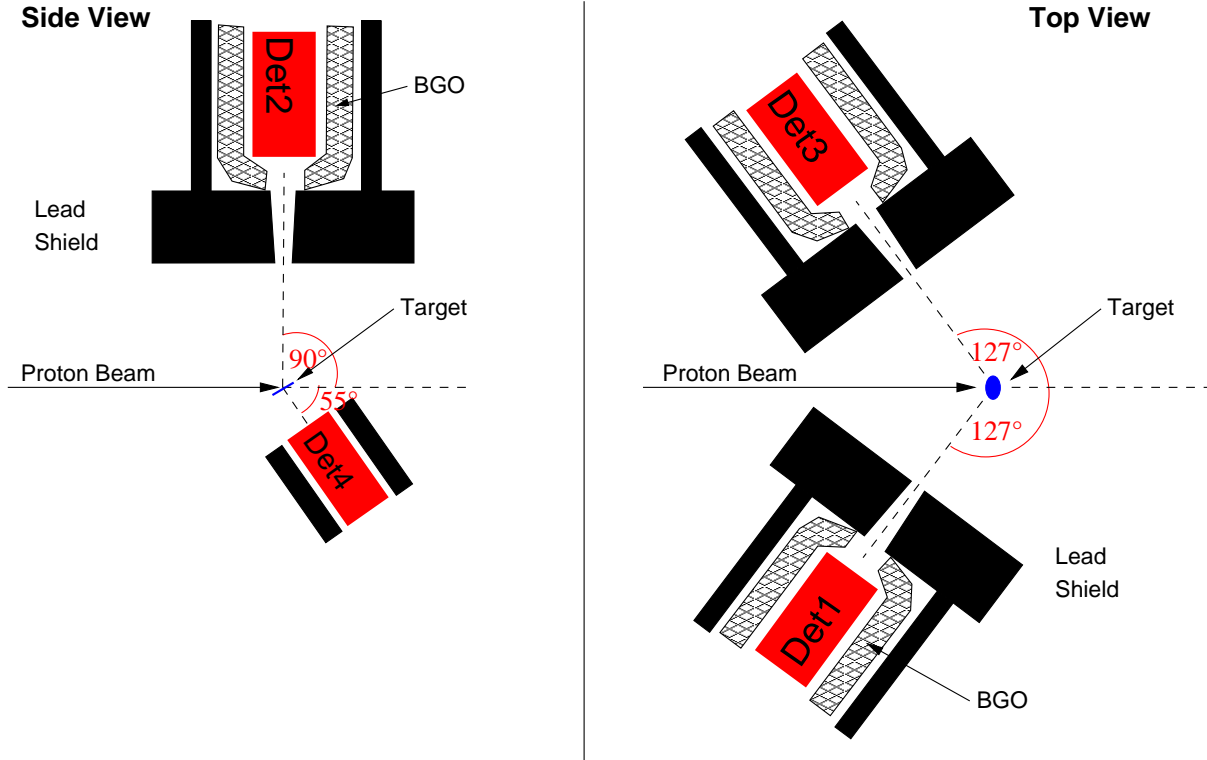


Figure 3.5: Scheme of the  $\gamma$ -ray detection setup for *Campaign 1*. **Left: side view** showing one HPGe detector (*Det2*) at  $90^\circ$  above the target and a 60% HPGe (*Det4*) at  $55^\circ$  tilted below the target. **Right: top view** showing the two 100% HPGe detectors (*Det1* and *Det3*) at  $\pm 127^\circ$  (left and right).

Substituting in eq. 3.2 the average observed  $\Gamma_1$  and the resonance total width  $\Gamma_{\text{RES}}$ , known from literature to be 1.57 keV [78], it has been possible to obtain the initial beam energy spread  $\Gamma_{\text{beam}}(1) = 1.1$  keV. This value was combined once again with the  $\Gamma_1$  from the partial target scan on the  $^{14}\text{N}(p,\gamma)^{15}\text{O}$   $E_p = 1058$  keV resonance (tab. 3.1) to give the total width  $\Gamma_{\text{RES}}$  of this resonance, i.e.  $(3.8 \pm 0.5)$  keV. The value is in agreement and more precise than the literature  $(3.9 \pm 0.7)$  keV [34].

The  $\Gamma_2$  width is dominated by the  $\Gamma_{\text{beam}}(2)$  after the straggling in the target and it is in good agreement with the  $(11 \pm 1)$  keV FWHM value obtained with the TRIM simulation program [60], for input  $E_p = 940$  keV,  $\text{Ti}_1\text{N}_{0.8}$  580 nm thickness.

### 3.1.3 Detection of emitted photons and efficiency

The number of events occurring at the target position has been measured by detecting the prompt high-energy photons emitted from the nuclear reactions. During *Campaign 1* the configuration of detectors around the target was the same as the one used in the photon-scattering NRF facility [65] at the superconducting electron accelerator ELBE in the same research center, that provided also the three anti-Compton HPGe detectors. The

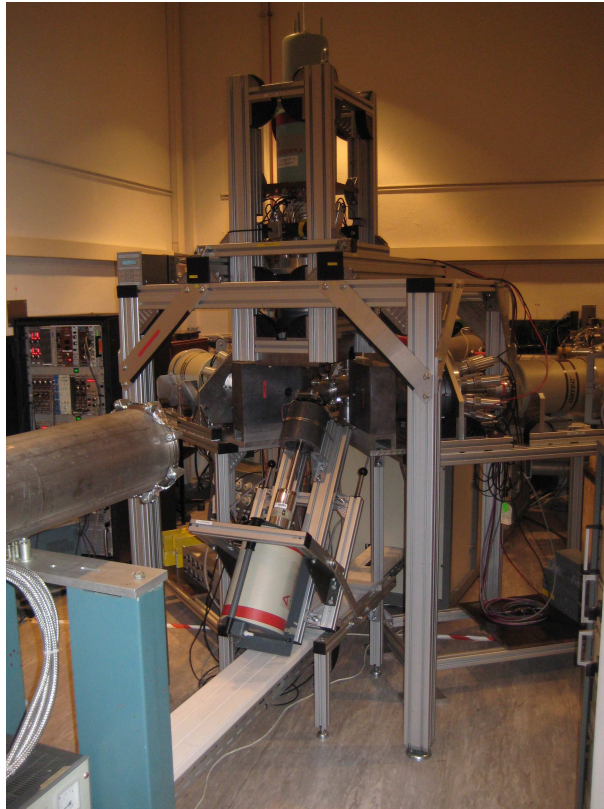


Figure 3.6: Photo of the  $\gamma$ -ray detection setup for *Campaign 1*. The beam comes from the right to the left outwards.

aim was two-fold: beside studying the nuclear reactions on the two isotopes of nitrogen, it was desired to obtain a detection efficiency curve for each detector based also on  $(p,\gamma)$  reactions. That allowed to extend the curve to higher energies from the region of calibrated radioactive sources and to check the simulations.

The  $\gamma$ -ray detection system consisted of four high-purity germanium (HPGe) detectors. Three 100% rel. efficiency HPGe detectors with BGO escape-suppression shield were used: two were placed horizontally at  $127^\circ$  (left and right) relative to the beam direction, with front faces at 32 cm from the target (hereafter called *Det1* and *Det3*). One was placed at  $90^\circ$  directly above the target, at 28 cm distance (*Det2*). Their BGO crystal was surrounded by 2 cm thickness Pb and they had a 10 cm frontal lead shield with a cone-shaped opening of 3-5 cm diameter. More details about these three detectors can be found in Ref. [65]. Care was taken so that their shielding and position with respect to the target reproduced the conditions in the NRF setup to  $\pm 0.5$  cm.

A fourth smaller HPGe (*Det4*) characterized by 60% relative efficiency, without escape-suppression, surrounded by a 1 cm thick lead shield was placed at 4 cm from the target, at downwards angle  $55^\circ$  (fig. 3.5).

This particular setup allowed to observe the emitted photons at three different angles,  $55^\circ$ ,  $90^\circ$ , and  $127^\circ$ , and to check the reproducibility for one angle, owing to the two

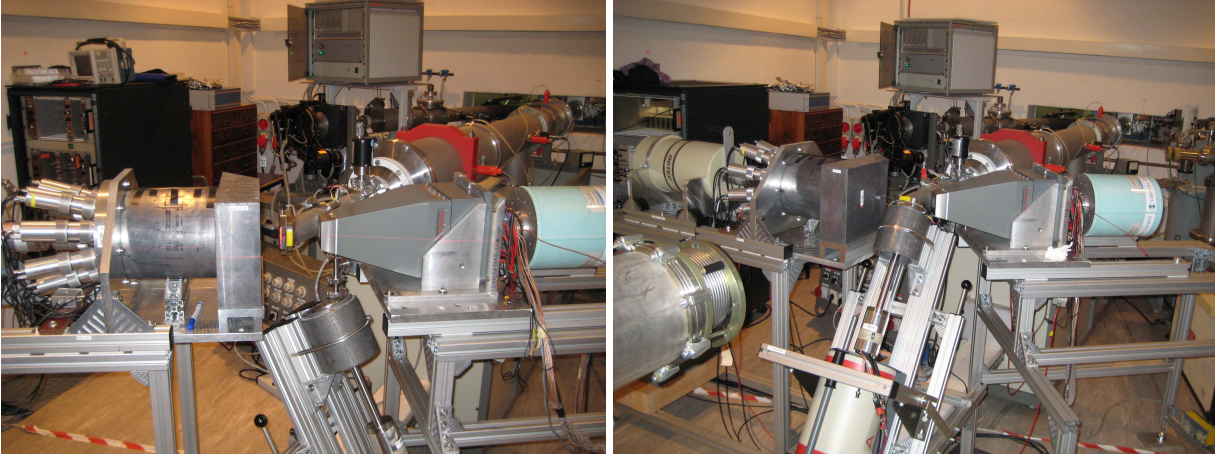


Figure 3.7: Photo of the  $\gamma$ -ray detection setup for *Campaign 2-a* (left) and *2-b* (right). The beam comes from the right to the left outwards.

detectors at  $\pm 127^\circ$ . The second order Legendre polynomial vanishes for angles equal to  $55^\circ$  and  $127^\circ$ , so that angular correlation effects are strongly diluted at these angles.

During *Campaign 2* the setup was optimized for the study of off resonance data, by placing the detectors as close as possible to the target chamber to increase their detection efficiency. In the first configuration (*2-a*), the BGO anti-Compton shielded *Det 1* was placed horizontally with its complete lead collimation structure described above at  $55^\circ$ , with its front face at 22.5 cm from the target. The *Det 4* occupied the position under the beam line at  $90^\circ$ , 14.5 cm from the target.

In configuration *2-b* the final segment of the target chamber was rotated axially by  $90^\circ$  in order to have the target holder facing the *Det 4* downwards at  $55^\circ$ , as in *Campaign 1*. The *Det 1* was shifted to a  $90^\circ$  position, at about 32 cm from the target.

The Eurysis Clover composite detector already used at LUNA and described in section 2.1.4 remained always positioned at  $135^\circ$  with the front faces of the Ge crystals at 14.5 cm from the target and the heavy-met collimator at 2 mm from the external walls of the beam line, during both configurations *2-a* and *2-b*. Fotos of the setup during *Campaign 2* are shown in fig. 3.7.

The acquisition system during *Campaign 1* was based on two different DAQs working in parallel. The part from the detectors to the amplifiers was in common and also the gate signals for the anticoincidence was formed similarly to what was done at LUNA (sec. 2.1.4, fig. 2.5). Then one branch was sent to an electronics chain and acquisition system based on the 14-bit histogramming Ortec 919/919E units [64] and the second branch to the so-called *Giesen-cards*. They were installed on a stand alone crate including a server where all the spectra and charge information were stored.

The *Giesen*-system showed a better resolution, but it was sometimes not reliable, prone to artifacts and more than once it has been necessary to substitute broken cards with spare ones. Both DAQs have been checked to produce the same counting rates, for



Figure 3.8: PTB radioactive source on a Ta backing installed in the target holder for efficiency calibration.

both BGO suppressed and unvetoes runs.

During *Campaign 2*, only the DAQ based on the Ortec 919/919E units was used. Both BGO on and off spectra were acquired for the Clover and *Det 1* detectors.

The detection efficiencies have been measured (Ref. [74] for *Campaign 1*) at low energy, from 662 to 1836 keV, by means of calibrated radioactive sources  $^{137}\text{Cs}$ ,  $^{60}\text{Co}$ ,  $^{88}\text{Y}$  from Physikalisch-Technische Bundesanstalt with quoted  $2\sigma$  activity uncertainty = 0.8–1.2%. The radioactive material occupied a point-like region of the size of 1 mm, embedded at the center of a polyethylene disk 0.3 mm thick (fig. 3.8). In the worst case, the attenuation of  $\gamma$ -rays of  $E_\gamma = 1.25$  MeV in a maximum thickness of 0.3 mm is less than 0.2%. The sources were placed at the position of the target on a blank Ta layer, the same as used for target production. The cooling water was let in the circuit in order to include all passive materials present also during the in-beam measurements.

With a procedure similar to the one described in section 2.4, the efficiency curve was then extended to higher energy via the ratios between low- and high-energy lines corresponding to the  $\gamma$ -rays in physical cascades following nuclear reactions. The known cascade branching ratios and angular distributions have been taken into account, as well as the corrections for summing-out (see Master's thesis by E. Trompler [74]). The resonances in  $^{11}\text{B}(p,\gamma)^{12}\text{C}$  at  $E_p = 675$  keV [79] and  $^{27}\text{Al}(p,\gamma)^{28}\text{Si}$  at  $E_p = 992$  keV [80] have been used for this purpose, in addition to the  $^{14}\text{N}(p,\gamma)^{15}\text{O}$  at  $E_p = 278$  keV used in section 2.4. A complete list of reactions used and corresponding  $E_\gamma$  of the cascade photons observed are summarized in table 3.2.

The fit performed on radioactive sources and nuclear reactions data points was of the form:

$$\varepsilon(E_\gamma; E_0) = \exp \left( a + b \cdot \ln \frac{E_\gamma}{E_0} + c \cdot \ln^2 \left( \frac{E_\gamma}{E_0} \right) + d \cdot \ln^3 \left( \frac{E_\gamma}{E_0} \right) \right) \quad (3.3)$$

where  $E_0$  was chosen equal to 6172 keV. The shape of the curve is not dependent on this value, while the error on the resulting fit parameters is. The parameters obtained for all four detectors and the uncertainties from the fit are summarized in table 3.3. The

Reaction	$E_p$ [keV]	$E_\gamma$ [keV]
$^{14}\text{N}(p,\gamma)^{15}\text{O}$	278	1385 - 6172, 765 - 6792, 2377 - 5181
$^{27}\text{Al}(p,\gamma)^{28}\text{Si}$	992	1779, 10763, 2839, 4498, 4743, 6020, 6265
$^{11}\text{B}(p,\gamma)^{12}\text{C}$	675	12138 - 4439

Table 3.2: Nuclear reactions used to extend the efficiency curve at higher energies. The resonance proton energy  $E_p$  and the cascade photon energies are reported. In the case of the  $^{27}\text{Al}(p,\gamma)^{28}\text{Si}$  resonance there are no pure 1:1 cascades: the  $\gamma$ -lines used are listed, the two most intense first.

Fit parameters	<i>Det1</i>	<i>Det2</i>	<i>Det3</i>	<i>Det4</i>
$E_0$	6172	6172	6172	6172
$a$	$-8.570\pm 0.036$	$-8.640\pm 0.054$	$-8.620\pm 0.047$	$-6.334\pm 0.022$
$b$	$-1.097\pm 0.031$	$-1.210\pm 0.046$	$-1.092\pm 0.043$	$-1.226\pm 0.022$
$c$	$-0.331\pm 0.061$	$-0.402\pm 0.089$	$-0.305\pm 0.081$	$-0.315\pm 0.040$
$d$	$-0.057\pm 0.019$	$-0.069\pm 0.027$	$-0.050\pm 0.025$	$-0.048\pm 0.012$

Table 3.3: Fit parameters in eq. 3.3 and their uncertainty, for the detection efficiencies of all four detectors in the *Campaign 1* setup.

efficiency curves, residuals and uncertainties for two detectors during *Campaign 1*, one close (*Det4*) and one far from the target (*Det2*) are plotted in fig. 3.9 and 3.10.

The fits have been repeated by varying  $E_0$  and calculating the uncertainty on  $\varepsilon(E_\gamma = E_0)$  from the parameters' uncertainties. An energy-dependent uncertainty has been obtained for the  $\gamma$ -detection function (fig. 3.9 and 3.10, bottom). The error is smaller in the energy region of the radioactive sources, because of precise data there. In the high-energy region the total uncertainty ranges from 2.5 to 4%, also depending on the detector. That reduces to  $\approx 1\%$  if just the  $\gamma$ -efficiency ratios of two high-energy  $\gamma$ -rays from the same detector are used, as in section 3.4.



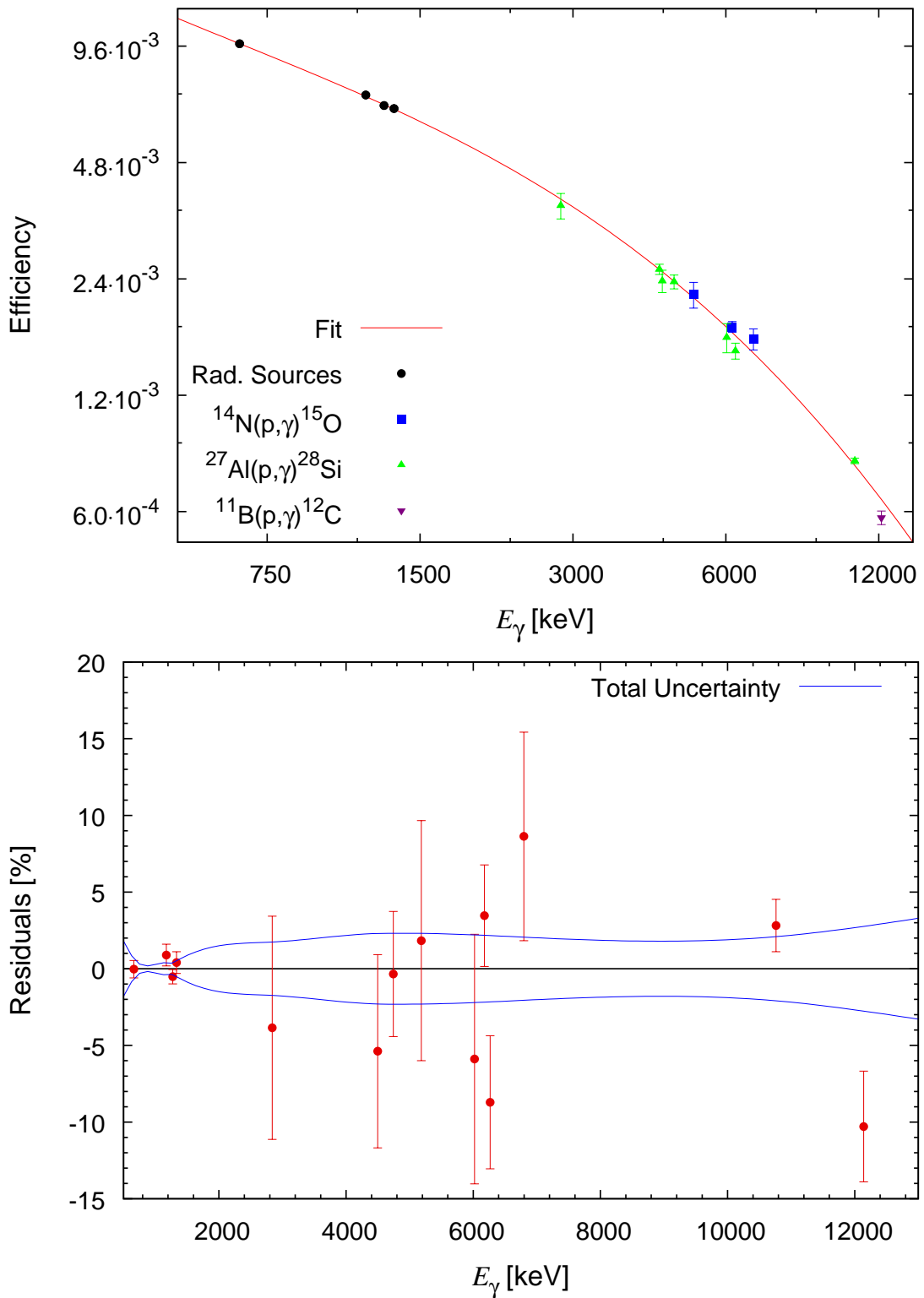


Figure 3.9: **Top:** Efficiency curve of the 60% HPGe at 4 cm distance from the target, at  $55^\circ$  (*Det4*, *Campaign 1*). **Bottom:** Residuals of the fitted points and total uncertainty calculated from the errors on the fit parameters versus detection energy.

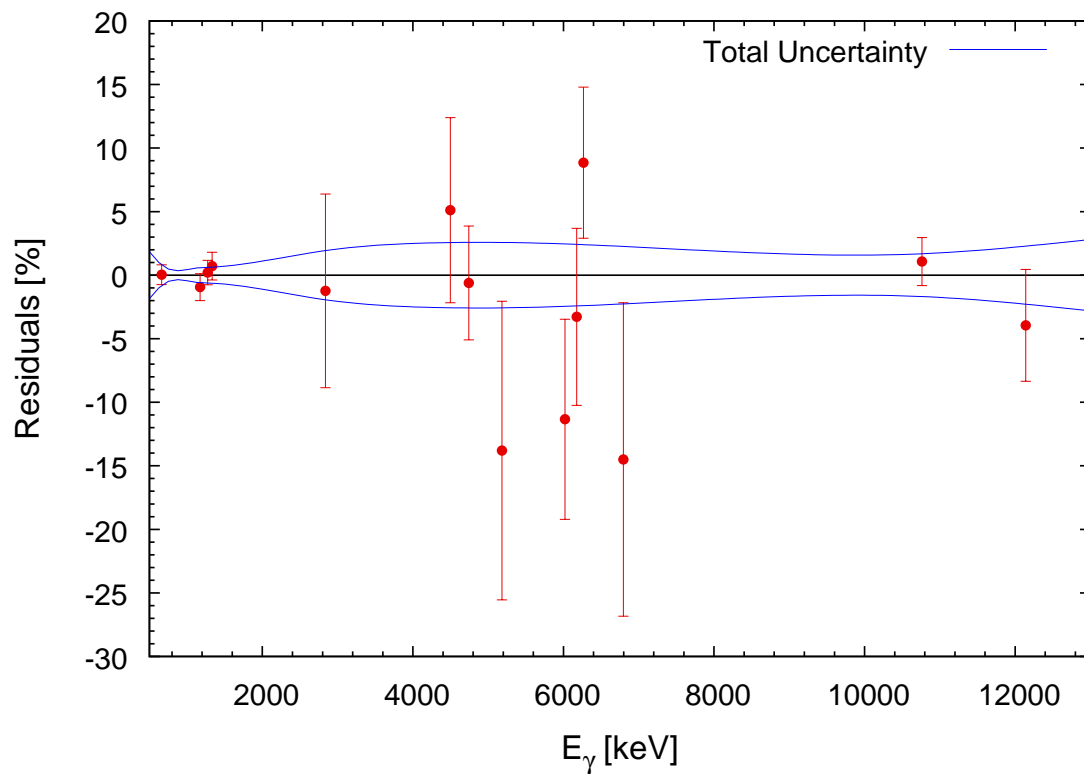
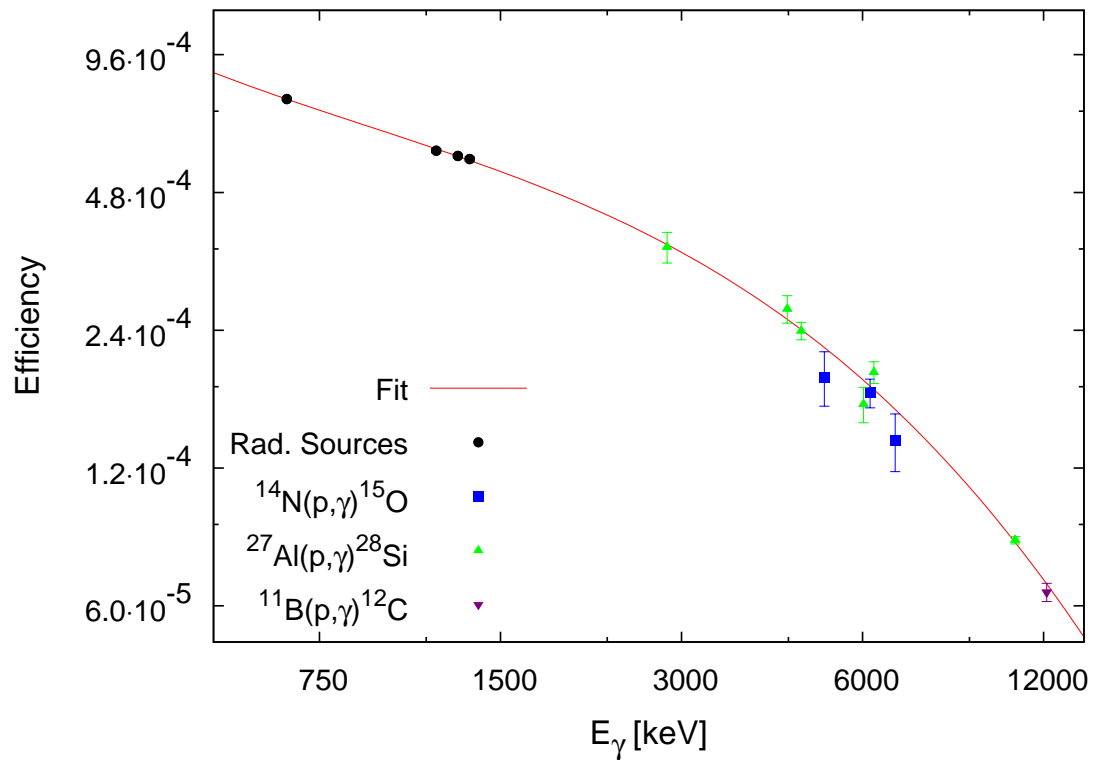


Figure 3.10: **Top:** Efficiency curve of the 100% HPGe, at 28 cm above the target chamber, at 90° (*Det2, Campaign 1*). **Bottom:** Residuals of the fitted points and total uncertainty calculated from the errors on the fit parameters versus detection energy.

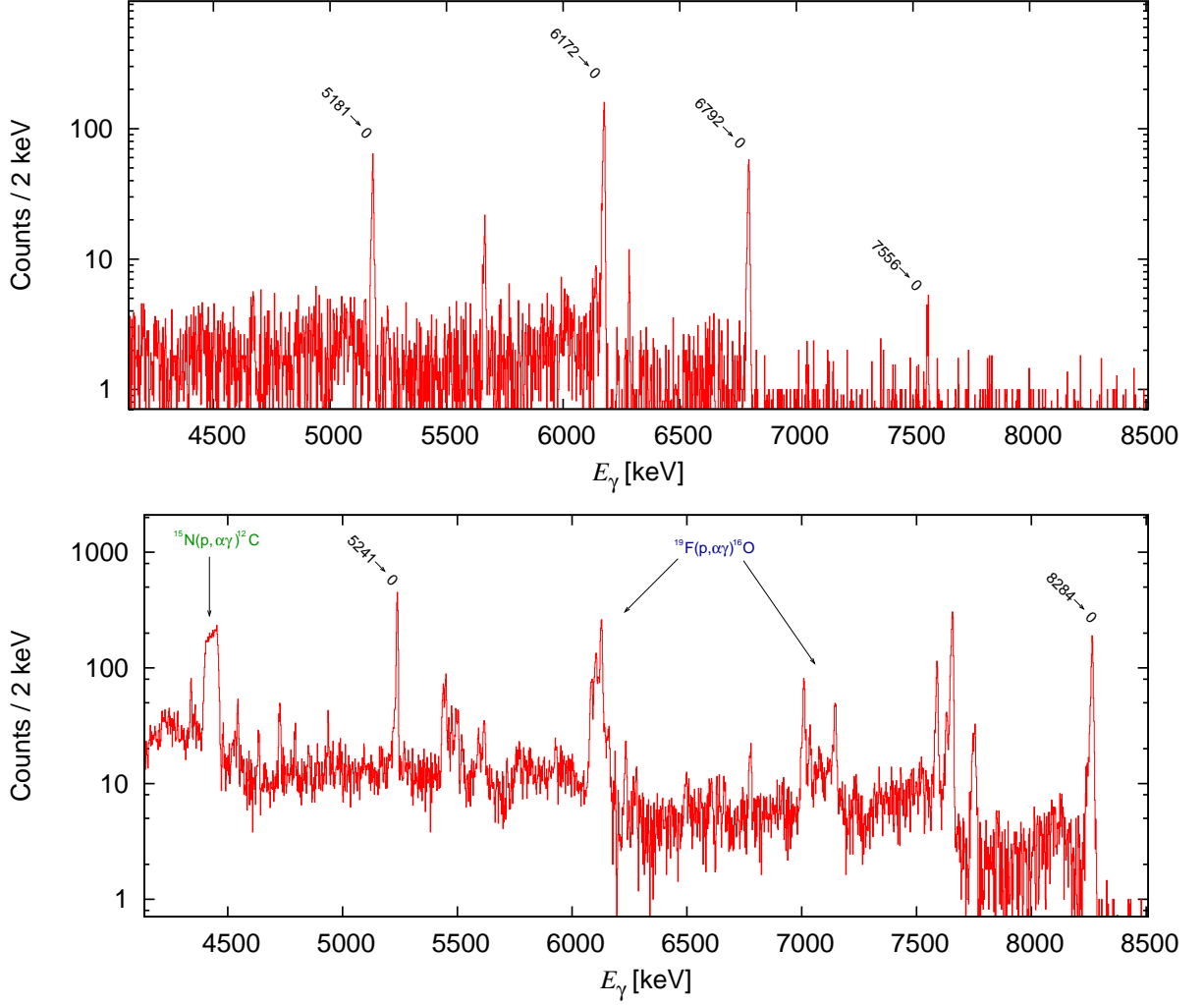


Figure 3.11:  $\gamma$ -ray spectra of *Det1* acquired on resonances in  $^{14}\text{N}(p,\gamma)^{15}\text{O}$  reaction, at  $E_p = 278$  keV (**top**) and  $E_p = 1058$  keV (**bottom**). The transitions of interest for the reaction under study are marked with black tilted tags. The most intense peaks of beam induced background from the  $^{19}\text{F}(p,\alpha\gamma)^{16}\text{O}$  and  $^{15}\text{N}(p,\alpha\gamma)^{12}\text{C}$  reaction are shown as well.

### 3.2 $^{14}\text{N}(p,\gamma)^{15}\text{O}$ resonances

The  $\gamma$ -ray spectra of *Det1* (fig. 3.11) show the decay of the resonances at  $E_p = 278$  and 1058 keV ( $E = 259$  and 987 keV in the center of mass frame). The resonances correspond to the capture to the excited states at  $E_x = 7556$  and 8284 keV in  $^{15}\text{O}$ . Due to the large beam induced background for  $E_p > 500$  keV, only the secondary  $E_\gamma > 4$  MeV emissions are taken into account in the present analysis, where the contribution from parasitic reactions is smaller.

In both cases the beam energy has been chosen about 15 keV higher than the resonance energy in order to completely cover their energy width with the present target thickness. Resonance scans (fig. 3.12) have been performed, in order to locate the plateau indepen-

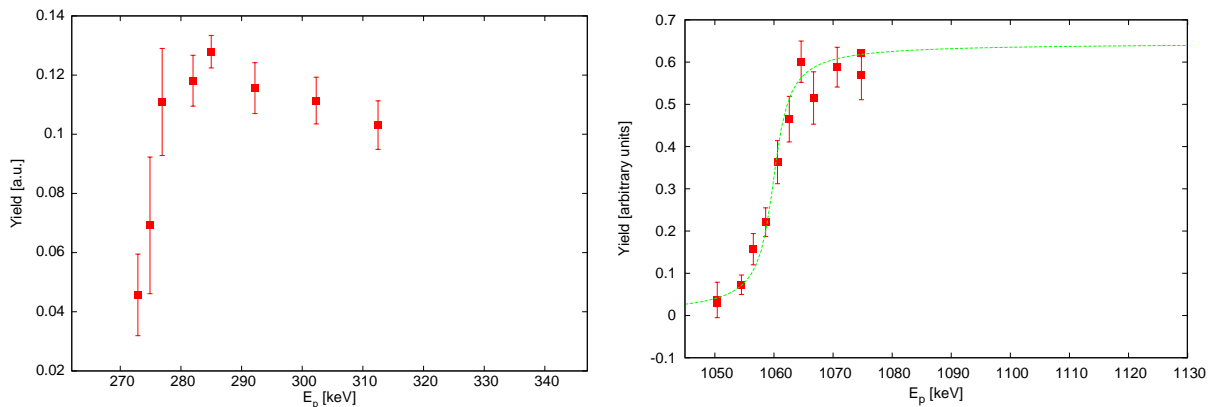


Figure 3.12: **Left:** Resonance scan at  $E_p = 278$  keV. **Right:** The same for the  $E_p = 1058$  keV resonance.

dently from the accelerator energy calibration and to be completely sure to measure the yield corresponding to an infinite target situation (eq. 3.5). Counting statistics of  $\approx 1\%$  combining all four detectors has been reached.

Runs well above ( $E_p = 1133$  keV) and below ( $E_p = 1049$  keV) the  $E_p = 1058$  keV resonance were recorded, in order to subtract an interpolated yield for nonresonant capture in the resonance region. The procedure has been (i) to convert the yields into adimensional S-factors, (ii) to perform a linear interpolation between the values at effective energies above and below resonance and (iii) subtract the yield corresponding to the interpolated S-factor at the resonance energy. The subtraction amounted to  $\approx 100\%$  for the  $6792 \rightarrow 0$  transition, which proceeds only through the nonresonant mechanism at these energies, and less than 6% for the two most intense transitions  $5241 \rightarrow 0$  and  $8284 \rightarrow 0$ .

The true coincidence summing effect was non-negligible only for *Det4* and was corrected for analytically based on eqns. (2.8) and (2.11) in section 2.6. The correction was not larger than 3% (with 0.5% uncertainty) for the  $\gamma$ -lines of interest, i.e. the 6.79, 6.17 and 5.18 cascades for the  $E_p = 278$  keV resonance and the 5.24 and GS transitions for the 1058 keV.

### 3.2.1 Angular distribution of emitted $\gamma$ -rays

The angular distribution of the  $1/2^+$  resonance at  $E_p = 278$  keV is expected to be isotropic [34, 38]. This assumption was experimentally verified for transitions through all excited states, though within their high statistical uncertainty. For this measurement, the yields at different energies  $E_\gamma$  were obtained using special detection efficiency curves, the fit of which did **not** include the data points from the  $^{14}\text{N}(p,\gamma)^{15}\text{O}$  reaction. Only the transition through 6172 keV excited state is shown (fig. 3.13, left panel), due to its higher branching ratio. In the present work, all  $\gamma$ -rays from the decay of this resonance are assumed to exhibit isotropy.

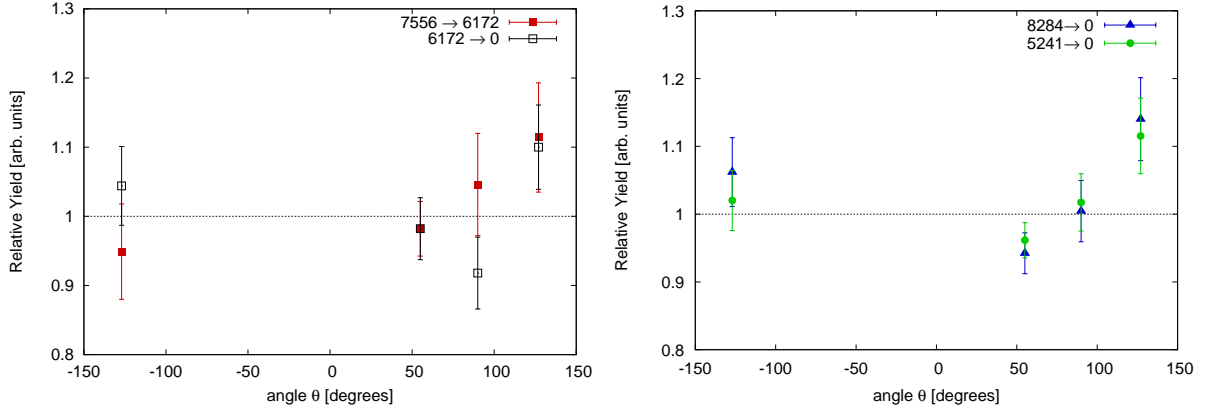


Figure 3.13: **Left:** Angular distribution of  $\gamma$ -rays of the  $E_p = 278$  keV resonance in  $^{14}\text{N}(p,\gamma)^{15}\text{O}$ . **Right:** The same for the  $E_p = 1058$  keV resonance.

As to the resonance at  $E_p = 1058$  keV, the  $\gamma$ -rays corresponding to the capture to the ground state and 5241 keV excited state have shown isotropic angular distribution to a level of 2% [81, 38]. The relative angular distribution was checked also in the present experiment (fig. 3.13, right) and was found to be compatible with isotropy within the uncertainties. In the present work, isotropy is assumed and a 3% uncertainty on angular distribution is taken into account, in case there were smaller effect that cannot be resolved with the present statistic.

For the off-resonance analysis (sec. 3.5), only *Det4* has been used because of its larger detection efficiency and its low dependence from angular correlation due to its proximity to the target and its  $55^\circ$  angle with respect to the beam axis.

### 3.2.2 Branching ratios

The branching ratios on the  $E_p = 278$  keV resonance have been already measured with high statistics in the experiment at LUNA (sec. 2) and they have not been investigated again with the present setup at HZDR.

The branching ratios for the decay of the  $E_p = 1058$  keV resonance have been measured using the high-statistics spectra of *Det4* (table 3.4), with the off-resonant contribution subtracted based on reference runs below and above the resonance. Angular corrections have been neglected for all transitions, because *Det4* is positioned at  $55^\circ$  (where the second-order Legendre polynomial vanishes) close to the target. Consequently the attenuation factors due to the finite detection solid angle are large (appendix A) and smooth out any remaining anisotropies.

For the weak  $\gamma$ -lines at 5181, 6172 and 6792 keV, the Compton-suppressed spectrum provided by *Det1* placed in a modified setup at  $55^\circ$  and close as possible to the target have been used to obtain precise ratios of counting rates relative to the 5241 keV transition. The results are summarized in table 3.4 and compared with literature data.

$E_x$ [keV]	Ref. [81]	Ref. [38]	Compilation [34]	Present work
6859	1.2±0.3	1.2±0.2	1.2±0.3	1.2±0.3
6172	2.2±0.6	2.6±0.1	2.2±0.6	1.7±0.4
5241	42.7±0.5	46±2	42.2±0.5	45.4±0.8
5181		1.2±0.1	1.2±0.1	1.1±0.6
0	53.8±0.25	49±2	53.2±0.25	50.5±0.8

Table 3.4: Branching ratios, in %, for the decay of the resonance at  $E_p = 1058$  keV in  $^{14}\text{N}(p,\gamma)^{15}\text{O}$ . Results from the literature [81, 38], from the standard compilation [34] based on these papers, and from the present work are shown.

The branching ratios in the standard compilation [34] are based on one work [81]. The only exception is the weak  $8284 \rightarrow 5181$  branch reported by Ref. [38], which was adopted, leading to a recalculation of the other branches [34].

For the two strongest transitions,  $8284 \rightarrow 0$  and  $8284 \rightarrow 5241 \rightarrow 0$ , the present branchings are in agreement with Ref. [38], but not with Ref. [81]. The present data show the  $8284 \rightarrow 5241$  transition to be stronger than reported in Ref. [81]. In that work [81], a sodium iodide scintillating detector had been used that was surrounded with a large Compton-suppressing guard detector. A correction has to be applied for the events lost in the detector due to vetoes by coincident cascade  $\gamma$ -rays. It is conceivable that the correction applied in Ref. [81] might have been different for the single  $8284 \rightarrow 0$   $\gamma$ -ray than for the  $\gamma$ -rays of the  $8284 \rightarrow 5241 \rightarrow 0$  cascade, leading to some systematic uncertainty. The present values for the weaker transitions  $8284 \rightarrow 6859$ ,  $8284 \rightarrow 6172$ , and  $8284 \rightarrow 5181$  are in good agreement with the literature [81, 38] but show generally less precision.

### 3.3 $^{15}\text{N}(p,\alpha\gamma)^{12}\text{C}$ resonances

The  $^{15}\text{N}(p,\alpha\gamma)^{12}\text{C}$  reaction and its narrow resonances at  $E_p = 430$  and  $897$  keV are interesting from several points of view. The reaction belongs to the CNO cycle too, but opposite to the  $^{14}\text{N}(p,\gamma)^{15}\text{O}$ , it represents a very fast step, thus there is no urgent need to increase the precision on its cross section. However, because of the naturally occurring small isotopic abundance of  $^{15}\text{N}$  in the targets, its strong resonances are well suited for fast target scans, monitoring their depth-profiles and degradation during the experiment. That is what has been done also during the present experiment.

The  $^{15}\text{N}(p,\alpha\gamma)^{12}\text{C}$  reaction is also useful in applied physics. In material science, the resonance at  $E_p = 430$  keV is frequently used for the hydrogen depth profiling technique using high energy  $^{15}\text{N}$  ions [82, e.g.] ( $E_{\text{beam}} = 6.39$  MeV) and detecting the  $4.439$  MeV  $\gamma$ -ray from the reaction. Usually, reference standard samples are used if absolute results are required, even because the precision of its strength is only  $\approx 10\%$  [83]. A more precise  $\omega\gamma$  would in principle allow an absolute measurement of hydrogen profiles without reference

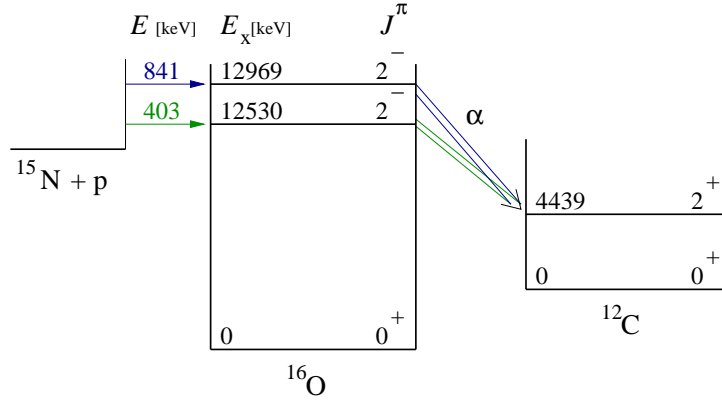


Figure 3.14: Reaction scheme of the  $^{15}\text{N}(p,\alpha\gamma)^{12}\text{C}$  (Q value 4965 keV). Energy levels of interest of  $^{16}\text{O}$  and  $^{12}\text{C}$  are shown.

to a standard.

The targets employed contained a natural occurring abundance of  $^{15}\text{N}$  isotope. That allowed not only to obtain daily target profiles based on the scan of the  $^{15}\text{N}(p,\alpha\gamma)^{12}\text{C}$  resonance at  $E_p = 897$  keV, but also to gain higher precision on the  $\omega_\gamma$  strength of this and a weaker resonance, namely at  $E_p = 897$  and  $430$  keV ( $E_x = 12.969$  and  $12.530$  MeV of  $^{16}\text{O}$ ). The analysis was performed relative to the well known strength of the  $^{14}\text{N}(p,\gamma)^{15}\text{O}$  resonance at  $E_p = 278$  keV.

The reaction proceeds via formation of the compound nucleus  $^{16}\text{O}$  and emission of an alpha particle with allowed angular momentum  $l_\alpha = 1, 3$  and a  $^{12}\text{C}^*$  excited nucleus, which then decays to ground state by emitting a photon (fig. 3.14). Due to angular momentum and parity conservation, the  $^{12}\text{C}^*$  nucleus following a resonant reaction results always in its first excited state at  $E_x = 4439$  keV (lifetime = 44 ps), for both resonances. As a consequence, observing this line in the  $\gamma$ -ray spectrum accounts for the complete number of resonant reactions which take place.

Nevertheless, nonresonant reactions may occur, which feed the same excited level in  $^{12}\text{C}$ . The nonresonant yield at resonance energy has been estimated by interpolating from runs well above and below the resonance. The subtraction amounted to 5.9% of the total observed 4.44 MeV  $\gamma$ -line yield at  $E_p = 917$  keV, which is the beam energy chosen during the run to study the resonance at  $E_p = 897$ . The subtracted quantity was 0.8% at  $E_p = 447$  keV, in the case of the resonance at  $E_p = 430$ . Nonresonant reactions may feed the ground state of  $^{12}\text{C}$  as well, but that does not lead to a  $\gamma$ -ray emission.

The peak corresponding to this decay is strongly enlarged around  $E_\gamma = 4.44$  MeV, because of (i) the large Doppler effect of the photon emitted from the excited  $^{12}\text{C}$  nucleus moving fast after the  $\alpha$ -particle emission and (ii) the particle and nucleus being emitted at all possible angles with respect to the detector. The peak width is 53 keV for the 430 keV resonance and about 10 keV larger for the 897 keV resonance, due to the higher kinetic energy available to the  $^{12}\text{C}$  nucleus (and alpha particle).

parameter	897 keV res	430 keV res
$a_2$	$0.26 \pm 0.02$	$0.37 \pm 0.02$
$a_4$	$0.40 \pm 0.03$	$0.79 \pm 0.03$

Table 3.5: Literature angular distribution parameters for the two investigated resonances of  $^{15}\text{N}(\text{p},\alpha\gamma)^{12}\text{C}$ , obtained from re-fitting the experimental yield vs angle.

### 3.3.1 Angular distribution of emitted $\gamma$ -rays

One difficulty in the analysis has been the strong anisotropy of the decay of the  $E_x = 4439$  keV level of  $^{12}\text{C}$ , but fortunately its angular distribution at the energy of the two resonances of the  $^{15}\text{N}(\text{p},\alpha\gamma)^{12}\text{C}$  are known [84]. The pattern is similar for both resonances due to the same spin and parity of the excited levels in  $^{16}\text{O}$  and  $^{12}\text{C}$ .

As a first step, the literature results have been compared to the ones from the present experiment. The literature yields versus angles from [84] for both resonances have been fitted with Legendre polynomials up to the fourth order (eq. (A.1)), with attenuation factors  $Q_{2,4}$  calculated [85] for the 100 cc scintillator detector used. The fitting parameters and uncertainties (tab. 3.5) obtained are used for the curves plotted in figure 3.15.

The literature curves (for  $Q = 1$ ) are compared to the present yields for both resonances: the data plotted are the ratios of yields relative to the yield of *Det2*. The error includes counting statistics and systematics due to the efficiency curves up to 4%. The point at  $55^\circ$  is corrected for finite angle, thus a comparison with the data at other angles is possible, with additional error due to angular distribution correction.

A normalization had to be applied in order to compare present experimental data from different detectors in different geometries, meaning different attenuation factors  $Q$ . Detectors *Det1,2,3* have  $Q = 1$ , due to their large distance from the target. The yield from *Det4* in close distance has been corrected for the ratio between the literature  $W(\theta)$  for  $Q = 1$  and the same function evaluated for  $Q$ s calculated for the position and size of *Det4* based on [85].

The data point of *Det4* in the right panel of figure 3.15 (430 keV resonance) underwent a special correction for its efficiency because its yield on the 897 keV resonance relative to the other detectors for that acquisition session was found to be 10% different from the other days and sessions, which suggests that its distance to the target was different with respect to the following acquisition sessions. That is realistic because *Det4* is the only one moved forth and back every time the target is changed. Being very close to the target chamber, its efficiency is very sensitive to the precise distance.

From the comparison in figure 3.15 it is concluded that the present experimental results are in fair agreement with the literature angular distribution.

As a reliability check, the ratio 430/897 of the yields of the 4439 keV  $\gamma$ -peak for two consecutive runs on the two different resonances was calculated for all detectors (table 3.6).



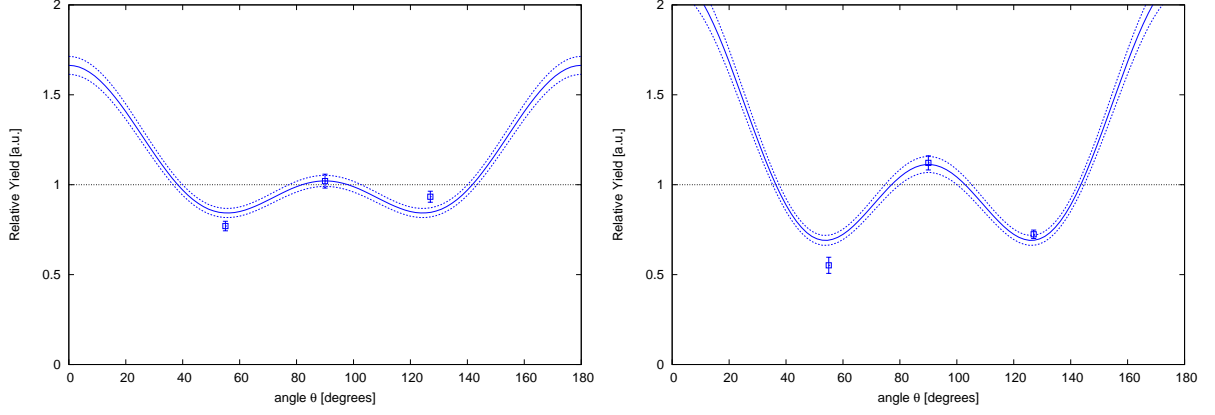


Figure 3.15: Angular distribution of  $\gamma$ -rays emitted by  $^{15}\text{N}(p,\alpha\gamma)^{12}\text{C}$  at the  $E_p = 897$  keV (left) and 430 keV (right) resonance. The parametrization refers to the pure case of detectors at far distance ( $Q_{2,4}=1$ ), with dashed lines showing the uncertainty. Present data are normalized to the literature value at angle  $90^\circ$  (squares).

Detector	$\theta$	d [cm]	Calculated		Literature [84]		Uncorrected exp. yield	Corrected yield ratio 430/897
			$Q_2$	$Q_4$	$W_{430}(\theta)$	$W_{897}(\theta)$		
<i>Det1</i> [present]	$-127^\circ$	32	$1.00^{+0.00}_{-0.01}$	$1.00^{+0.00}_{-0.01}$	$0.69\pm 0.01$	$0.85\pm 0.01$	$0.071\pm 0.002$	$0.087\pm 0.004$
<i>Det2</i> [present]	$90^\circ$	28	$1.00^{+0.00}_{-0.01}$	$1.00^{+0.00}_{-0.01}$	$1.11\pm 0.02$	$1.02\pm 0.02$	$0.100\pm 0.003$	$0.091\pm 0.004$
<i>Det3</i> [present]	$127^\circ$	32	$1.00^{+0.00}_{-0.01}$	$1.00^{+0.00}_{-0.01}$	$0.69\pm 0.01$	$0.85\pm 0.01$	$0.070\pm 0.002$	$0.086\pm 0.004$
<i>Det4</i> [present]	$55^\circ$	4	$0.70\pm 0.05$	$0.25\pm 0.09$	$0.92\pm 0.03$	$0.96\pm 0.01$	$0.076\pm 0.001$	$0.079\pm 0.003$
<i>Det4'</i> [10]	$0^\circ$	10	$0.94\pm 0.02$	$0.80\pm 0.04$	$1.98\pm 0.05$	$1.57\pm 0.05$	$0.106\pm 0.001$	$0.084\pm 0.004$

Table 3.6: Experimental yield ratio 430/897 of the two  $^{15}\text{N}(p,\alpha\gamma)^{12}\text{C}$  resonances at different angles. In the last column, the values are corrected for the angular distributions.

The same ratio has also been calculated for a similar experiment [10] with targets enriched in  $^{15}\text{N}$  and *Det4'* placed at  $0^\circ$ , where the anisotropy is very pronounced, and 10 cm distance (table 3.6, last line). The yield ratio depends only on the effective detection angle of the device, hence the angular distribution and its attenuation. After correcting for these two effects, the values for the yield ratio are consistent (table 3.6).

In the present work, the literature angular distributions and their uncertainties have been assumed to be correct.

### 3.4 Resonance strengths of the $^{14}\text{N}(p,\gamma)^{15}\text{O}$ and $^{15}\text{N}(p,\alpha\gamma)^{12}\text{C}$ reactions

When a beam with energy slightly higher than the resonance impinges on an extended target, it produces resonant reactions at a particular depth inside the target, after the ions underwent some energy loss until the resonance energy is reached. The total width of the three resonances under study here is small compared to the energy loss in the present targets, consequently it is assumed that they obey a Breit-Wigner-like description, where

the cross section  $\sigma_{\text{BW}}(E)$  is given [2] by the function:

$$\sigma_{\text{BW}}(E) = \frac{\lambda^2}{4\pi} \omega \frac{\Gamma_1 \Gamma_2}{(\Gamma/2)^2 + (E - E_{\text{res}})^2} \quad (3.4)$$

where  $\lambda$  is the de Broglie wavelength at the resonance energy  $E_{\text{res}}$ ,  $\omega$  is a statistical term depending on the spin of the states involved in the reaction,  $\Gamma$  is the total resonance width and  $\Gamma_{1,2}$  are the partial widths, assumed independent from  $E$ .

If the energy width of the target  $\text{thick}E_p$  is much larger than the width  $\Gamma$  of the resonance, the target extends over all energies where the resonant cross section is non-negligible. Then, the observed yield will not depend on the total target thickness, but just on how many target ions are present in the resonance energy region. In the present case it is possible to apply the classical definition of the thick target yield  $Y_\infty$  [2], which is the maximum yield obtained by integrating the cross section in eq. (3.4) over the target thickness  $\text{thick}E_p$ , with  $\text{thick}E_p \gg \Gamma$ :

$$Y_\infty^i = \frac{\lambda^2}{2} \beta^i \frac{\omega\gamma}{\epsilon}; \quad Y_\infty = \frac{\sum_i Y_\infty^i}{\sum_i \beta^i} = \frac{\lambda^2}{2} \frac{\omega\gamma}{\epsilon}, \quad (3.5)$$

where  $Y_\infty^i$  is the experimental yield for branch  $i$  with branching ratio  $\beta^i$  corrected for  $\gamma$ -efficiency and angular distribution,  $\epsilon$  is the effective stopping power [2], and  $\lambda$  is again the de Broglie wavelength at the resonance energy.  $\omega\gamma$  is the resonance strength:

$$\omega\gamma = \frac{2J+1}{(2j_1+1)(2j_2+1)} \frac{\Gamma_1 \Gamma_2}{\Gamma}, \quad (3.6)$$

which depends on the widths  $\Gamma$  and the particles' total angular momenta  $j_{1,2}$  and spin of the resonance state  $J$ .

$\epsilon$  is the stopping power related to the nuclear species taking part in the reaction under study. If the target of interest is  $^{14}\text{N}$ ,  $\epsilon$  is given by:

$$\epsilon^{14}(E_p) = \epsilon_{\text{N}}(E_p) \left(1 + \frac{n^{15}\text{N}}{n^{14}\text{N}}\right) + \epsilon_{\text{Ti}}(E_p) \frac{n_{\text{Ti}}}{n^{14}\text{N}} \quad (3.7)$$

and for  $^{15}\text{N}$  as target:

$$\epsilon^{15}(E_p) = \epsilon_{\text{N}}(E_p) \left(1 + \frac{n^{14}\text{N}}{n^{15}\text{N}}\right) + \epsilon_{\text{Ti}}(E_p) \frac{n_{\text{Ti}}}{n^{15}\text{N}} = \frac{n^{14}\text{N}}{n^{15}\text{N}} \epsilon^{14}(E_p). \quad (3.8)$$

The isotopic abundance  $n^{15}\text{N}/n^{14}\text{N}$  is always taken to be the standard value,  $\frac{0.3663}{99.6337}$  [75], with an uncertainty of 1.0% [86]. The ratio of resonance strengths for two different resonances at  $E_p = n$  keV ( $n \in \{430; 897; 1058\}$ ) and at  $E_p = 278$  keV, the reference strength, is then given by:

$$\frac{\omega\gamma_n}{\omega\gamma_{278}} = \frac{Y_{\infty,n}}{Y_{\infty,278}} \frac{\lambda_{278}^2}{\lambda_n^2} \frac{\epsilon^a(n)}{\epsilon^{14}(278)}; \quad a \in \{14; 15\}. \quad (3.9)$$

The ratio of yields  $Y_{\infty,n}/Y_{\infty,278}$  was taken from the weighted average of the ratios obtained for each of the four detectors corrected for angular distributions, after checking

Reaction	Literature [34, 78]		Present		Literature	New recommended
	$E_p$ [keV]	$\Gamma_{\text{lab}}$ [keV]	$\omega\gamma_n/\omega\gamma_{278}$	$\omega\gamma$ [eV]	$\omega\gamma$ [eV]	$\omega\gamma$ [eV]
$^{14}\text{N}(p,\gamma)^{15}\text{O}$	278	1.12	$\stackrel{\text{Def}}{=}1$	—	$0.0131\pm 0.0006$	—
$^{14}\text{N}(p,\gamma)^{15}\text{O}$	1058	3.8	$27.8\pm 0.9$	$0.364\pm 0.021$	$0.31\pm 0.04$ [38]	$0.353\pm 0.018$
$^{15}\text{N}(p,\alpha\gamma)^{12}\text{C}$	430	0.1	$(1.73\pm 0.07)\cdot 10^3$	$22.7\pm 1.4$	$21.1\pm 1.4$ [83]	$21.9\pm 1.0$
$^{15}\text{N}(p,\alpha\gamma)^{12}\text{C}$	897	1.57	$(2.77\pm 0.09)\cdot 10^4$	$362\pm 20$	$293\pm 38$ [88]	$362\pm 20$

Table 3.7: Relative and absolute resonance strength values  $\omega\gamma$ . The errors for the new absolute  $\omega\gamma$  values include the uncertainty from the reference strength  $\omega\gamma_{278}$ . See the text for a discussion of the new recommended values.

that they were consistent. The ratio of effective stopping powers at different energies  $\epsilon^a(n)/\epsilon^{14}(278)$  is only slightly dependent on the target stoichiometry  $n_{\text{Ti}}/n_{^{14}\text{N}}$ . The main uncertainty associated with stopping powers is their absolute scale and not the energy dependence beyond the Bragg peak [87], and only the energy dependence is needed here. The stoichiometric ratio varied for the worst case from  $\text{Ti}_1\text{N}_{0.93}$  (virgin target) to  $\text{Ti}_1\text{N}_{0.80}$  (after a  $\text{H}^+$  dose of 0.97 Coulomb). Using the stopping powers from SRIM [60], this change affected  $\epsilon^{14}(1058)/\epsilon^{14}(278)$  by just 0.1%. In order to include also theoretical uncertainties, 1.0% uncertainty is assumed for  $\epsilon^a(n)/\epsilon^{14}(278)$ .

The target deterioration under beam bombardment has been corrected for based on the change observed in the yield of the  $E_p = 897$  keV resonance in  $^{15}\text{N}(p,\alpha\gamma)^{12}\text{C}$  on the plateau of the target scans, leading to 0.9% uncertainty.

For calculating the reference yield of the  $E_p = 278$  keV resonance, the yields of the three peaks corresponding to the decay of the  $E_x = 6792, 6172,$  and  $5182$  keV excited states of  $^{15}\text{O}$  and their precisely known branching ratios [35] have been used. The strength of the  $E_p = 1058$  keV resonance has been obtained based on the yields from the two strongest transitions,  $5241\rightarrow 0$  and  $8284\rightarrow 0$ , and the presently measured branching ratios (tab. 3.4).

For the two resonances in  $^{15}\text{N}(p,\alpha\gamma)^{12}\text{C}$ , the broad  $\gamma$ -peak at 4439 keV was used to calculate the yield. The nonresonant contribution was not subtracted, because the results are intended to improve the hydrogen depth profiling method, that makes use of the total yield without distinction of resonant and nonresonant reactions.

The strength ratio was found to be  $\omega\gamma_{430}/\omega\gamma_{897} = (6.25\pm 0.17)\cdot 10^{-2}$ , in fair agreement with the literature value of  $(5.8\pm 0.2)\cdot 10^{-2}$ . That value had been obtained with two detectors placed at  $55^\circ$  [88], neglecting angular distribution effects and the resultant uncertainty. The present error bar includes these effects. Because of a target change, the ratio  $\omega\gamma_{430}/\omega\gamma_{278}$  had to be calculated in two steps

$$\frac{\omega\gamma_{430}}{\omega\gamma_{278}} = \frac{\omega\gamma_{430}}{\omega\gamma_{897}} \frac{\omega\gamma_{897}}{\omega\gamma_{278}} \quad (3.10)$$

leading to slightly higher uncertainty. All the errors for the resonance strength ratios are summarized in table 3.8.

Using these strength ratios and the reference strength  $\omega\gamma_{278} = 13.1\pm 0.6$  meV [31], new

	1058 keV	897 keV	430 keV
Counting statistics	<b>1.7%</b>	<b>1.6%</b>	<b>1.0%</b>
$\gamma$ -efficiency (relative) [74]	0.7%	1.3%	
Decay branching ratio	1.2%	0.5%	
Angular distribution	1.8%	1.1%	1.9%
Stopping power ratio	1.0%	1.0%	1.0%
Isotopic abundance $n_{15\text{N}}/n_{14\text{N}}$		1.0%	
Target degradation $n_{14\text{N}}/n_{\text{Ti}}$	0.9%	0.9%	0.8%
Beam intensity	1.0%	1.0%	1.0%
<b>Final uncertainty of <math>\omega\gamma_n/\omega\gamma_{\text{ref}}</math></b>	<b>3.3%</b>	<b>3.1%</b>	<b>2.7%</b>
Reference strength $\omega\gamma_{\text{ref}}$	4.6%	4.6%	5.5%
<b>Final uncertainty of <math>\omega\gamma_n</math></b>	<b>5.7%</b>	<b>5.5%</b>	<b>6.1%</b>

Table 3.8: Uncertainties affecting the resonance strength ratios  $\omega\gamma_n/\omega\gamma_{\text{ref}}$ . The 1058 and 897 keV resonances are referred to the 278 keV resonance,  $\omega\gamma_{\text{ref}} = \omega\gamma_{278}$ . The 429 keV resonance is referred to the 897 keV resonance,  $\omega\gamma_{\text{ref}} = \omega\gamma_{897}$ . Its uncertainty includes also the 1.0% from the isotopic abundance  $n_{15\text{N}}/n_{14\text{N}}$ .

absolute resonance strengths have been obtained for the three resonances under study (table 3.7).

Near the 1058 keV resonance in  $^{14}\text{N}(\text{p},\gamma)^{15}\text{O}$ , the R-matrix fits for capture to the ground state show a pronounced interference pattern [45, 46, 72] (fig. 4.3, bottom panel). Therefore, the shape of the excitation curve for this transition does not obey the ideal Breit-Wigner form. However, the present rather thick target covers the entirety of the energy range directly affected by the resonance and therefore the present strength value is unaffected by this fact.

The present strength value of the 1058 keV resonance in  $^{14}\text{N}(\text{p},\gamma)^{15}\text{O}$  is higher than the previous number [38], but still in agreement within the uncertainty. Therefore, a weighted average of the two numbers is formed and recommended for future use (table 3.7).

Also for the 897 keV resonance in  $^{15}\text{N}(\text{p},\alpha\gamma)^{12}\text{C}$ , the present value is higher than the literature [88]. That value [88] had been obtained just with two detectors at  $55^\circ$  angle and neglecting angular distribution effects. However, the literature angular distribution [84] is lower than unity at  $55^\circ$  (fig. 3.15) as confirmed also by the present data, so this assumption leads to a systematically low value. Consequently, the  $\omega\gamma$  value from the present experiment is recommended.

For the 430 keV resonance, the present strength, determined based on  $\gamma$ -spectroscopy, has the same precision as the literature value which had been obtained by  $\alpha$ -spectroscopy instead [83]. That work [83] had used an  $\alpha$ -detector at  $30^\circ$  and applied the  $\alpha$ -particle angular distribution. Based on the two independent results from  $\alpha$ -spectroscopy [83] and

from  $\gamma$ -spectroscopy (present work), a weighted average for the strength is recommended that has just 4% uncertainty (table 3.7).

## 3.5 Preliminary off-resonance cross sections of the $^{14}\text{N}(p,\gamma)^{15}\text{O}$ reaction

Several runs have been recorded varying the proton energy from 0.5 to 2.5 MeV to investigate the reaction in the extended region where no resonances are present. The importance of the off-resonance data in the R-matrix framework is briefly reminded. Although the R-matrix theory is by definition mainly concerned with resonances, their strengths, energy widths and positions, the off-resonance data are important to constrain the fit in the regions where no easy prediction can be done.

### 3.5.1 $\gamma$ -ray spectra

The spectra in the runs at energies  $E_p$  far from resonances were affected by intense beam induced background. The expected yield from different captures to levels in  $^{15}\text{O}$  is much lower than at the resonance. Even only the Compton events by an intense peak of beam-induced background were enough to cover the signal in the region of interest.

Two strong sources of disturbance were present throughout the acquisition. The  $\gamma$ -line at 4.44 MeV from the  $^{15}\text{N}(p,\alpha\gamma)^{12}\text{C}$  reaction arising from  $^{15}\text{N}$  isotopes in the target was used for target scans and the properties of two resonances have been studied. The line at 4.44 MeV is only disturbing the low energy part of the  $\gamma$ -ray spectra, so the present study of the peaks lying at  $E_\gamma > 5$  MeV is not affected.

The intense  $\gamma$ -line from the decay of the  $^{16}\text{O}$  excited state at 6.13 MeV has been a major problem. It is caused by the  $^{19}\text{F}(p,\alpha\gamma)^{16}\text{O}$  reaction and its yield is higher at some proton energies in correspondence to resonances (fig. 3.16). Even just its off-resonance yield is such that it overcomes completely the signals from the  $^{14}\text{N}(p,\gamma)^{15}\text{O}$  reaction. Even worse, at higher beam energies the reaction populates further levels of  $^{16}\text{O}$ , at 6.92 and 7.12 MeV, adding more noise to the 6.79 MeV peak region (fig. 3.17).

The  $E_\gamma = 6172$  keV peak was also affected by the intense 6.13 MeV line: Doppler shifted events occur at 40 keV above and below the level energy for a detector at  $127^\circ$  with respect to the beam axis (see inset in fig. 3.17). However, for detectors “behind” the target, like *Det4* in the present setup, the events with  $E_\gamma > 6.13$  MeV are only due to the limited energy resolution of the detector. The oxygen nuclei emitted inwards in the target are completely stopped before emitting the photon, because the stopping time is much lower than the lifetime of the excited level, equal to 18.4 ps. Therefore the emitted  $\gamma$ -ray has energy  $E_\gamma = E_x$  (the level energy), not affected by the Doppler shift.

In *Campaign 1*, the yield of the peak at 6.13 MeV increased along with the irradiation

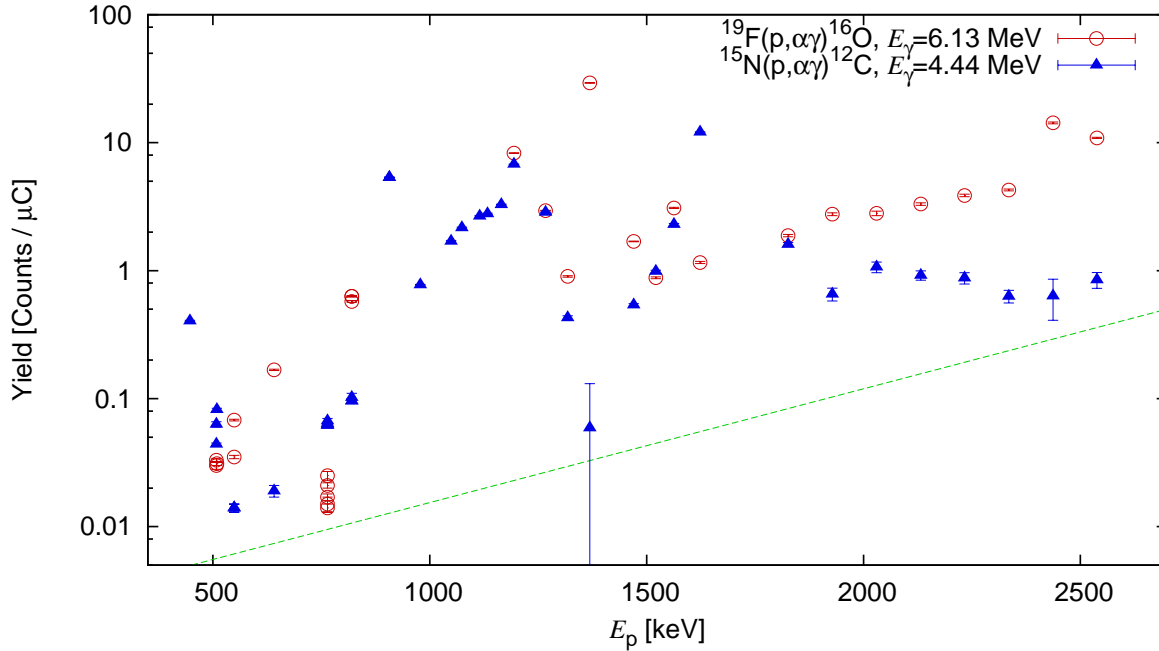


Figure 3.16: Yield obtained from *Det4* of the broad peak at  $E_\gamma = 6.13$  MeV from the  $^{19}\text{F}(p,\alpha\gamma)^{16}\text{O}$  (red circles) and  $E_\gamma = 4.44$  MeV from the  $^{15}\text{N}(p,\alpha\gamma)^{12}\text{C}$  (blue triangles). The dashed line gives an idea of the maximum yield from the reaction of interest.

for runs performed at the same energy (e.g. target scans at  $E_p \approx 900$  keV), by about 10 times in one week measurement. A slightly larger increase is observed for *Det4*, which had no lead wall in front of it for collimation and could consequently collect  $\gamma$ -rays coming from a more extended region of the chamber. That means that the fluorine has been accumulating somewhere inside the target chamber as a consequence of the beam.

The reason was identified with the beam hitting on the collimator, initially not water-cooled, resulting in an intense heat. Enough to partially melt or burn the Teflon insulators that insulated it electrically (and thermally!) from the chamber, to enable a reliable current measurement. The products of the burning diffused and deposited in regions where it could be hit by the beam.

Due to the the difficulties encountered in analyzing the spectra, the acquisition of the off-resonance data was repeated during *Campaign 2*, with the following enhancements: (i) the collimator was still insulated but properly watercooled to prevent overheating due to the beam; (ii) a 100% HPGe detector with good lead collimation and BGO anti-Compton veto system was installed at  $55^\circ$  behind the target and as close as possible to it, to avoid the positive Doppler shift and possibly enable the measurement of the  $E_\gamma = 6172$  keV peak; (iii) the same Clover detector with the BGO anti-Compton shield described in section 2.1.4 was placed opposite to the previous detector at  $125^\circ$ , to increase the statistics.

A comparison between  $\gamma$ -ray spectra obtained with *Det1* in *Campaign 1* and in *Campaign 2-a* at  $E_p \approx 1350$  keV is shown in fig. 3.17. The counts were normalized for beam

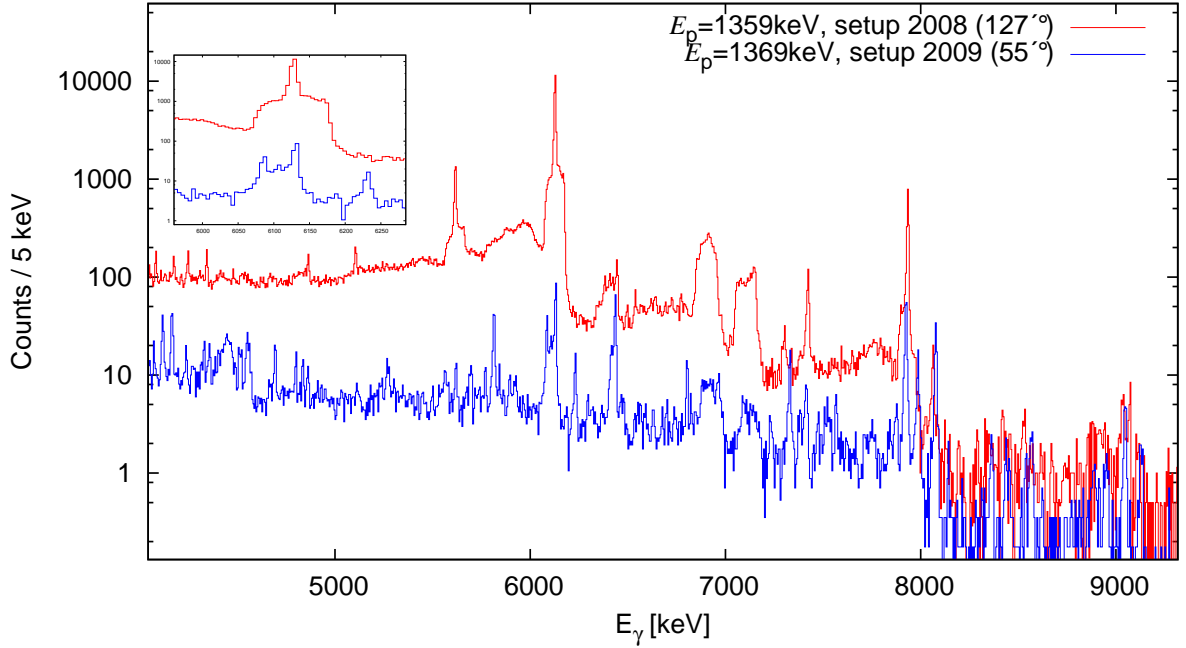


Figure 3.17: Comparison of  $\gamma$ -ray spectra properly normalized from *Det1* during *Campaign 1* at  $127^\circ$  (red) and *Campaign 2-a* at  $55^\circ$  (blue). The inset zooms on the particular structure of the broad 6.13 MeV peak from  $^{19}\text{F}(p,\alpha\gamma)^{16}\text{O}$ , which is different for the two detection angles.

charge, distance from the target (32 and 22.5 cm) and target thickness (approximately halved in those used in *Campaign 2*). The more counts in *Campaign 1* spectrum are due to the additional beam-induced background, mainly given by reactions on fluorine deposited in the target chamber.

### 3.5.2 Analysis and results

Considering only the setup of *Campaign 1*, four peak areas for the capture to the 6792 keV excited state in  $^{15}\text{O}$  and two for the ground state transition have been considered reliable. They have been converted to S-factors based on the same procedure described in section 2.9. The error bars reflect the statistical uncertainties.

The results  $E_{eff}$ ,  $S_{\text{exper}}(E_{eff})$  and their uncertainties are listed in table 3.9 and plotted in fig. 3.18. They are in fair agreement with the data by Schröder et al. [38].

Capture to ground state		Capture to 6792 keV state	
$E$	$S_{\text{GS}} \pm \Delta_{\text{stat}}$	$E$	$S_{6792} \pm \Delta_{\text{stat}}$
689	$0.29 \pm 0.02$	449	$1.37 \pm 0.15$
1093	$0.26 \pm 0.05$	688	$1.02 \pm 0.02$
		738	$1.12 \pm 0.16$
		1092	$1.03 \pm 0.15$

Table 3.9: S-factor results for capture to the ground state and to the excited state at 6792 keV in  $^{15}\text{O}$ . The effective energy  $E$  is given in keV, the S-factor  $S$  in keV b and the uncertainties are only statistical.

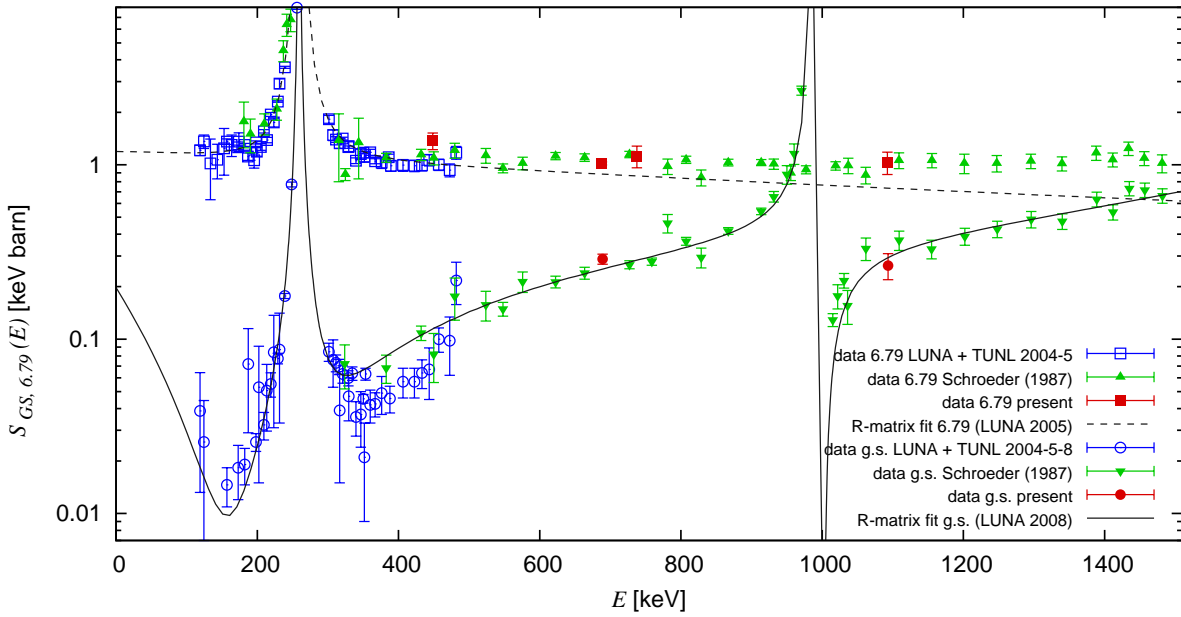


Figure 3.18: S-factor data obtained from the present experiment both for the capture to 6792 keV excited state (red squares) and ground state (red circles) of  $^{15}\text{O}$ , compared with other literature data (Schröder, LUNA+TUNL) and the fits from [35, 72].



# Chapter 4

## R-matrix analysis

After cross sections and resonance strengths are measured in a laboratory on Earth, the following step is to obtain their extrapolated values at the low stellar energies normally not reached in the experiments. The method to do that may rely only on theory, or both theory and experimental data, like in the R-matrix framework. The data for the capture to the ground state obtained in chapter 2 were included in a R-matrix fit, to test their effect on the extrapolated  $S_{\text{GS}}(0)$  value. Eventually, only the two data sets not affected by summing-in were included in a negligible summing-in fit, giving 0.20 keV b and solving the previous literature discrepancy for this transition (sec. 1.4).

### 4.1 What is R-matrix?

The single-level Breit-Wigner formula (eq. 3.4) is an easy approach to interpret resonance data, but it is truly applicable given certain requirements. The resonance should be well isolated, narrow and with no influences from other resonances. In the R-matrix framework these assumptions are relaxed, therefore a more reliable interpretation of the observed experimental data is possible. Interference effects between multiple resonant and nonresonant contributions are accounted for.

The R-matrix approach divides the particle configuration space into internal and external region. The interactions in the internal region are described by many-body nuclear physics and depend on the set of states of the compound nucleus (*poles*), while the external region contains only the Coulomb interaction and depends only on energy, mass, charge and angular momentum of the couple of particles interacting, called *channel*. The different interactions in the two regions determine the wave functions and they must match at the boundary surface, as well as their derivatives. More details can be found in the review [89], considered the “bible” of R-matrix theory.

For the end-user, the R-matrix framework is a fit to experimental cross section (or S-factor) data that include a treatment of the resonances based on theory and leave few parameters free to vary. They correspond to the properties of the poles: resonance energy,

entrance and exit channel widths.

The code [45] used in the present analysis, introduces an additional pole not corresponding to real resonances, positioned at high energy and with a very broad resonance width. It is called *background pole* and it takes into account the slowly varying offset in the S-factor, due to nonresonant mechanism and far away resonances.

A new code has been released [90], that is multilevel and multichannel, i.e. it considers all the poles and their interference, while simultaneously fitting the data for more than one reaction channel, for example radiative and scattering channels. That could be an advantage if some parameters are better constrained by reactions other than the one of interest.

## 4.2 Influence of present data

Some limited R-matrix calculations have been performed using the code [45] made available by P. Descouvemont, to get some insight into the changes produced by the present experimental data. Before adding the present points to the data set to be fitted, the previous fits by LUNA [36] and TUNL [37] have been reproduced by applying the procedure to the same data sets used in literature (figures 4.1 and 4.2). This check confirmed that the code was used properly.

For the following analysis, only the  $\gamma$ -widths of the background pole and of the sub-threshold resonance at  $E = -505$  keV, corresponding to the 6792 keV excited state, have been considered as free parameters in the fits. An interaction radius of  $a=5.5$  fm has been adopted for all. The  $\chi^2$  function of the two parameters was investigated, showing a bit of correlation between the two and giving the uncertainty on the fits parameters and the extrapolated value.

The effect of the results in section 2.7.1 were tested by repeating the previous two R-matrix fits by LUNA and TUNL after including the three present data points.

**The TUNL fit** has been repeated after adding the present points to see the change in the extrapolated S-factor. The input parameters for the poles at 0.259, 0.985, 2.187 MeV, position and proton width of the background pole have taken unchanged from the previous TUNL fit [37]. Only the data from TUNL and the present relative data have been used, converted to absolute S-factors with the TUNL R-matrix fit for capture to the 6792 keV state [37].

The fit (called fit B) and data are plotted in fig. 4.1. The result,  $S_{GS}(0)=0.23$  keV b , is clearly not consistent with the previous TUNL result  $S_{GS}(0)=0.49\pm 0.08$  keV b , which is ruled out.

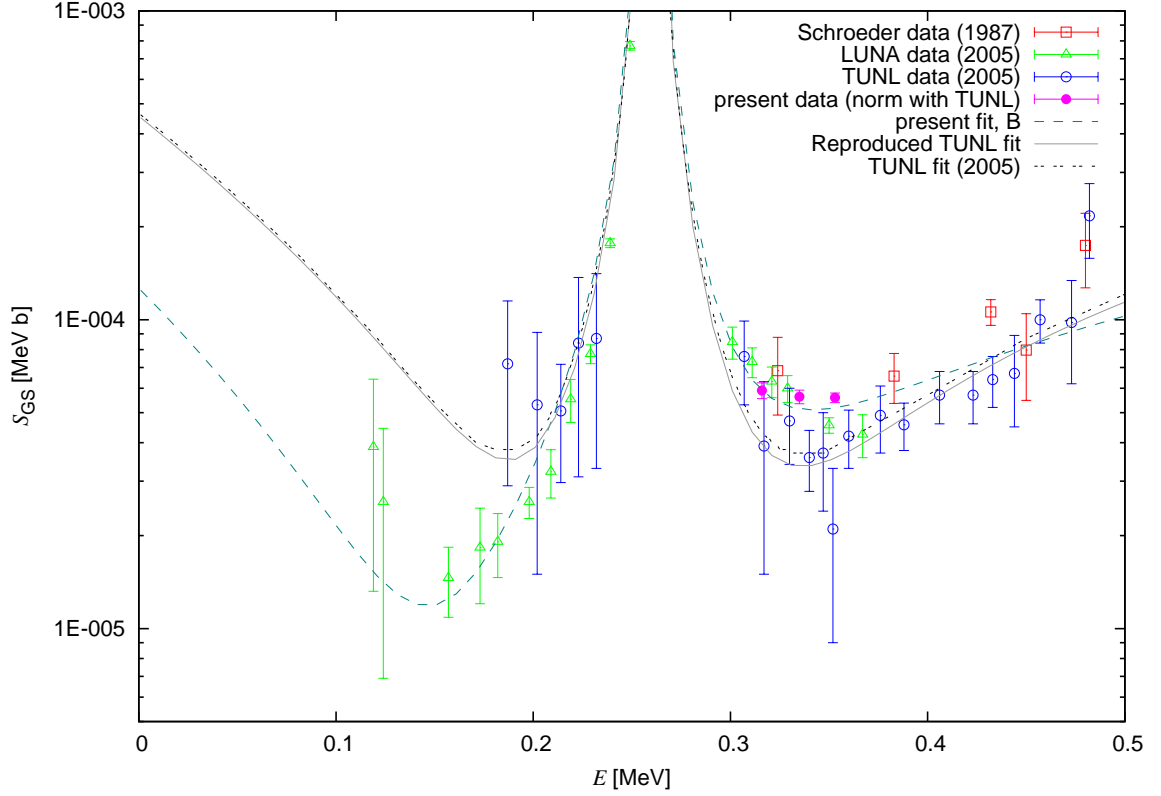


Figure 4.1: Influence of present data on the TUNL R-matrix fit. The Original TUNL fit and the one reproduced with the present code are shown as well.

The test of adding the present three data points has been applied also with the **LUNA fit**. The input parameters ANC, poles at  $E = 0.259, 0.985, 2.187$  MeV and reduced width of the background pole were taken unchanged from the previous LUNA fit [36]. Just as in the previous fit, the data from LUNA 2005[36, 35] and the Schröder data [38] corrected for summing [36] have been used. The obtained extrapolated  $S_{GS}(0) = 0.24$  (fig. 4.2) is only slightly lower from the previous LUNA result  $0.25 \pm 0.06$  keV b. This is no surprise because the present data are only three and their smaller errors cannot constrain the fit too much, because the other data in the same energy region do not have much larger error bars, as is the case for the TUNL data set.

One should not forget that those literature data have been obtained after a large summing-in correction and their quoted uncertainties does not seem to always reflect this fact, as pointed out in section 1.4. There, it is estimated that a more realistic error should be at least 10% of the correction applied (tab. 1.5). If the literature uncertainties were to be changed accordingly, the data would not have this major contribution on the  $\chi^2$ .

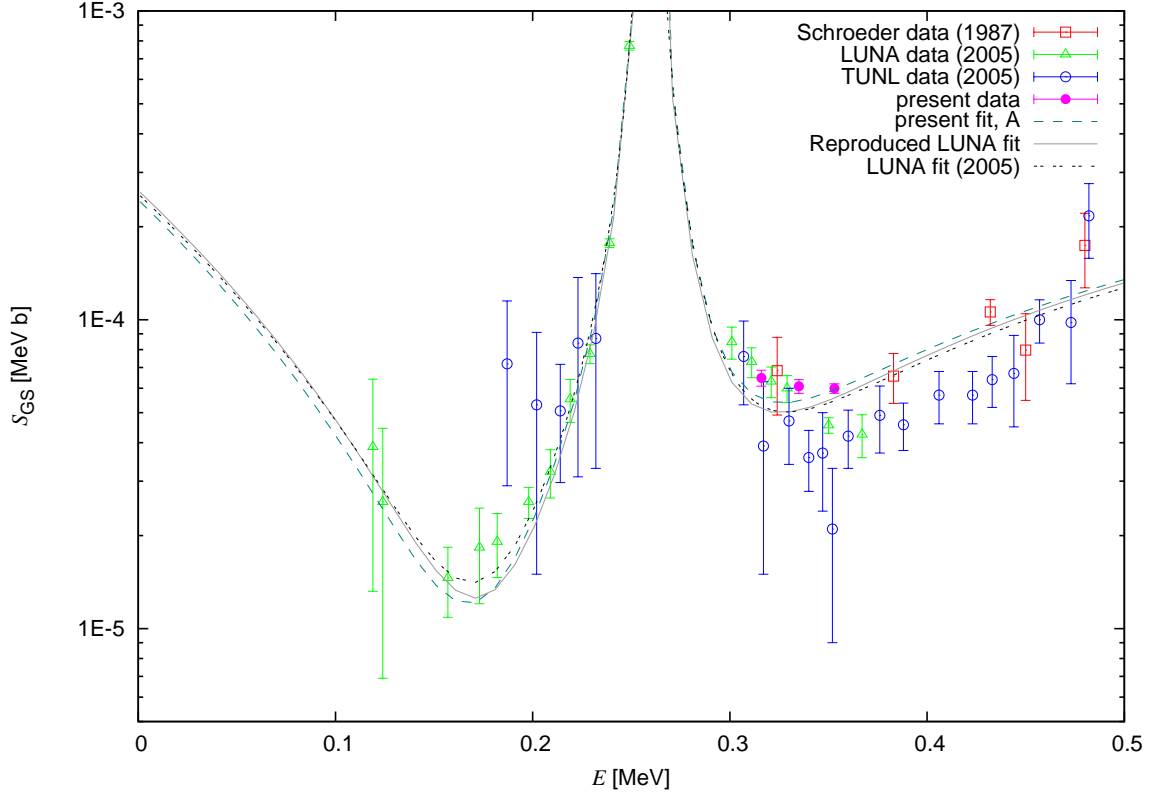


Figure 4.2: Influence of present data on the LUNA 2005 R-matrix fit. The original LUNA 2005 fit and the one reproduced with the present code are shown as well.

### 4.3 New R-matrix fit for capture to the ground state

For the present new fit it was decided not to include all data affected by summing-in larger than 50%, in order to obtain a result for extrapolated S-factor where problems due to that correction could be excluded. With the exclusion of TUNL and LUNA 2005 results, also data points below the resonance that would have been very useful can not be considered.

The only data sets considered are the higher-energy data (summing corrected [36]) of Schröder et al. [38] and the present S-factors from the relative analysis (tab. 2.21). For the strength of the 259 keV resonance, 13.1 meV (weighted average of [37, 35, 54, 91]) was adopted, and for the ground state branching, 1.6% (weighted average of [37, 35] and the present work) was used. The interference pattern around the 259 keV resonance is fixed by the results of [36, 37, 35], and the interaction radius was set to 5.5 fm [36].

The best fit (fig. 4.3) varying only the  $\gamma$ -widths of the subthreshold state and of the background pole results in  $S_{\text{GS}}(0) = 0.20 \text{ keV barn}$  with a  $\gamma$ -width  $\Gamma_\gamma = 0.9 \pm 0.2 \text{ eV}$  for the subthreshold state, in agreement with Coulomb excitation work [44] and with lifetime measurements [42, 43]. A full R-matrix analysis including a detailed error determination for all parameters is beyond the scope of the present work. Therefore, the previous relative

uncertainty of 24% in  $S_{\text{GS}}(0)$  [36] is adopted here, giving  $S_{\text{GS}}(0) = 0.20 \pm 0.05$  keV barn, in good agreement with the previous LUNA value [36, 35].

The latest fit SF2 from the review [31] considers the data sets by (summing-in corrected) Schröder [38], LUNA 2005 [36, 35], TUNL [37] renormalized (by 2-6%) considering their results for the 259 keV  $\omega\gamma$  with respect to the average 13.1 meV [31]. The present data (LUNA 2008) [72] from the analysis relative to the 6.79 S-factor have also been included in the fit. The extrapolated value is  $S_{\text{GS}}(0) = 0.27 \pm 0.05$  keV b with  $\Gamma_\gamma = 1.1$  eV, in agreement with the present value but higher, mainly because of the inclusion of all available data sets. Notice also that this fit does not consider the resonances at  $E = 0.987$  and  $2.19$  MeV (fig. 4.3, bottom panel) and that could be yet another reason for the different extrapolated S-factor.

The ground state capture now contributes less than 4% uncertainty to the total  $S_{\text{tot}}(0)$ , instead of the previous 15%. On the basis of the present result,  $S_{\text{tot}}(0) = 1.57 \pm 0.13$  keV barn is recommended, with the uncertainty including also systematic effects. For this sum,  $S_{6172}(0) = 0.09 \pm 0.07$  keV barn has been adopted based on the results by [49, 46, 37, 35], while the other contributions are as given in LUNA 2005 [35].

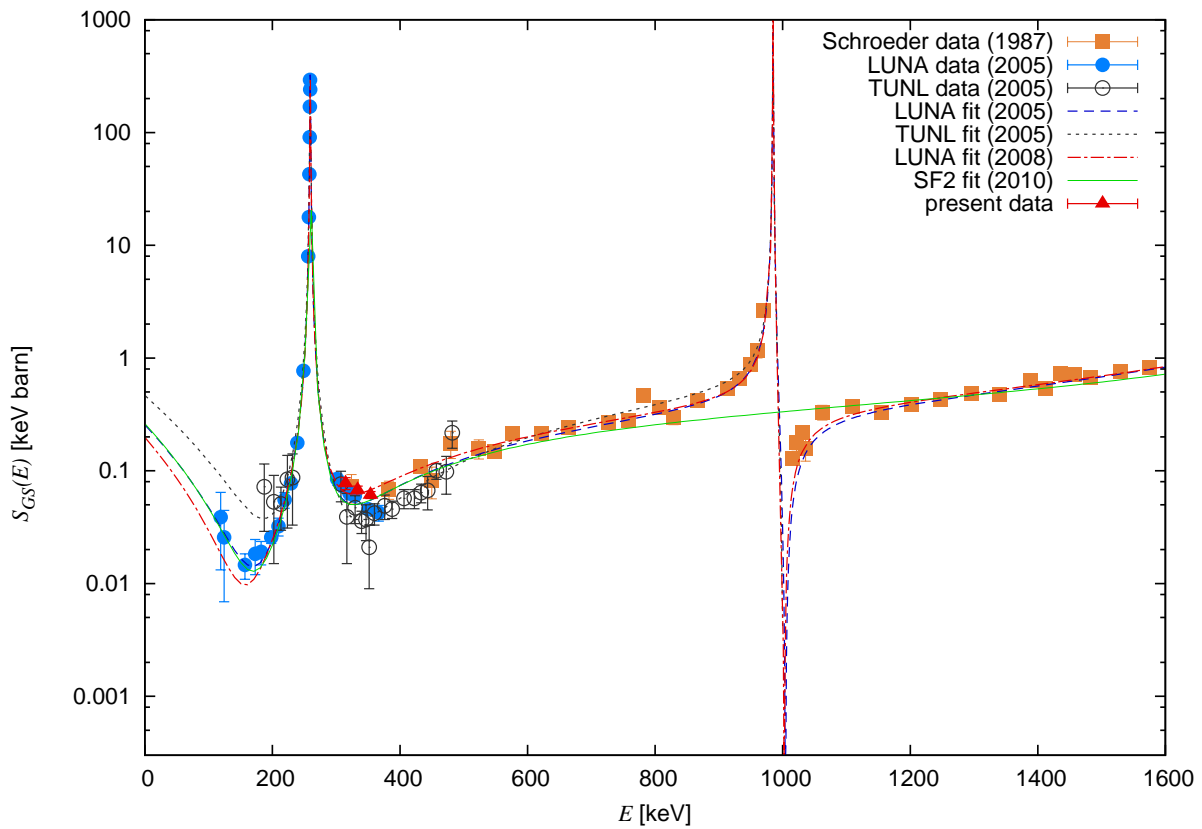
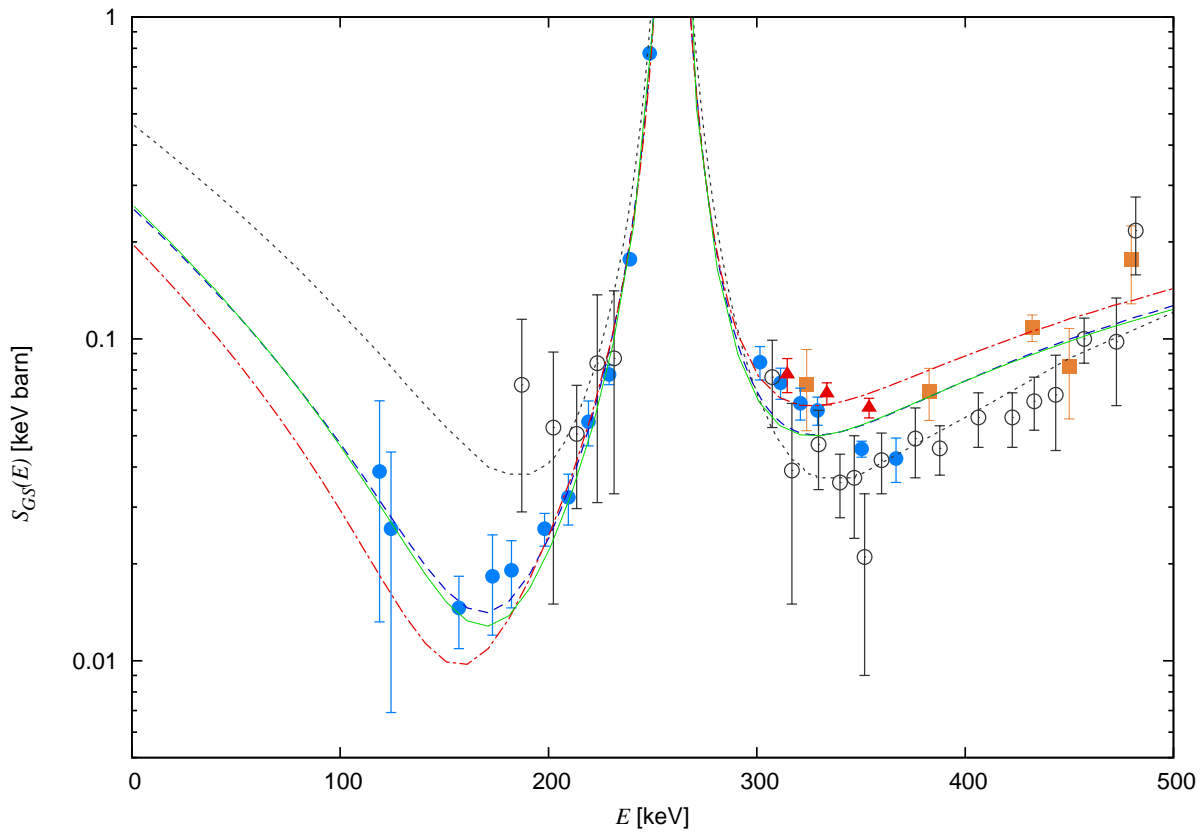


Figure 4.3: Present R-matrix fit LUNA 2008, compared to previous TUNL, LUNA 2005 and the recent SF2 (Solar Fusion 2 workshop [31]).

# Summary and Outlook

The reaction  $^{14}\text{N}(p,\gamma)^{15}\text{O}$  has been studied in the low and the high-energy domains, in two different experiments. Three data points at energy  $E_p = 0.36, 0.38, 0.40$  MeV have been obtained in the underground facility LUNA. Using a Clover composite detector, the cross section for capture to the ground state has been studied with strongly reduced true coincidence summing-in effect. The data have been obtained as ratios of cross sections, relative to the well-studied capture to the 6792 keV excited state in  $^{15}\text{O}$ . A new R-matrix fit has been performed, based only on data sets that are only weakly affected by the summing correction. The result solved a previous factor of two discrepancy for this transition, ruling out the TUNL extrapolated S-factor in favor of the LUNA 2005 one.

Cross section data for transitions to the excited states in  $^{15}\text{O}$  have also been obtained, with a different method based on target information, beam current and detection efficiency. Larger systematic uncertainties than the relative data had to be included in the final results. The new S-factors provide an additional independent data set with competitive uncertainties.

More precise branching ratios on the 259 keV resonance have been obtained, with unprecedented low summing correction.

The high-energy range  $E_p = 0.6 - 2$  MeV has been studied at the 3 MV Tandetron in Dresden with four HPGe detectors surrounding the target chamber, enabling also angular correlation studies for two resonances in the  $^{14}\text{N}(p,\gamma)^{15}\text{O}$  reaction and another two in the  $^{15}\text{N}(p,\alpha\gamma)^{12}\text{C}$  reaction. The isotropy of  $\gamma$ -rays emitted on the 259 keV resonance was confirmed. The angular distribution on the  $E_p = 1058$  keV has been checked within 3%. The strong anisotropy measured in literature was confirmed for the  $^{15}\text{N}(p,\alpha\gamma)^{12}\text{C}$  resonances at  $E_p = 430$  and 897 keV.

The strengths  $\omega\gamma$  of three resonances have been measured relative to the well-known  $^{14}\text{N}(p,\gamma)^{15}\text{O}$  resonance at  $E = 259$  keV, improving the precision. The  $E_p = 430$  keV resonance in  $^{15}\text{N}(p,\alpha\gamma)^{12}\text{C}$  also studied here is used in inverse kinematics for hydrogen depth profiling.

For the  $E_p = 1058$  keV resonance in  $^{14}\text{N}(p,\gamma)^{15}\text{O}$ , the branching ratios have been measured. They point out a possible problem in the previous compilation, which is based on one experiment using low-resolution detectors.

The present results have been included in all the recent reviews of the field [92, 93, 94,

31], and they have been used in a stellar network [95]. The new recommended S-factor is included in the recently updated solar model [14].

Possible further improvements on the precision of the  $^{14}\text{N}(p,\gamma)^{15}\text{O}$  reaction at astrophysical energies may be obtained by remeasuring the 259 keV resonance strength, because of its importance as a reference for other data. A measurement of the  $\gamma$ -width of the subthreshold resonance at  $E_x = 6792$  keV may also help in fixing free parameters in the R-matrix framework.

However, the improvement depends not only on experimental studies, but also on reliable ways to extrapolate the data. An alternative to the R-matrix framework is an ab initio theoretical calculation that does not depend on experimental data. That has been done very recently [96] for the  $^3\text{He}(^4\text{He},\gamma)^7\text{Be}$  reaction. With future improvements in computer facilities, it may be possible to extend this approach to higher masses.



# Appendix A

## Angular correlation

The  $\gamma$ -rays following a radioactive decay or a nuclear reaction are in general not isotropically emitted. In the usual case, a correlation exists between the direction of a photon and the one of the beam or the photon belonging to the same physical cascade. It is referred to the two emissions involved as entrance and exit channel. The probability of the exit-channel photon being emitted at one angle  $\theta$  with respect to the direction of the entrance-channel photon (or particle) is expressed as a sum of Legendre polynomials  $P^L(x)$ :

$$W(\theta) = 1 + a_2 Q_2 P_2^L(\cos(\theta)) + a_4 Q_4 P_4^L(\cos(\theta)) + \dots \quad (\text{A.1})$$

where  $\theta$  is the detection angle with respect to the beam direction,  $a$  are parameters, and  $Q$  the attenuation factors due to finite detection solid angle [85], that depends on the size of detectors and their distance from the point of emission of the photons. The detection angle  $\theta$  in center of mass frame can be approximated<sup>1</sup> with the one in the laboratory frame, if the reactions occurring at very low incident energy on target heavier than the projectile as in the present work. The function in (A.1) satisfies the normalization condition:

$$\int_{\Omega} W(\theta) d\Omega \stackrel{!}{=} 4\pi; \quad \int_0^\pi W(\theta) 2\pi \sin(\theta) d\theta \stackrel{!}{=} 4\pi$$

If we imagine to collect all the events with a surrounding detector covering the whole solid angle, the resulting number should not be different from the sum of the counts from many smaller detectors at different angles, each corrected for the angular distribution at that angle.

The  $\rho^{\gamma\gamma}$  in section 2.6.1 was obtained by finding the parameter  $a_2$  in the following expression of the angular correlation,

$$W(\theta) = 1 + a_2 Q_2 P_2^L(\cos(\theta)) \quad (\text{A.2})$$

that satisfies the experimental values found by [53]:

$$\frac{W(180^\circ)}{W(90^\circ)} = \frac{I(180^\circ)}{I(90^\circ)}. \quad (\text{A.3})$$

---

<sup>1</sup>the difference is  $< 0.2\%$  for the present radiative reaction if  $E_p < 400$  keV

transition	$j_1$	$L_1, L'_1$	$J$	$L_2, L'_2$	$j_2$	$\delta_1$	$\delta_2$	$a_2$
6.79		M1, E2	$\frac{3}{2}^+$	E1 (M2)		-0.08	0	0.18
6.17	$\frac{1}{2}^+$	E1 (M2)	$\frac{3}{2}^-$	M1, E2	$\frac{1}{2}^-$	0	-0.12	0.14
5.18		E1	$\frac{1}{2}^-$	M1		0	0	0

Table A.1: Adopted values for the theoretical calculation of the pairwise angular correlation of the three physical cascade through the 6792, 6172 and 5181 keV excited states in  $^{15}\text{O}$ , on the 259 keV resonance. The multipolarity M2 is negligible with respect to E1 and is not considered. The results obtained for  $a_2$  in the last column.

The attenuation factor  $Q_2$  was 0.71 for the setup in [53] and 0.74 for the experiment performed at LUNA. The results for  $a_2$  corresponding to the transitions 6.79, 6.17, 5.18 are respectively 0.1765, 0.147, 0.009. The angular correlation of the 5.18-cascade  $\gamma$ -rays is isotropic within the uncertainty.

The parameters  $a_2$  have been obtained also with an independent theoretical method. Because the correlation involves an intermediate state  $J$  of well defined parity, it was possible to calculate the angular correlation between cascade  $\gamma$ -rays in a straightforward way based on the spin and parity of nuclear states involved [2, p. 606].

In the two-step process, an intermediate state of spin  $J$  is formed from an initial state of spin  $j_1$  via the absorption or emission of a photon of  $L_1$  or  $L'_1$  angular momentum (multipolarity). The same terminology is used for the exit channel, with identifier 2. The parameters  $a_n$  in eq. (A.1) in case of two possible multiplicities (with  $L_i < L'_i$ ) for the radiation in the entrance or exit channel are given by:

$$a_n = [F_n(L_1, L_1, j_1, J) + 2\delta_1 F_n(L_1, L'_1, j_1, J) + \delta_1^2 F_n(L'_1, L'_1, j_1, J)] \cdot [F_n(L_2, L_2, j_2, J) + 2\delta_2 F_n(L_2, L'_2, j_2, J) + \delta_2^2 F_n(L'_2, L'_2, j_2, J)] \quad (\text{A.4})$$

where  $\delta_i$  are the  $\gamma$ -ray multipolarity mixing ratios,  $F_n(L_i, L_i, j_i, J)$  are tabulated [97, p. 199] values that depend in turn on Clebsch-Gordan and Racah coefficients [98].  $\delta_i = 0$  if only one multipolarity  $L_i$  is possible or it is much more probable than the higher order one  $L'_i$ . The adopted values and results obtained on resonance are shown in table A.1. The initial and final state are the level at  $E_x = 7556$  keV and the ground state in  $^{15}\text{O}$ , for all transitions. The distribution in the 5.18 case is by definition isotropic because the intermediate state  $J$  has spin 1/2.

In the off-resonance case, the calculation was performed considering the entrance channel as a virtual state with spin and parity given by the possible combinations of projectile and target nucleus parities and spins. Due to the low interaction energy, only the case  $l = 0$  for the angular momentum of the proton was considered. Thus, two possible values for the initial state  $j_1$  can be formed:  $1/2^+$  and  $3/2^+$ . The first case corresponds to the on-resonance case already discussed. The same procedure was applied in the other case separately, obtaining the results  $a_2(3/2)$  of table A.2. The final  $a_2$  is obtained by

transition	$j_1$	$L_1, L'_1$	$J$	$L_2, L'_2$	$j_2$	$\delta_1$	$\delta_2$	$a_2(\frac{3}{2})$	$a_2$
6.79		M1, E2 (M3)	$\frac{3}{2}^+$	E1 (M2)		-0.08	0	-0.26	-0.11
6.17	$\frac{3}{2}^+$	E1 (M2, E3)	$\frac{3}{2}^-$	M1, E2	$\frac{1}{2}^-$	0	-0.12	-0.11	-0.03
5.18		E1 (M2)	$\frac{1}{2}^-$	M1		0	0	0	0

Table A.2: Adopted values for the theoretical calculation of the pairwise angular correlation of the three physical cascade through the 6792, 6172 and 5181 keV excited states in  $^{15}\text{O}$ , off resonance. The multiplicities M2, E2 and M3 are negligible and are not considered. The results for the initial state  $3/2^+$  are in the one but last column. These values are combined with the ones in the previous table to give the  $a_2$  for angular correlation off resonance, in the last column.

summing these and the results from table A.1, weighted with the probability to form the initial state  $3/2^+$  or  $1/2^+$ , respectively  $4/6$  and  $2/6$ .



# Bibliography

- [1] C. Rolfs and W. Rodney. *Cauldrons in the Cosmos*. University of Chicago Press, Chicago (1988)
- [2] C. Iliadis. *Nuclear Physics of Stars*. Wiley-VCH (2007)
- [3] C.-F. von Weizsäcker. *Über Elementumwandlungen im Innern der Sterne. II*. *Physikalische Zeitschrift* **39**, 633–646 (1938)
- [4] H. Bethe. *Energy production in stars*. *Phys. Rev.* **55**, 434–456 (1939)
- [5] F. Herwig, S. M. Austin, and J. C. Lattanzio. *Nuclear reaction rate uncertainties and astrophysical modeling: Carbon yields from low-mass giants*. *Phys. Rev. C* **73**, 025802 (2006)
- [6] L. M. Krauss and B. Chaboyer. *Age Estimates of Globular Clusters in the Milky Way: Constraints on Cosmology*. *Science* **299**, 65–70 (2003)
- [7] G. Imbriani et al. *The bottleneck of CNO burning and the age of Globular Clusters*. *Astron. Astrophys.* **420**, 625–629 (2004)
- [8] E. Degl’Innocenti et al. *The  $^{14}\text{N}(p,\gamma)^{15}\text{O}$  reaction, solar neutrinos and the age of globular clusters*. *Phys. Lett. B* **590**, 13–20 (2004)
- [9] J. N. Bahcall, A. M. Serenelli, and S. Basu. *10,000 Standard Solar Models: A Monte Carlo Simulation*. *Astrophys. J. Suppl. Ser.* **165**, 400–431 (2006)
- [10] A. Caciolli. *Underground study of  $^{15}\text{N}(p,\gamma)^{16}\text{O}$  at stellar energies*. Ph.D. thesis, Università degli studi di Padova (2010)
- [11] Y. Amelin, A. N. Krot, I. D. Hutcheon, and A. A. Ulyanov. *Lead Isotopic Ages of Chondrules and Calcium-Aluminum-Rich Inclusions*. *Science* **297**, 1678–1683 (2002)
- [12] J. Baker, et al. *Early planetesimal melting from an age of 4.5662 Gyr for differentiated meteorites*. *Nature* **436**, 1127–1131 (2005)
- [13] J. N. Bahcall, A. M. Serenelli, and S. Basu. *New Solar Opacities, Abundances, Helioseismology, and Neutrino Fluxes*. *Astrophys. J.* **621**, L85–L88 (2005)

- [14] A. M. Serenelli, S. Basu, J. W. Ferguson, and M. Asplund. *New Solar Composition: The Problem with Solar Models Revisited*. *Astrophys. J. Lett.* **705**, L123–L127 (2009)
- [15] R. Davis, D. S. Harmer, and K. C. Hoffman. *Search for Neutrinos from the Sun*. *Phys. Rev. Lett.* **20**, 1205–1209 (1968)
- [16] G. Bellini, et al. *Measurement of the solar  $^8\text{B}$  neutrino rate with a liquid scintillator target and 3 MeV energy threshold in the Borexino detector*. *Phys. Rev. D* **82**, 033006 (2010)
- [17] C. Arpesella, et al. *Direct Measurement of the  $^7\text{Be}$  Solar Neutrino Flux with 192 Days of Borexino Data*. *Phys. Rev. Lett.* **101**, 091302 (2008)
- [18] J. Hosaka et al. *Solar neutrino measurements in Super-Kamiokande-I*. *Phys. Rev. D* **73**, 112001 (2006)
- [19] Q. R. Ahmad, et al. *Measurement of Day and Night Neutrino Energy Spectra at SNO and Constraints on Neutrino Mixing Parameters*. *Phys. Rev. Lett.* **89**, 011302 (2002)
- [20] F. Hill, et al. *The Solar Acoustic Spectrum and Eigenmode Parameters*. *Science* **272**, 1292–1295 (1996)
- [21] P. H. Scherrer, et al. *The Solar Oscillations Investigation - Michelson Doppler Imager*. *Solar Physics* **162**, 129–188 (1995)
- [22] S. Basu and H. M. Antia. *Helioseismology and solar abundances*. *Phys. Rep.* **457**, 217–283 (2008)
- [23] S. Basu. *Helioseismology as a diagnostic of the solar interior*. *Astrophys. Space Sci.* **328**, 43–50 (2010)
- [24] M. Asplund, N. Grevesse, A. J. Sauval, and P. Scott. *The Chemical Composition of the Sun*. *Ann. Rev. Astron. Astroph.* **47**, 481–522 (2009)
- [25] N. Grevesse, M. Asplund, A. Sauval, and P. Scott. *The chemical composition of the Sun*. *Astrophys. Space Sci.* **328**, 179–183 (2010). ISSN 0004-640X
- [26] N. Grevesse and A. J. Sauval. *Standard Solar Composition*. *Space Sci. Rev.* **85**, 161–174 (1998). ISSN 0038-6308
- [27] W. C. Haxton and A. M. Serenelli. *CN-Cycle Solar Neutrinos and Sun's Primordial Core Metalicity*. *Astrophys. J.* **687**, 678–691 (2008)
- [28] A. Ianni. *Understanding the sun: Borexino*. *Journal of Physics: Conference Series* **202**, 012028 (2010)

- [29] B. Aharmim, et al. *Independent Measurement of the Total Active  $^8\text{B}$  Solar Neutrino Flux Using an Array of  $^3\text{He}$  Proportional Counters at the Sudbury Neutrino Observatory.* Phys. Rev. Lett. **101**, 111301 (2008)
- [30] S. Abe, et al. *Precision Measurement of Neutrino Oscillation Parameters with KamLAND.* Phys. Rev. Lett. **100**, 221803 (2008)
- [31] E. Adelberger et al. *Solar fusion cross sections II. The pp chain and CNO cycles.* Rev. Mod. Phys. **83**, 195–245 (2011)
- [32] M. C. Chen. *The SNO Liquid Scintillator Project.* Nucl. Phys. B (Proc. Suppl.) **145**, 65–68 (2005)
- [33] E. M. Burbidge, G. R. Burbidge, W. A. Fowler, and F. Hoyle. *Synthesis of the Elements in Stars.* Rev. Mod. Phys. **29**, 547–650 (1957)
- [34] F. Ajzenberg-Selove. *Energy levels of light nuclei  $A = 13-15$ .* Nucl. Phys. A **523**, 1–196 (1991)
- [35] G. Imbriani et al. *S-factor of  $^{14}\text{N}(p,\gamma)^{15}\text{O}$  at astrophysical energies.* Eur. Phys. J. A **25**, 455–466 (2005)
- [36] A. Formicola et al. *Astrophysical S-factor of  $^{14}\text{N}(p,\gamma)^{15}\text{O}$ .* Phys. Lett. B **591**, 61–68 (2004)
- [37] R. C. Runkle et al. *Direct Measurement of the  $^{14}\text{N}(p,\gamma)^{15}\text{O}$  S Factor.* Phys. Rev. Lett. **94**, 082503 (2005)
- [38] U. Schröder et al. *Stellar reaction rate of  $^{14}\text{N}(p,\gamma)^{15}\text{O}$  and hydrogen burning in massive stars.* Nucl. Phys. A **467**, 240–260 (1987)
- [39] E. Adelberger et al. *Solar fusion cross sections.* Rev. Mod. Phys. **70**, 1265–1291 (1998)
- [40] G. Caughlan and W. Fowler. *Thermonuclear Reaction Rates V.* At. Data Nucl. Data Tables **40**, 283–334 (1988)
- [41] C. Angulo et al. *A compilation of charged-particle induced thermonuclear reaction rates.* Nucl. Phys. A **656**, 3–187 (1999)
- [42] P. Bertone et al. *Lifetime of the 6793-keV state in  $^{15}\text{O}$ .* Phys. Rev. Lett. **87**, 152501 (2001)
- [43] D. Schürmann et al. *Lifetime measurement of the 6792 keV state in  $^{15}\text{O}$ , important for the astrophysical S factor extrapolation in  $^{14}\text{N}(p,\gamma)^{15}\text{O}$ .* Phys. Rev. C **77**, 055803 (2008)

- [44] K. Yamada et al. *E1 strength of the subthreshold  $3/2^+$  state in  $^{15}\text{O}$  studied by Coulomb excitation.* Phys. Lett. B **579**, 265–270 (2004)
- [45] C. Angulo and P. Descouvemont. *The  $^{14}\text{N}(p,\gamma)^{15}\text{O}$  low-energy  $S$ -factor.* Nucl. Phys. A **690**, 755–768 (2001)
- [46] A. Mukhamedzhanov et al. *Asymptotic normalization coefficients for  $^{14}\text{N}+p \rightarrow ^{15}\text{O}$  and the astrophysical  $S$  factor for  $^{14}\text{N}(p,\gamma)^{15}\text{O}$ .* Phys. Rev. C **67**, 065804 (2003)
- [47] P. F. Bertone et al.  *$^{14}\text{N}(\beta\text{He},d)^{15}\text{O}$  as a probe of direct capture in the  $^{14}\text{N}(p,\gamma)^{15}\text{O}$  reaction.* Phys. Rev. C **66**, 055804 (2002)
- [48] D. Spergel et al. *First-Year Wilkinson Microwave Anisotropy Probe (WMAP) Observations: Determination of Cosmological Parameters.* Astrophys. J. Suppl. Ser. **148**, 175–194 (2003)
- [49] S. O. Nelson et al. *Analyzing power measurement for the  $^{14}\text{N}(\vec{p},\gamma)^{15}\text{O}$  reaction at astrophysically relevant energies.* Phys. Rev. C **68**, 065804 (2003)
- [50] D. Güttler. *An Investigation of Target Poisoning during Reactive Magnetron Sputtering.* Ph.D. thesis, Technische Universität Dresden (2009). FZD Report FZD-515
- [51] H. Costantini. *Direct measurements of radiative capture reactions at astrophysical energies.* Ph.D. thesis, Università degli studi di Genova (2003)
- [52] A. Formicola. *A new study of  $^{14}\text{N}(p,\gamma)^{15}\text{O}$  at low energy.* Ph.D. thesis, Ruhr-Universität Bochum (2004)
- [53] B. Povh and D. F. Hebbard. *Angular Correlation Measurements in  $^{15}\text{O}$ .* Phys. Rev. **115**, 608–613 (1959)
- [54] A. Lemut et al. *First measurement of the  $^{14}\text{N}(p,\gamma)^{15}\text{O}$  cross section down to 70 keV.* Phys. Lett. B **634**, 483 (2006)
- [55] D. Bemmerer et al. *Low energy measurement of the  $^{14}\text{N}(p,\gamma)^{15}\text{O}$  total cross section at the LUNA underground facility.* Nucl. Phys. A **779**, 297–317 (2006)
- [56] D. Bemmerer et al. *Feasibility of low-energy radiative-capture experiments at the LUNA underground accelerator facility.* Eur. Phys. J. A **24**, 313–319 (2005)
- [57] S. P. Ahlen et al. *Study of penetrating cosmic ray muons and search for large scale anisotropies at the Gran Sasso Laboratory.* Phys. Lett. B **249**, 149–156 (1990)
- [58] T. Szücs, et al. *An actively vetoed Clover  $\gamma$ -detector for nuclear astrophysics at LUNA.* European Physical Journal A **44**, 513–519 (2010)



- [59] A. Formicola et al. *The LUNA II 400 kV accelerator*. Nucl. Inst. Meth. A **507**, 609–616 (2003)
- [60] J. Ziegler. *SRIM version 2008.02* (2008). Software SRIM, Stopping and Range of Ions in Matter
- [61] Eurisys Mesures. *Clover Detector Manual*. Lingolsheim (1998)
- [62] G. Duchêne et al. *The Clover: a new generation of composite Ge detectors*. Nucl. Inst. Meth. A **432**, 90 (1999)
- [63] Z. Elekes et al. *Absolute full-energy peak efficiency calibration of a Clover-BGO detector system*. Nucl. Inst. Meth. A **503**, 580–588 (2003)
- [64] *Hardware manual: model 919E, Multichannel Buffer*. Ortec (2002)
- [65] R. Schwengner, et al. *The photon-scattering facility at the superconducting electron accelerator ELBE*. Nucl. Inst. Meth. A **555**, 211 – 219 (2005). ISSN 0168-9002
- [66] G. Gilmore. *Practical  $\gamma$ -ray spectrometry, 2nd edition*. John Wiley and Sons, New York (2008)
- [67] Brookhaven National Laboratory, National Nuclear Data Center. *Nuclear Structure and Decay Databases*. <http://www.nndc.bnl.gov>
- [68] G. Musiol, J. Ranft, R. Reif, and D. Seeliger. *Kern- und Elementarteilchenphysik*. VCH Weinheim (1988)
- [69] National Institute of Standards and Technology. *Tables and graphs of the photon mass attenuation coefficient*. <http://www.nist.gov/pml/data/xraycoef/index.cfm>
- [70] T. Tabata and K. Okano. *Gamma-rays from the 7.56 MeV level in O-15*. J. Phys. Soc. Japan **15**, 1552–1555 (1960)
- [71] D. F. Hebbard and G. M. Bailey. *Non-resonant radiation from the  $^{14}\text{N}(p,\gamma)$  reaction (II)*. Nucl. Phys. **49**, 666–685 (1963)
- [72] M. Marta et al. *Precision study of ground state capture in the  $^{14}\text{N}(p,\gamma)^{15}\text{O}$  reaction*. Phys. Rev. C **78**, 022802(R) (2008)
- [73] M. Friedrich, W. Bürger, D. Henke, and S. Turuc. *The Rossendorf 3 MV tandetron: a new generation of high-energy implanters*. Nucl. Inst. Meth. A **382**, 357–360 (1996)
- [74] E. Trompler. *Messung des Wirkungsquerschnitts astrophysikalisch relevanter Kernreaktionen*. Master’s thesis, Technische Universität Dresden (2009). FZD Report FZD-523

- [75] T. B. Coplen et al. *Isotope-abundance variations of selected elements (IUPAC Technical Report)*. Pure Appl. Chem. **74**, 1987–2017 (2002)
- [76] A. Mariotti. *Atmospheric nitrogen is a reliable standard for natural  $^{15}\text{N}$  abundance measurements*. Nature **303**, 685–687 (1983)
- [77] D. Bemmerer et al. *Direct measurement of the  $^{15}\text{N}(p,\gamma)^{16}\text{O}$  cross section at novae energies*. J. Phys. G **36**, 0452002 (2009)
- [78] D. Tilley, H. Weller, and C. Cheves. *Energy levels of light nuclei  $A = 16-17$* . Nucl. Phys. A **564**, 1–183 (1993)
- [79] F. Zijderhand, F. P. Jansen, C. Alderliesten, and C. van der Leun. *Detector-efficiency calibration for high-energy gamma-rays*. Nucl. Inst. Meth. A **286**, 490 – 496 (1990). ISSN 0168-9002
- [80] A. Anttila, J. Keinonen, M. Hautala, and I. Forsblom. *Use of the  $^{27}\text{Al}(p,\gamma)^{28}\text{Si}$ ,  $E_p = 992\text{ keV}$  resonance as a gamma-ray intensity standard*. Nucl. Inst. Meth. **147**, 501 – 505 (1977). ISSN 0029-554X
- [81] A. E. Evans, B. Brown, and J. B. Marion. *Study of the  $^{14}\text{N}(p,\gamma)^{15}\text{O}$  Reaction*. Phys. Rev. **149**, 863–879 (1966)
- [82] L. S. Wielunski, et al. *Hydrogen depth resolution in multilayer metal structures, comparison of elastic recoil detection and resonant nuclear reaction method*. Nucl. Inst. Meth. B **190**, 693–698 (2002). ISSN 0168-583X
- [83] H. Becker et al. *Hydrogen depth profiling using  $^{18}\text{O}$  ions*. Z. Phys. A **351**, 453–465 (1995)
- [84] A. A. Kraus, A. P. French, W. A. Fowler, and C. C. Lauritsen. *Angular Distribution of Gamma-Rays and Short-Range Alpha-Particles from  $^{15}\text{N}(p, \alpha\gamma)^{12}\text{C}$* . Phys. Rev. **89**, 299–301 (1953)
- [85] M. E. Rose. *The analysis of angular correlation and angular distribution data*. Phys. Rev. **91**, 610–615 (1953)
- [86] G. Junk and H. Svec. *The absolute abundance of the nitrogen isotopes in the atmosphere and compressed gas from various sources*. Geochim. Cosmochim. Acta **14**, 234–243 (1958)
- [87] J. F. Ziegler, J. P. Biersack, and M. D. Ziegler. *SRIM. The Stopping and Range of Ions in Matter*. SRIM Co., Chester, Maryland (2008)
- [88] F. Zijderhand and C. van der Leun. *Strong  $M2$  transitions*. Nucl. Phys. A **460**, 181–200 (1986)

- [89] A. M. Lane and R. G. Thomas. *R-matrix theory of nuclear reactions*. Rev. Mod. Phys. **30**, 257–353 (1958)
- [90] R. E. Azuma, et al. *AZURE: An R-matrix code for nuclear astrophysics*. Phys. Rev. C **81**, 045805 (2010)
- [91] F. Ajzenberg-Selove. *Energy levels of light nuclei a = 13-15*. Nucl. Phys. A **523**, 1–196 (1991)
- [92] H. Costantini et al. *LUNA: a laboratory for underground nuclear astrophysics*. Rep. Prog. Phys. **72**, 086301 (2009)
- [93] C. Broggini, D. Bemmerer, A. Guglielmetti, and R. Menegazzo. *LUNA: Nuclear Astrophysics Deep Underground*. Annu. Rev. Nucl. Part. Sci. **60**, 53–73 (2010)
- [94] M. Wiescher, et al. *The Cold and Hot CNO Cycles*. Annu. Rev. Nucl. Part. Sci. **60**, 381–404 (2010)
- [95] S. Palmerini, M. L. Cognata, S. Cristallo, and M. Busso. *Deep Mixing in Evolved Stars: I. The Effect of Reaction Rate Revisions from C to Al*. Astrophys. J. **729**, 3 (2011)
- [96] T. Neff. *Microscopic calculation of the  ${}^3\text{He}(\alpha,\gamma){}^7\text{Be}$  and  ${}^3\text{H}(\alpha,\gamma){}^7\text{Li}$  capture cross sections using realistic interactions*. Phys. Rev. Lett. **106**, 042502 (2011)
- [97] R. D. Gill. *Gamma-ray angular correlations*. Academic Press, London (1975). ISBN 0-12-283850-5
- [98] L. C. Biedenharn and M. E. Rose. *Theory of Angular Correlation of Nuclear Radiations*. Rev. Mod. Phys. **25**, 729–777 (1953)



# Acknowledgements

I would like to thank all the people that directly or indirectly made my doctoral experience, and consequently this work, possible, enriching and pleasant.

I am grateful to Prof. Eckart Grosse for being my Doktorvater and for the opportunity of working in this institute as a Ph.D. student, thus allowing me to continue with the research started during the master's degree. For similar reasons, I'm indebted with Prof. Thomas Cowan and I would like to thank him very much. Special thanks to Dr. Daniel Bemmerer with whom I shared these four years, for his constant support, advices, and all the things I learned from him. And also for the relaxed atmosphere in the office! Many thanks to Dr. Zsolt Fülöp who will be a referee for this work.

I'm particularly thankful to Dr. Zoltan Elekes for providing the GEANT4 simulations for the Clover detector, to Dr. Hanns-Peter Trautvetter for the discussion on the analysis (and for hosting me), to Erik Trompler for his contribution on the detection efficiencies at the Tandatron experiment, to Dr. P. Descouvemont (ULB Brussels) for the R-matrix code.

I would like to thank all the colleagues from the LUNA collaboration, the people at the FZ...I mean HZDR, and the colleagues at ATOMKI, who actively participated in the experiments described in this work.

I do not forget Alessandra and Roberto Bonetti who welcomed me at the very beginning in LUNA even though I'm a nuclear engineer, Alba per l'aceto balsamico e il turpiloquio, Antonio perché è un amico. Olive juice to all the people who are able to make me feel at home. And  
Vielen Dank Blechlawine!

The song "Wipe out" by the Surfariis and its drum solo are gratefully acknowledged for keeping me going when working late at night. And thanks for the anti-stress.

Before I go completely crazy, I would like to thank my family in Italy for the support, always. And my niece Gaia for being the star of my desktop.



# Erklärung

Hiermit versichere ich, dass ich die vorliegende Arbeit ohne unzulässige Hilfe Dritter und ohne Benutzung anderer als der angegebenen Hilfsmittel angefertigt habe. Die als fremde Quellen direkt oder indirekt übernommenen Gedanken sind als solche kenntlich gemacht. Die Arbeit wurde bisher weder im Inland noch im Ausland in gleicher oder ähnlicher Form einer anderen Prüfungsbehörde vorgelegt.

Die vorliegende Arbeit wurde am Helmholtz-Zentrum Dresden - Rossendorf unter der wissenschaftlichen Betreuung von Prof. Dr. Eckart Grosse angefertigt.

Es haben bisher keine Promotionsverfahren stattgefunden.

Ich erkenne die Promotionsordnung der Fakultät Mathematik und Naturwissenschaften vom 20.03.2000 an.

*Dresden, Januar 2011*

Michele Marta